MESOSCALE MODELING OF DYNAMIC FAILURE OF SHOCKED SINGLE CRYSTALS AND POLYCRYSTALS

A Dissertation

by

THAO THI TAM NGUYEN

Submitted to the Office of Graduate and Professional Studies of
Texas A&M University
in partial fulfillment of the requirements for the degree of

DOCTOR OF PHILOSOPHY

Chair of Committee:	Justin W. Wilkerson
Committee Members:	J. N. Reddy
	Alan Freed
	A. Amine Benzerga
Head of Department:	Andreas A. Polycarpou

May 2019

Major Subject: Mechanical Engineering

ABSTRACT

A framework for dislocation-based viscoplasticity and dynamic ductile failure (CPD-FE) has been developed to model high strain rate deformation and damage in single crystals and polycrystals. The rate dependence of the crystal plasticity formulation is based on the physics of relativistic dislocation kinetics suited for extremely high strain rates. The damage evolution is based on the dynamics of void growth, which are governed by both micro-inertia as well as dislocation kinetics and dislocation substructure evolution. An averaging scheme is proposed in order to approximate the evolution of the dislocation substructure in both the macroscale as well as its spatial distribution at the microscale. Additionally, a concept of a single equivalent dislocation density that effectively captures the collective influence of dislocation density on all active slip systems is proposed here. Together, these concepts and approximations enable the use of semi-analytic solutions for void growth dynamics, which greatly reduce the computational overhead that would otherwise be required. The resulting homogenized CPD-FE framework has been implemented into a commercially available finite element package, and a validation assessment against a suite of direct numerical simulations was carried out. The model is calibrated and validated against published experimental data of the stress-strain response of single crystals subject to dynamic loading conditions. Lastly, the model is utilized to study polycrystals at the mesoscale level through the explicit resolution of individual grains, i.e. resolving each individual grain's size, shape, and orientation. A few thousand mesoscale calculations are carried out, systematically varying the misorientation angles of the grain boundaries (GB) in the computational microstructures. Despite the fact that the CPD-FE model neglects the possibility of variation in inherent GB weakness, the CPD-FE simulations agree favorably with experimental observations that have demonstrated a non-monotonic relationship be-

tween GB misorientation and the likelihood of failure initiation along said GB. The role played by mechanics, i.e. elastic and plastic anisotropy, in this non-monotonic trend is elucidated here.

ACKNOWLEDGMENTS

I would like to thank my advisor, Dr. Justin W. Wilkerson, for reaching out to me when I had serious moments of self-doubt in pursuing fundamental science research. His trust and encouragement during each of my struggles helped me overcome those difficult moments. The guidance and challenging opportunities that he offered inspired me in doing a better job as a researcher. I would also like to thank my mentor, Dr. Darby J. Luscher, for his support and many fruitful hours-long discussions during my short summer visit at Los Alamos National Laboratory and my graduate study after that. I also appreciate Dr. Jeffrey T. Lloyd for challenging my modeling results each time we met, providing me his thoughtful ideas and in-depth perspectives. I would like to thank my committee members: Dr. Alan Freed, Dr. J.N. Reddy, Dr. A. Amine Benzerga for their thorough comments on my work, which helps improve the quality of my dissertation.

I would like to thank my undergraduate advisor, Dr. Tran Tran, for his endless encouragement to pursue higher education in mechanical engineering. Dr. Tran Tran inspires me by living the example of modest scientist in the situation of limited resources.

A special thank you goes out to my college friend, Dr. Nam Ngô, for his patience to answer or help find the answers to all kind of questions that I had from LaTex usage to complex research questions. My special appreciation also goes to my group members: Zach Huber, Sara Adibi, Babak Ravaji, Eli Iglesias, Mash Nitol, for lifting my spirit, providing much needed random humor and comfort.

I am deeply indebted to my parents for supporting me, setting examples of lifelong learner, and their prompt responses to prevent my many possible total wrecks. I am also thankful for my sisters, Thuy Nguyen and Hieu Nguyen, for their encouragement and support. Finally, I would like to dedicate this work to my loving husband, Duc Phan,

and two daughters, Thao-Nguyen Phan and Alice Phan. You are always being by my side through all of my ups and downs, constantly reminding me to stay calm and focus, embracing me with love and joy.

CONTRIBUTORS AND FUNDING SOURCES

Contributors

This work was supervised by a dissertation committee consisting of Professors Justin W. Wilkerson (advisor), J. N. Reddy, Alan Freed of the Department of Mechanical Engineering, Professor A. Amine Benzerga of the Department of Aerospace Engineering, and Dr. Darby J. Luscher of Los Alamos National Laboratory.

Funding Sources

The research was supported by Army Research Laboratory under the MEDE Collaborative Research alliance through Cooperative Agreement No. W911NF-12-2-0022. Portions of the research were performed under the auspices of the U.S. Department of Energy under contract DE-AC52-06NA25396 and partly under sub-contract 464745. The support of the Advanced Scientific Computing, Physics and Engineering Models Program (ASC-PEM) is acknowledged. The views and conclusions contained in this document are those of the author and should not be interpreted as representing the official policies, either expressed or implied, of the Army Research Laboratory or the U.S. Government. Portions of this research were conducted with high performance research computing resources provided by Texas A&M University (`https://hprc.tamu.edu`).

NOMENCLATURE

Acronyms

CP	Crystal plasticity
CPD	Crystal plasticity damage
CPD-FE	CPD finite element model
MD	Molecular Dynamics
KB/SHPB	Kolsky bar or split Hopkinson pressure bar
BVP	Boundary value problem
ODE	Ordinary differential equation
DNS	Direct numerical simulation
GB	Grain boundary
TB	Twin boundary
FZ	Fundamental zone
SCF	Stress concentraion factor
RSS	Resolved shear stress
CRSS	Critical resolved shear stress
cr	Critical value
m	Mobile dislocation
im	Immobile dislocation
eff	Effective value
eq	Equivalent value
$mult$	Multiplication
$trap$	Trapping
ann	Annihilation
rec	Recovery
nuc	Nucleation
het	Heterogeneous
hom	Homogeneous

General

ρ_s	Mass density of solid material at rest
b	Burgers vector
(α)	Slip system index
$c_\perp$	Taylor interaction factor
μ	Shear modulus
c_s	Shear wave speed
$\mathbf{I}$	Second order identity tensor
$\mathbf{e}$	Basis vector in reference configuration
$\mathbb{I}$	Forth order identity tensor
$\mathbb{S}$	Eshelby's tensor
$\mathbb{C}$	Elastic modulus tensor in crystal basis
Σ_{sp}	Material spall strength
c_{0b}	Bulk wave speed at ambient condition

Ductile failure

a	Current void radius
φ	Current void volume fraction
a_0	Initial void radius
φ_0	Initial void volume fraction
ℓ_v	Average void spacing in reference configuration
$\mathcal{R}$	Internal resistance to void growth
$\mathcal{R}_{dd}$	Dislocation dynamics resistance
$\mathcal{R}_{cr}$	Quasistatic resistance

M_T	Taylor factor
$\mathbb{C}^d$	Effective elastic modulus tensor in crystal basis

Crystal Plasticity

Microscale	*Macroscale*	*Description*
$\mathbf{f}$	$\mathbf{F}$	Total deformation gradient tensor
$\mathbf{f}^e$	$\mathbf{F}^e$	Elastic part of the deformation gradient tensor
$\mathbf{f}^p$	$\mathbf{F}^p$	Plastic part of the deformation gradient tensor
$-$	$\mathbf{F}^d$	Damage part of the deformation gradient tensor
$\mathbf{s}$	$\mathbf{\Sigma}$	Cauchy stress
$\mathbf{l}$	$\mathbf{L}$	Velocity gradient
$v_\perp$	$\mathcal{V}_\perp$	Dislocation velocity
τ	T	Resolved shear stress
τ_{cr}	T_{cr}	Critical resolved shear stress
$\dot{\gamma}$	$\dot{\Gamma}$	Slip rate
$\mathbf{s}_0$	$\mathbf{s}_0$	Slip direction vector in crystal basis
$\mathbf{n}_0$	$\mathbf{n}_0$	Slip plane normal vector in crystal basis
$\mathbf{s}$	$\mathbf{S}$	Slip direction vector in plastically deformed configuration
$\mathbf{n}$	$\mathbf{N}$	Slip plane normal vector in plastically deformed configuration
ϱ	$\langle\varrho\rangle^s$	Total dislocation density
ϱ_m	$\langle\varrho_m\rangle^s$	Mobile dislocation density
ϱ_{im}	$\langle\varrho_{im}\rangle^s$	Mobile dislocation density

TABLE OF CONTENTS

LIST OF FIGURES

FIGURE Page

LIST OF TABLES

TABLE Page

1. INTRODUCTION AND MOTIVATION

A deeper understanding of and control over the fundamental processes governing deformation and failure of ductile metals subject to dynamic loading is vital to the advancement of a number of applications, e.g. personal and vehicular protection systems, spacecraft shielding, automotive crash safety, and advanced manufacturing. Despite this technological importance, many fundamental aspects of dynamic ductile failure are poorly understood and the sophistication of constitutive models for dynamic ductile failure has lagged behind their quasi-static counterparts. Our aim here is to advance the state-of-the-art in this area through the development, implementation, calibration, verification, and validation of what is to our knowledge the first dislocation-based crystal plasticity framework for dynamic ductile failure. In particular, this dissertation focuses on spall strength and dynamic failure of crystalline and polycrystalline metals. The ultimate goal of this work is to understand the relationship between dynamic mechanical behavior, microstructure, and loading conditions, which will ultimately provide guidance for material selection and material design for shock loading applications.

1.1 Shock compression and spall failure experiments

While the proposed framework is applicable to general loading situations, the shock deformation and failure of materials is typically studied experimentally via plate impact testing. A single plate impact experiment provides a wealth of information that may be utilized to calibrate and validate viscoplasticity and damage constitutive models. In addition, physics-based models, like the one developed here, may be utilized to interpret aspects of

The present chapter is based on publications by Nguyen et al. (2017, 2019).

the experimental measurements and observations, e.g. dislocation nucleation and kinetics, twin and void dynamics, phase transformations, etc.

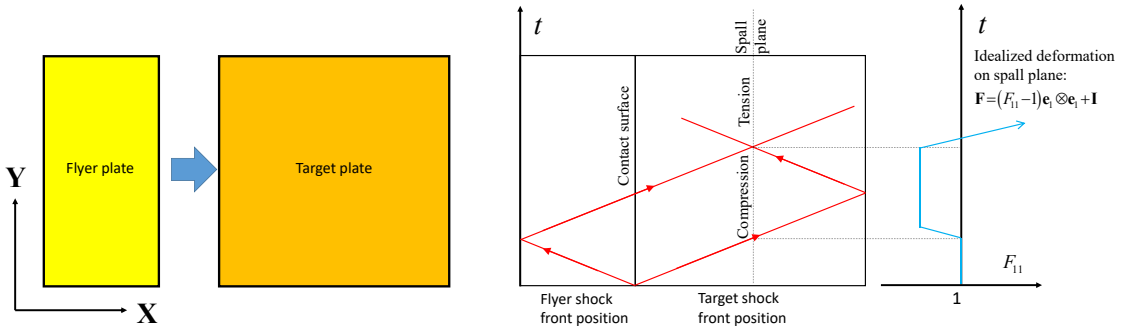

Fig. 1.1: From left to right: schematic of a plate impact test; typical time versus stress wave front position diagram for plate impact tests; idealized deformation description on the spall plane.

The schematic of a plate impact test is shown in Fig. 1.1. In the test, a flyer plate is accelerated to come into contact with a target plate which is initially at rest (Meyers and Aimone, 1983; Meyers, 1994; Kanel, 2010). The target plate is made of the material of interest. The contact generates two compressive incident waves traveling away from the impact surface in both plates (cf. Fig. 1.1). As those waves reach the rear ends, they are reflected back as rarefaction fan waves, meet each other again and generate a tensile wave at a position called the spall plane. By controlling the thickness ratio between the target and the flyer, experimentalists can design the spall plane to be in the middle of the target plate. In particular, for two plates of the same material, a ratio greater than one creates a spall plane inside the target plate; a ratio of two creates a spall plane in the middle of the target plate (cf. Fig. 1.1). Due to the high aspect ratios between the plates' radiuses to their thickness, the strain state of a volume element on the spall plane can idealized as uniaxial

strain, i.e. its macroscopic deformation gradient can be written as

$$[\mathbf{F}] = \begin{bmatrix} F_{11} & 0 & 0 \\ 0 & 1 & 0 \\ 0 & 0 & 1 \end{bmatrix}. \tag{1.1.1}$$

The coefficients for the above deformation gradient tensor and other tensors below are with respect to the basis show in Fig. 1.1. In the absence of rigid rotation, the logarithmic strain tensor $\boldsymbol{\epsilon}$ can then be written as

$$[\boldsymbol{\epsilon}] = \begin{bmatrix} \ln(F_{11}) & 0 & 0 \\ 0 & 0 & 0 \\ 0 & 0 & 0 \end{bmatrix}. \tag{1.1.2}$$

The deviatoric part of the logarithmic strain tensor can be written as

$$[\boldsymbol{\epsilon'}] = \begin{bmatrix} \frac{2}{3}\ln(F_{11}) & 0 & 0 \\ 0 & -\frac{1}{3}\ln(F_{11}) & 0 \\ 0 & 0 & -\frac{1}{3}\ln(F_{11}) \end{bmatrix}. \tag{1.1.3}$$

The equivalent logarithmic strain is then simplified as

$$\epsilon_{eq} \equiv \sqrt{\frac{2}{3}\boldsymbol{\epsilon'} : \boldsymbol{\epsilon'}} = \frac{2}{3}\ln(F_{11}). \tag{1.1.4}$$

In order to diagnose the macroscopic material behavior, the velocity history of the free surface of the target plate is recorded using velocity interferometer system for any reflectors (VISAR, Meyers, 1994). Figure 1.2 presents a generic free surface velocity (u_{fs}) history from a plate impact test. Due to shock loading, the dynamic behavior of a

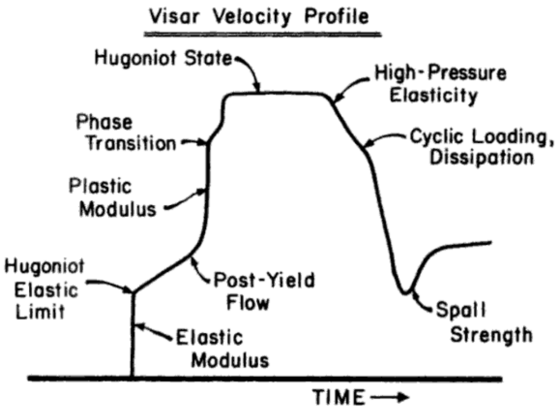

Fig. 1.2: Illustration of a typical free surface velocity history (Meyers, 1994, figure 4.8(b)).

material depends on the strong stress wave propagation, reflection and interaction. The recorded velocity history provides important information on that dynamic behavior, such as Hugoniot elastic limit (or the dynamic yield strength), plastic hardening or softening, phase transition, as can be seen in Fig. 1.2.

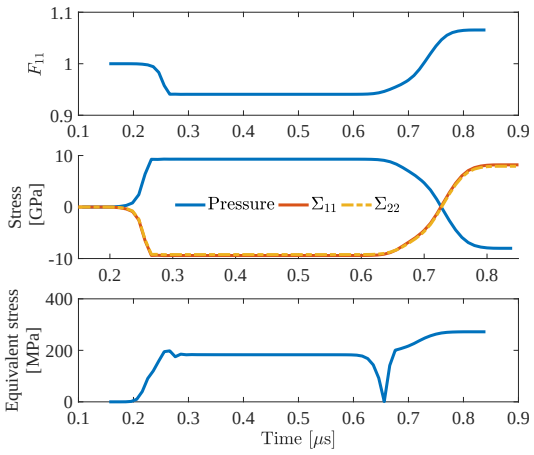

Fig. 1.3: Typical time evolution of F_{11}, pressure and equivalent stress of a volume element on spall plane without damage evolution.

One particularly important property that may be obtained from the velocity history is the spall strength, which is the tensile strength of a material under shock loading conditions. For an isotropic material, the Cauchy stress tensor for the uniaxial strain deformation on spall plane can be written as

$$[\boldsymbol{\Sigma}] = \begin{bmatrix} \Sigma_{11} & 0 & 0 \\ 0 & \Sigma_{22} & 0 \\ 0 & 0 & \Sigma_{22} \end{bmatrix}. \tag{1.1.5}$$

The pressure and equivalent stress are then defined as

$$P = -\tfrac{1}{3}(\Sigma_{11} + 2\Sigma_{22}), \tag{1.1.6}$$

$$\Sigma_{eq} = |\Sigma_{11} - \Sigma_{22}|. \tag{1.1.7}$$

By substituting the pressure and equivalent stress into the Cauchy stress we have

$$[\boldsymbol{\Sigma}] = \begin{bmatrix} -P + \frac{2}{3}\Sigma_{eq}\mathrm{sgn}(\Sigma_{11} - \Sigma_{22}) & 0 & \\ 0 & -P - \frac{1}{3}\Sigma_{eq}\mathrm{sgn}(\Sigma_{11} - \Sigma_{22}) & 0 \\ 0 & 0 & -P - \frac{1}{3}\Sigma_{eq}\mathrm{sgn}(\Sigma_{11} - \Sigma_{22}) \end{bmatrix}. \tag{1.1.8}$$

The deviatoric part of the Cauchy stress can be written as

$$[\boldsymbol{\Sigma}'] = \begin{bmatrix} \frac{2}{3}\Sigma_{eq}\mathrm{sgn}(\Sigma_{11} - \Sigma_{22}) & 0 & \\ 0 & -\frac{1}{3}\Sigma_{eq}\mathrm{sgn}(\Sigma_{11} - \Sigma_{22}) & 0 \\ 0 & 0 & -\frac{1}{3}\Sigma_{eq}\mathrm{sgn}(\Sigma_{11} - \Sigma_{22}) \end{bmatrix}. \tag{1.1.9}$$

Figure 1.4 illustrates the time evolution of deformation gradient F_{11} and stress on the spall plane, when damage evolution is not activated. When shock wave reaches the spall

plane for the first time (≈ 0.2 μs), the volume element on the spall plane is subjected to compression (i.e. $F_{11} < 1$), leading to a positive compression pressure and an increase in equivalent stress. When the two reflected waves from the flyer and target free surface interact at the spall plane (≈ 0.65 μs), the volume element is unloaded and then stretched (i.e. $F_{11} > 1$), leading to a tensile hydrostatic stress and an increase in equivalent stress after unloading. During loading, the principle stresses Σ_{11} and Σ_{22} of ductile materials are close to the opposite of pressure. The two stresses Σ_{11} and Σ_{22} cross each other when unloading initiates (≈ 0.65 μs).

Figure 1.4 illustrates the stress states on the spall plane with 3 deformation modes: elastic; elasto-plastic; elasto-plastic with damage evolution, and their corresponding free surface velocity. With elasto-plastic behavior, the the equivalent stress increases to the yield strength and then relaxes, as compared to purely elastic behavior, with hardening or softening as loading progresses. Without damage evolution, the pressure continues to drop to a negative value close to the peak compression pressure ($\approx$ 10 GPa in Fig. 1.4) as tension progresses. In reality, when the tensile stress is higher than the dynamic tensile strength of the material, nanovoids and/or microvoids can nucleate, grow and coalesce. That damage evolution relaxes the hydrostatic stress. The stress relaxation on spall plane sends a pullback signal to the recorded velocity history, as illustrated in Fig. 1.4(c).

From the difference between the maximum (u_{fs}^{max}) and local minimum (u_{fs}^{min}) of the target plate free surface velocity (cf. Fig. 1.5), which is usually called the pullback velocity, an acoustic estimation (Kanel, 2010) of the target plate material spall strength can be obtained as

$$\Sigma_{sp} = \frac{1}{2}\rho_s c_{0b}\left(u_{fs}^{max} - u_{fs}^{min}\right). \tag{1.1.10}$$

In the above equation, ρ_s is the mass density of the solid material at rest, c_{0b} is the bulk wave speed at ambient condition. Romanchenko and Stepanov (1980) proposed a correc-

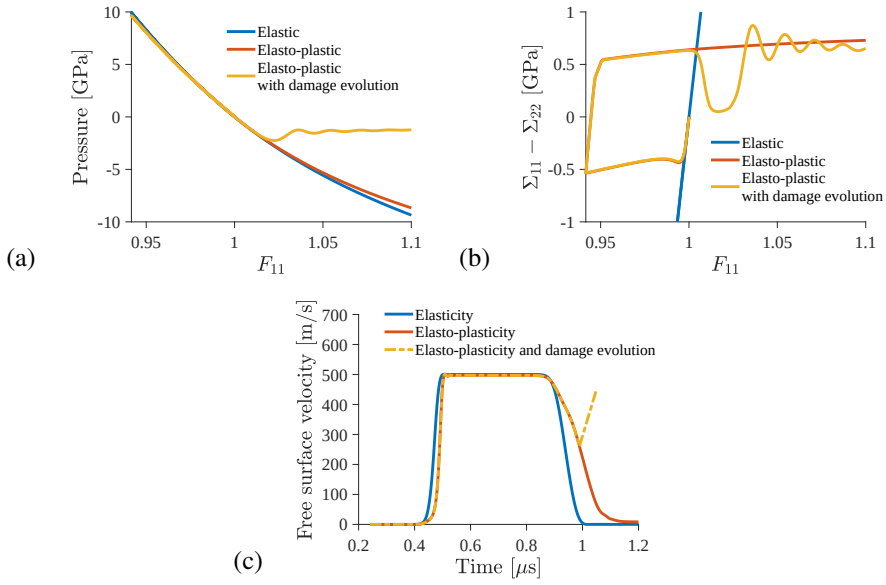

Fig. 1.4: Evolution of (a) pressure and (b) $(\Sigma_{11} - \Sigma_{22})$ of a volume element on spall plane for pure elastic; elasto-plastic; elasto-plastic with damage evolution material behavior. Equivalent stress is the absolute value of $(\Sigma_{11} - \Sigma_{22})$. (c) Corresponding velocity histories.

tion to the bulk wave speed using the longitudinal wave speed as below

$$\Sigma_{sp} = \rho_s \left(u_{fs}^{max} - u_{fs}^{min} \right) \frac{c_{0b} c_{0l}}{c_{0b} + c_{0l}}, \tag{1.1.11}$$

with c_{0l} denoting the longitudinal wave speed at rest. Kanel (2010) proposed a correction to the pullback velocity using the time-derivative of the free surface velocity right before and after spall signal as below

$$\Sigma_{sp} = \frac{1}{2} \rho_s c_{0b} \left(u_{fs}^{max} - u_{fs}^{min} + h_{sp} \left(\frac{1}{c_{0b}} - \frac{1}{c_{0l}} \right) \frac{du_{fs}}{dt}^{*} \right) \tag{1.1.12}$$

In the above equation, h_{sp} is the target thickness, $\frac{du_{fs}}{dt}^{*} = \frac{|\dot{u}_1| \dot{u}_2}{|\dot{u}_1| + \dot{u}_2}$ is a function of deceleration before spall ($\dot{u}_1$) and acceleration after spall ($\dot{u}_2$). Due to its simplicity, Eq. (1.1.10) is the most commonly used formulation to estimate spall strength from plate impact test.

At a given compressive pressure (i.e. for given flyer-target impedance and impact velocity), different strain rates can be obtained by varying the plates thickness. This is the result of the shock wave attenuation due to propagation inside the target material. In particular, an increase in the target plate thickness results in reducing the loading rate. The tensile loading rate is usually estimated from the unloading curve in the free surface velocity history (right before spall signal - see Fig. 1.5) as below

$$\dot{\varepsilon} = \frac{1}{2c_{0b}} \left. \frac{du_{fs}}{dt} \right|_{t=t_{sp}} . \tag{1.1.13}$$

Equation (1.1.13) is a rough approximation of tensile strain rate and it is likely smaller than the real rate during spallation, due to shock wave attenuation with propagation and the spreading of rarefaction wave to target free surface. For example, the tensile strain rate on spall plane from plate impact tests (i.e. using Eq. (1.1.13)) is ≈ 6 times lower than their hydrodynamic computer simulation counterparts (i.e. directly approximate from spall plane deformation) in (Turley et al., 2018).

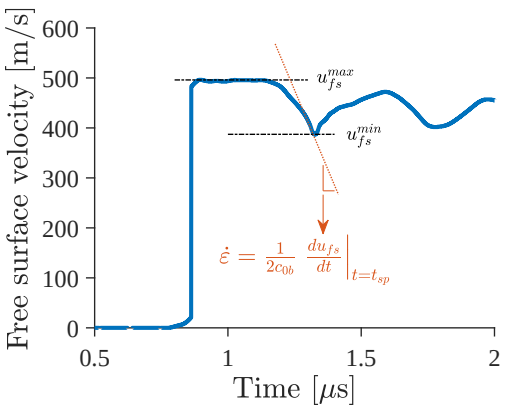

Fig. 1.5: Typical recorded velocity history of target free surface, reproduced from shot 1 data of Turley et al. (2018).

Beside the indirectly measured spall strength from target free surface velocity, the target damage morphology can also be useful in correlating the spall strength to microstructure of the materials (Peralta et al., 2009; Wayne et al., 2010; Brown, 2015; Krishnan et al., 2015; Fortin et al., 2016). For example, by analyzing the morphology of the fracture surface (Fig. 1.6), the statistics of damage localization on the spall plane (i.e. the relative tendency to have damage localization of individual microstructure) (Wayne et al., 2010; Brown, 2015) and the damage characteristic (i.e. intergranular versus intragranular) (Peralta et al., 2009) during spallation can be obtained.

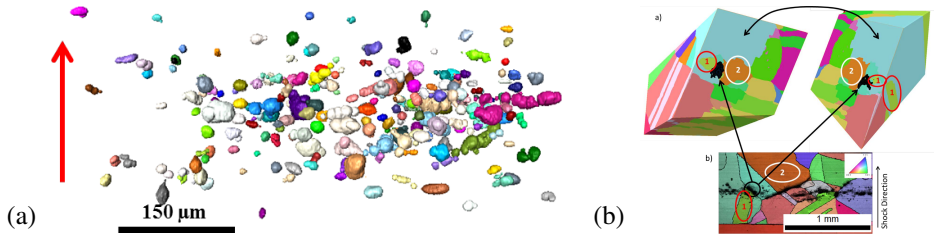

Fig. 1.6: (a) Intergranular and intragranular voids on spall plane of polycrystalline copper. (b) intergranular void in polycrystalline copper (Brown, 2015).

1.2 Key factors governing spall strength of single crystals

Within high purity metal single crystals, the key factors reported to affect spall strength are the crystal orientation (Minich et al., 2004; Turley et al., 2018), and the loading conditions including the shock pressure (Minich et al., 2004; Turley et al., 2018), tensile strain rate (Srinivasan et al., 2007; Turley et al., 2018), and the pulse shape of the incident shock wave (Gray III et al., 2007; Luo et al., 2009b). However, the reported trends relating the apparent spall strength in single crystals and these key factors seem to contradict each other in some cases. For example, orientation dependence was observed in the experiments of Minich et al. (2004); Perez-Bergquist et al. (2011); Turley et al. (2018), but not

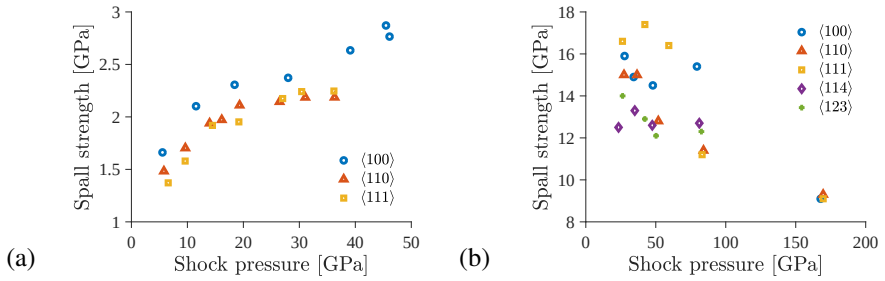

Fig. 1.7: Variation of single crystal copper spall strength with respect to shock pressure from (a) plate impact tests, (b) MD calculation (reproduced from (Minich et al., 2004) and (Luo et al., 2009a), respectively).

in MD simulations of Luo et al. (2009a) at a very high pressure (160 GPa) (cf. Fig. 1.7). Also, some of the observations of orientation dependence made solely from experiments are inconsistent with each other, for example in single crystal copper the $\langle 100 \rangle$ orientation was observed to be stronger than the $\langle 110 \rangle$ orientation by Minich et al. (2004) and Turley et al. (2018), but weaker than the $\langle 110 \rangle$ orientation by (Perez-Bergquist et al., 2011), at similar magnitudes of peak shock pressure. Similarly, the spall strength was reported to increase with shock pressure in Minich et al. (2004); Turley et al. (2018), but is observed to decrease with shock pressure, presumably because of the increase in shock temperature, in the results of Luo et al. (2009a) (cf. Fig. 1.7).

While MD simulations provide more detailed insights to the processes occurring within the crystal lattice during the spallation process, they are presently restricted to strain rates that are much higher than those typically associated with experiments. Continuum models offer the opportunity to bridge across the disparate time scales, but require that the appropriate mechanisms are incorporated into the constitutive theory for single crystal behavior.

1.3 The role of microstructure in spall failure

For polycrystalline materials, it is necessary to understand the relationship between spall strength and material microstructure (Meyers and Aimone, 1983; Curran et al., 1987; Meyers, 1994) in order to optimize the strength. Spall strength tends to be highly sensitive to microstructure, and sometimes exhibits perplexing relationships. For example, alloying can either increase (Chen et al., 2006; Wang et al., 2014) or decrease (Curran et al., 1987; Pedrazas et al., 2012) the spall strength of aluminum alloys. Likewise, the spall strength dependence on grain size was reported to follow typical Hall-Petch strength-size relation (i.e. *smaller is stronger*) in atomistic calculations (Kuksin et al., 2008; Mackenchery et al., 2016) and some experimental observations (Zurek et al., 1988; Buchar et al., 1991). By contrast, spall strength was observed to increase with increasing grain size (i.e. *smaller is weaker*) in (Minich et al., 2004; Razorenov et al., 2007), with strongest spall strength exhibited in high purity single crystals. This contradiction was argued to be an implication of the competing length scales of grain size and spacing between damage nucleation sites (Wilkerson and Ramesh, 2016). In addition to affecting the spall strength, grain size reportedly influenced dynamic fracture morphology of polycrystals (Escobedo et al., 2011, 2014), i.e. influenced the transgranular versus intergranular characteristic of polycrystalline damage.

Beyond grain size, crystal orientation also affects void growth (Ling et al., 2016, 2017, 2018), spall strength (Minich et al., 2004; Turley et al., 2018) and spall failure morphology (Perez-Bergquist et al., 2011). Moreover, from analyzing intergranular spall damage in polycrystal copper, Wayne et al. (2010) and Brown et al. (2015) suggested that microstructure features such as GB misorientation angle may play a role in damage localization. Figure 1.6 shows examples of intragranular and intergranular damages in polycrystalline copper due to spallation. In their observation, the likelihood of finding intergranular

damage was related to the corresponding misorientation angle (see Fig. 1.8). Their results showed that the peak probability of damage nucleating on a particular GB occurred within the range of 25° to 50° misorientation angle, and the peak was more pronounced in pre-strained polycrystals (Brown et al., 2015).

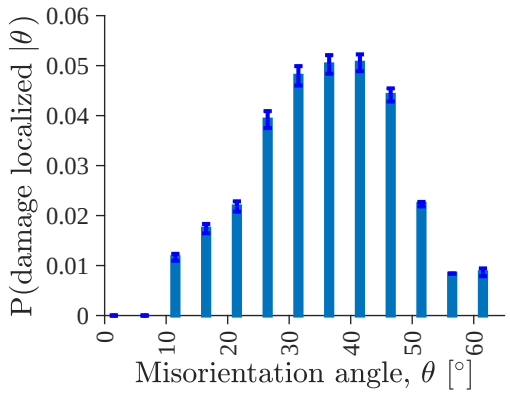

Fig. 1.8: Conditional probability to find voids at GB of given misorientation angle, on spall plane of prestrained polycrystalline copper, reconstructed here from the work of Brown (2015).

The fundamental reason for this correlation is unclear, but is likely related to one of the following factors: inherent GB weakness (e.g. dislocation mobility or lack thereof across a GB, local atomic disregistry) or mechanics of interface incompatibilities (i.e. difference in mechanical behavior of neighboring grains). Fensin and Hahn (2017) used molecular dynamics to study susceptibility of tantalum GBs to dynamic failure, and reported no distinguishable link between the void nucleation stress and GB disorder measures such as energy or excess free volume. In a detailed experimental analysis, Escobedo et al. (2011) found no clear correlation between the likelihood of a GB being damaged and the Schmid factor nor the elastic stiffness mismatch across the GB.

In contrast, Krishnan et al. (2015) utilized an extended Gurson model for crystal plasticity to study incipient spall failure for a set of experimentally observed damaged GBs and suggested a larger role of incompatibility in mechanical properties across the interface, as well as interface orientation, on intergranular failure. Wu and Zikry (2016) observed a similar preference of intergranular fracture due to elastoplastic incompatibility when analyzing the mode I fracture of $\Sigma 3$ and $\Sigma 17$b bicrystals. Lieberman et al. (2016) expanded these earlier studies to provide a more fundamental understanding of the relationship between plastic incompatibility and the likelihood of intergranular damage using material characterization in conjunction with direct numerical simulation. However, there has yet to be a systematic and conclusive analysis to fully understand the dominant factors governing the correlation of intergranular damage localization and GB misorientation angles reported in (Wayne et al., 2010; Brown et al., 2015).

1.4 The modeling state of the art

The earliest models of ductile failure were based on the analytic analysis of an isolated void in an otherwise homogeneous infinite medium, e.g. (Bishop et al., 1945; Hill, 1950; McClintock, 1968; Rice and Tracey, 1969; Ball, 1982; Huang et al., 1991). While these early models provided valuable insights into the initial stages of void growth, such models failed to capture the important effect of an evolving void volume fraction, i.e. porosity, thereby limiting their utility in ductile fracture analysis. This shortcoming was remedied by Gurson (1977), who proposed a pioneering micromechanics-based framework capable of modeling the progressive failure of porous materials. In the subsequent decade, Gurson's model was modified into what would become known as the Gurson-Tvergaard-Needleman (GTN) model (Chu and Needleman, 1980; Tvergaard, 1981; Tvergaard and Needleman, 1984), which provided a mixed phenomenological and micromechanics-based framework to distinctly account for the three critical elements of ductile failure, i.e. void

nucleation, growth, and coalescence. For more comprehensive reviews of these ductile failure mechanisms and associated models see (Garrison and Moody, 1987; Pineau and Pardoen, 2007; Besson, 2009; Benzerga and Leblond, 2010; Pineau et al., 2016). One significant drawback of the original model derived by Gurson (1977) was that the derivation is restricted to porous materials whose solid matrix material may be adequately approximated as an elastically rigid and rate-independent perfectly plastic material. Given that most real materials do not behave in this mathematically idealized manner, a significant amount of effort has gone into extending the applicability of this class of ductile failure theories to account for more complex constitutive behaviors of the solid matrix material, including

- viscoplasticity, e.g. Budiansky et al. (1982); Johnson and Cook (1983); Haghi and Anand (1991); Cortés (1992a,b); Tong and Ravichandran (1993, 1995); Paquet and Ghosh (2011); Wilkerson and Ramesh (2014);

- plastic anisotropy, e.g. Benzerga and Besson (2001); Monchiet et al. (2008); Keralavarma and Benzerga (2008, 2010); Keralavarma et al. (2011);

- strain-gradient plasticity (and other nonlocal effects), e.g. Tvergaard and Needleman (1995); Huang et al. (2000); Wu et al. (2003a); Reusch et al. (2003); Wen et al. (2005a,b); Enakoutsa and Leblond (2009); Nguyen et al. (2015);

- crystal plasticity, e.g. Nemat-Nasser and Hori (1987); Han et al. (2013); Paux et al. (2015); Mbiakop et al. (2015);

- inertial effects, e.g. Carroll and Holt (1972); Ortiz and Molinari (1992); Molinari and Mercier (2001); Jacques et al. (2012a,b); Molinari et al. (2015); Jacques et al. (2015).

This dissertation continues this progress towards greater sophistication through the extension to a single crystal matrix material of finite mass density (i.e. non-negligible inertial effects) whose constitutive response is governed by a single crystal dislocation-based viscoplasticity model (Lloyd et al., 2014b) applicable for extremely high strain rates.

As stated earlier, the development of dynamic ductile failure theories has significantly lagged behind their quasi-static counterparts. For example, the first attempts to extend a Gurson-type porous flow potential to the dynamic regime (i.e. non-negligible microscale inertial effects) were carried out two decades later by Wang and Jiang (1997); Wang (1997) and subsequently in an alternative form by Molinari and Mercier (2001). Even more stark is the fact that this class of Molinari and Mercier (2001) type ductile failure models has been utilized to computationally analyze only about a dozen or so published non-trivial macroscopic boundary value problems, e.g. (Czarnota et al., 2006, 2008; Jacques et al., 2012a,b, 2015; Fick et al., 2015), compared to the hundreds or perhaps thousands that have been solved with the quasi-static GTN model. This disparity is in spite of the well-documented (Carroll and Holt, 1972; Ortiz and Molinari, 1992; Tong and Ravichandran, 1993, 1995; Wu et al., 2003b; Molinari and Wright, 2005) important role played by micro-inertia in retarding the growth of voids under dynamic loading. The real-world importance of micro-inertia has been further bolstered by several recent works (Czarnota et al., 2006; Wright and Ramesh, 2008; Czarnota et al., 2008; Jacques et al., 2010; Wilkerson and Ramesh, 2014, 2016), which have invoked micro-inertia as the dominant mechanism governing the experimentally-observed strong strain rate-dependence of spall strength (a measure of dynamic tensile strength inferred from high velocity plate impact experiments) reported in e.g. (Moshe et al., 1998, 2000; Antoun, 2003; Cuq-Lelandais et al., 2009; Kanel, 2010). These claims are in contrast to the earlier works that attributed the rate-dependence of spall strength simply to viscoplasticity of the solid matrix material (Seaman et al., 1976; Johnson and Cook, 1983; Perzyna, 1986; Cortés, 1992a,b; Wang, 1994; Zheng

et al., 1994). These discrepancies were rectified by Wu et al. (2003b,a,c) whose calculations clearly demonstrated that viscoplasticity may be dominant in the early stages of void growth; however, the dominant mechanism soon becomes micro-inertia as the voids grow to large sizes ($\gtrsim$ 1-10 μm).

Recently, Wilkerson and Ramesh (2014) argued that a comprehensive revisit of the role played by micro-inertia versus solid matrix material viscoplasticity was long overdue given the extremely high strain rates ($\gtrsim 10^7$ s^{-1}) that may be achieved near the internal surface of a dynamically growing void. At such strain rates, the simple power-law type rate-sensitivity invoked in much of the earlier literature is inadequate (Barton et al., 2011); therefore, Wilkerson and Ramesh (2014) instead utilized the J_2 dislocation-based viscoplasticity model recently proposed by Austin and McDowell (2011) in order to describe the constitutive behavior of the solid matrix material in a thick-wall spherical shell analysis. The key components of the Austin and McDowell (2011) model are (i) an additive decomposition of the total dislocation density into mobile and immobile populations with mobile segments being the carriers of plasticity through an Orowan-type relation; (ii) a mobility law that accounts for the thermally-activated regime as well as the relativistic dislocation regime where dislocation velocities are forbidden to exceed the material wave speed (Eshelby, 1949); and (iii) evolution equations for the dislocation substructure that approximate nucleation, multiplication, trapping, annihilation, and recovery mechanisms. With this model, Wilkerson and Ramesh (2014) demonstrated that while micro-inertia remained dominate for late stage void growth, the retarding effect of viscoplasticity on early growth could be far more severe than previously assumed. In particular, once dislocation velocities near the void surface approach the wave speed the void growth rate is paralyzed and incapable of growing at faster rates regardless of the applied stress. Moreover, the evolution of dislocation substructure may induce a number of unique void growth behaviors, e.g. the complete shut down of void growth (after voids have grown by a factor of

about 10 or 100) due to the starvation of the mobile dislocation density.

Here we account for these important retarding effects of micro-inertia and dislocation kinetics on dynamic void growth in a single crystal ductile failure framework. Unlike (Wilkerson and Ramesh, 2014), which was limited to pure hydrostatic stress states, here we aim to develop a framework applicable to general loading conditions, similar in spirit to the isotropic dynamic ductile failure model of Molinari and Mercier (2001), which is the current state-of-the-art in dynamic ductile failure modeling. The key advancements of the proposed framework over that of Molinari and Mercier (2001) is (i) crystal plasticity rather than J_2 plasticity; (ii) dislocation-based plasticity rather than phenomenological plasticity models; and (iii) relativistic drag-based viscoplasticity more suited to extremely high strain rates. To the best of our knowledge, there is no general framework for dynamic ductile failure that includes even one of these features, let alone all three. Fortunately, the necessary preliminaries are in place with extensions of the dislocation-based J_2 theory of Austin and McDowell (2011) to dislocation-based crystal plasticity having been recently developed by Lloyd et al. (2014b) and Luscher et al. (2017). Figure 1.9 summarizes the key contributions in physics-based viscoplasticity and micromechanics-based damage modeling of isotropic and anisotropic materials.

1.5 Dissertation organization

The remainder of this dissertation is organized as follows.

- chapter 2 is devoted to the theoretical framework for dynamic failure of single crystals. section 2.1 details the finite deformation kinematics invoked for the macroscopic (effectively homogenized) continuum as well as the assumed (approximate) kinematics of microscopic continuum, i.e. the solid matrix material. Furthermore, in order to render a framework that is as computationally tractable as possible, some geometric simplifications are assumed. In section 2.2, we briefly review the mi-

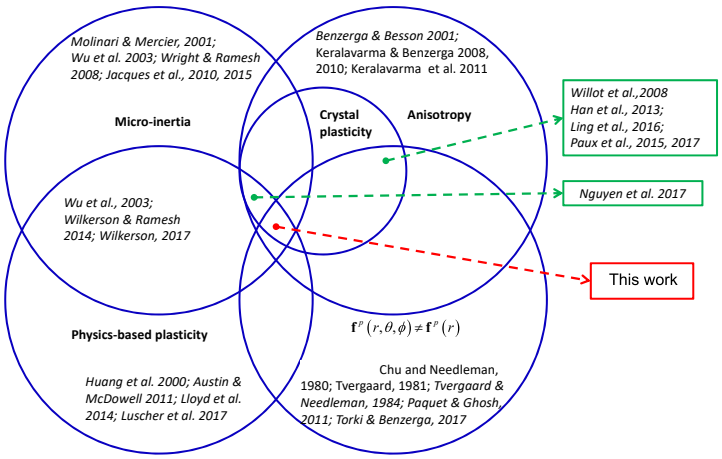

Fig. 1.9: Schematic of key literature in physics-based viscoplasticity and micromechanics-based damage modeling of isotropic and anisotropic materials.

croscopic constitutive equations utilized here to describe the solid matrix material, namely those of (Lloyd et al., 2014b) with some modifications to account for the small length-scales associated with the plastic zone of a growing void. Moreover, the assumed macroscopic constitutive equations are postulated based on volume averaging schemes, and incorporation of porosity effect on macroscopic shear stress threshold. A Mie-Grüneisen equation of state is added to model the nonlinear relationship between pressure and volume. Again, for computational expediency a number of assumptions are made in section 2.3 in order to simplify the evolution equation for porosity evolution down to a single second-order ordinary differential equation.

- chapter 3 details a fairly extensive validation assessment of the predictive capability of the homogenized single crystal dynamic ductile failure framework in comparison

with direct numerical simulations. While this validation effort provides no assessment of the validity of chosen model parameters, it does provide some degree of confidence in the assumptions made throughout section 2.2.

- chapter 4 presents calibration of model parameters against experimental results. The chapter is divided into crystal plasticity calibration in subsection 4.1.1 and damage distribution calibration in subsection 4.1.2. section 4.2 analyzes the pressure dependence of spall strength on a range [4,14] GPa pressure.

- chapter 5 aims to shed light on the potential role of mismatch in anisotropic properties across a grain boundary (GB) in explaining the observed intergranular damage statistics in polycrystalline copper due to spallation. section 5.1 details the boundary value problem (BVP) that is used in the chapter to study misorientation dependence of damage localization preference. section 5.2 presents the simulation results and discussion of the possible governing factors.

- Lastly, chapter 6 presents concluding remarks and future directions.

- The details of the implementation scheme and verification of the CPD-FE VUMAT are provided in an appendix.

2. FRAMEWORK

2.1 Kinematics

2.1.1 Kinematics at macroscale

Consider a general porous single crystal in a reference (undeformed) configuration $\mathcal{B}_0$. The body may be mapped into the current configuration $\mathcal{B}_t$ through the total macroscopic deformation gradient tensor $\mathbf{F}$, as shown in Fig. 2.1. A multiplicative decomposition of the total macroscopic deformation gradient tensor is assumed, i.e. $\mathbf{F} = \mathbf{F}^e\mathbf{F}^p\mathbf{F}^d$, where $\mathbf{F}^d$ accounts for irreversible volumetric deformation, $\mathbf{F}^p$ accounts for irreversible deviatoric deformation, and $\mathbf{F}^e$ accounts for reversible elastic deformation of the body. The solid material is taken to be plastically incompressible, and hence the porosity may be directly related to the damage part of the macroscopic deformation gradient tensor as

$$\mathbf{F}^d = \sqrt[3]{\frac{1-\varphi_0}{1-\varphi}}\mathbf{I} \tag{2.1.1}$$

with $\mathbf{I}$ denoting the second order identity tensor, φ and φ_0 denoting void volume fraction and its initial value, respectively.

The elastic strain measure utilized throughout this proposal is the Green-Lagrange strain, i.e. $\mathbf{E}^e \triangleq \frac{1}{2}(\mathbf{F}^{eT}\mathbf{F}^e - \mathbf{I})$. The total macroscopic velocity gradient $\mathbf{L} \triangleq \dot{\mathbf{F}}\mathbf{F}^{-1}$ is additively decomposed into elastic, irreversible deviatoric, and irreversible volumetric parts:

$$\mathbf{L} = \underbrace{\dot{\mathbf{F}}^e\mathbf{F}^{e-1}}_{\triangleq\mathbf{L}^e} + \underbrace{\mathbf{F}^e\dot{\mathbf{F}}^p\mathbf{F}^{p-1}\mathbf{F}^{e-1}}_{\triangleq\mathbf{L}^p} + \underbrace{\mathbf{F}^e\mathbf{F}^p\dot{\mathbf{F}}^d\mathbf{F}^d\mathbf{F}^{p-1}\mathbf{F}^{e-1}}_{\triangleq\mathbf{L}^d}, \tag{2.1.2}$$

The present chapter is based on publication by Nguyen et al. (2017).

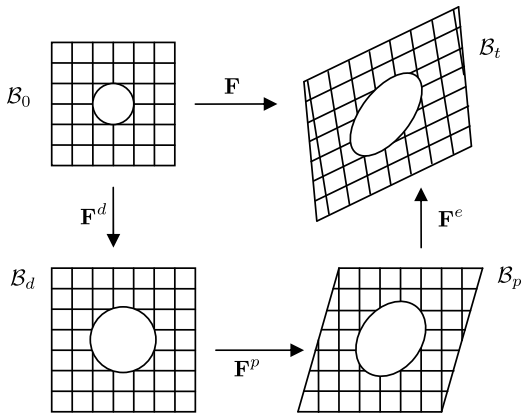

Fig. 2.1: Schematic of a multiplicative decomposition of total macroscopic deformation gradient tensor $\mathbf{F}$ into elastic $\mathbf{F}^e$, irreversible deviatoric $\mathbf{F}^p$, and irreversible volumetric $\mathbf{F}^d$ parts.

The irreversible deviatoric velocity gradient in the intermediate configuration, which will be utilized in the crystal plasticity macroscopic constitutive relationship, is obtained by pull back of $\mathbf{L}^p$ via $\mathbf{F}^e$, i.e. $\tilde{\mathbf{L}}^p = \dot{\mathbf{F}}^p\mathbf{F}^{p-1}$, $\tilde{\cdot}$ denoting the tensor at intermediate configuration $\mathcal{B}_p$. The plastic part of the rate of deformation tensor in the intermediate configuration is denoted as $\tilde{\mathbf{D}}^p \triangleq \frac{1}{2}(\mathbf{F}^{eT}\mathbf{F}^e\tilde{\mathbf{L}}^p + \tilde{\mathbf{L}}^{pT}\mathbf{F}^{eT}\mathbf{F}^e)$, cf. (Luscher et al., 2013).

2.1.2 Geometric considerations

Consider again the porous single crystal described in Fig. 2.1. For simplicity, the porous single crystal is assumed to have uniform void size and void distribution, and preserve the number of voids during deformation. As a consequence, the porosity φ can be computed as

$$\varphi = \frac{4}{3}\pi N_v a^3 \tag{2.1.3}$$

with a denoting void radius, N_v denoting the total number of voids per unit volume of total material in the intermediate damaged configuration $\mathcal{B}_d$. This number density of voids may be directly related to an characteristic length scale $\ell_v \triangleq \left(\frac{4}{3}\pi N_v\right)^{-\frac{1}{3}}$, and thus we express

Eq. (2.1.3) as:

$$\varphi = \left(\frac{a}{\ell_v}\right)^3. \tag{2.1.4}$$

2.1.3 Kinematics at microscale

Consider now the microscale deformation of the representative spherical shell in the intermediate damaged configuration $\mathcal{B}_d$. Since all of the irreversible volumetric deformation is attributed to void growth, the microscale deformation will consist of only elastic and irreversible deviatoric deformation. As with the macroscale, a multiplicative split of the total microscopic deformation gradient $\mathbf{f}$ is assumed, i.e. $\mathbf{f} = \mathbf{f}^e\mathbf{f}^p$, with $\mathbf{f}^e$ and $\mathbf{f}^p$ denoting the microscopic elastic and plastic parts of the deformation gradient tensor, respectively. Here, lowercase variables generally denote microscale field quantities. The deformation gradient at microscale ($\mathbf{f}$) is indirectly related to the deformation gradient at macroscale ($\mathbf{F}$) through volume averaged strain, i.e. $\mathbf{E} = \mathcal{V}^{-1}\iiint_{\mathcal{V}} \mathbf{e} d\mathcal{V}$, where $\mathbf{E}$ and $\mathbf{e}$ are Green-Lagrange strain tensor at microscale and macroscale.

Turning our attention to closed-form approximation of these deformation fields, following Gurson (1977) consider a velocity field (absent of rigid body motion) in the intermediate configuration additively composed of a spatially-varying (non-negligible fluctuations), spherically-symmetric motion and a linear field approximated as an affine (nil fluctuations) extrapolation of the macroscale isochoric motion in the intermediate plastic configuration $\mathcal{B}_p$, i.e.

$$\mathbf{v}_p(\mathbf{x}_p, t) = \dot{r}_p(r_p, t)\mathbf{e}_\mathbf{r} + \tilde{\mathbf{L}}^p \cdot \mathbf{x}_\mathbf{p}, \tag{2.1.5}$$

where $\mathbf{v}_p$ denotes the spatial velocity at time t of a microscopic material point located at $\mathbf{x_p}$ in the intermediate configuration. Likewise, r_0 and r_p respectively denote the radial position of microscale material point in the reference and intermediate plastic configurations in the absence of macroscopic irreversible deviatoric deformation in the intermediate plas-

tic configuration, i.e. $\mathbf{F}^p = \mathbf{I}$. The incompressibility of the matrix material, i.e. $\det \mathbf{f}^p = 1$, places a constraint on admissible solutions for r_p, such that the plastic part of the velocity gradient tensor may be obtained as

$$\tilde{\mathbf{l}}^p \triangleq \frac{\partial \mathbf{v}_p}{\partial \mathbf{x}_p} = \tilde{\mathbf{L}}^p - 2\frac{\dot{r}_p}{r_p}\mathbf{e}_r \otimes \mathbf{e}_r + \frac{\dot{r}_p}{r_p}\left(\mathbf{e}_\theta \otimes \mathbf{e}_\theta + \mathbf{e}_\phi \otimes \mathbf{e}_\phi\right), \tag{2.1.6}$$

where the second two terms on the right-hand side of Eq. (2.1.6) approximate the spatial fluctuations from the mean experienced in the solid matrix material.

Moreover, the plastic part of rate of deformation tensor at intermediate configuration is simply the symmetric part of Eq. (2.1.6), i.e.

$$\tilde{\mathbf{d}}^p = \bar{\mathbf{D}}^p \underbrace{-2\frac{\dot{r}_p}{r_p}\mathbf{e}_r \otimes \mathbf{e}_r + \frac{\dot{r}_p}{r_p}\left(\mathbf{e}_\theta \otimes \mathbf{e}_\theta + \mathbf{e}_\phi \otimes \mathbf{e}_\phi\right)}_{\triangleq \tilde{\mathbf{d}}^p_\mu}, \tag{2.1.7}$$

with $\bar{\mathbf{D}}^p \triangleq \frac{1}{2}(\tilde{\mathbf{L}}^p + \tilde{\mathbf{L}}^{pT})$ and $\tilde{\mathbf{d}}^p_\mu$ denoting the microscale fluctuations from the macroscale plastic part of the rate of deformation tensor in the intermediate plastic configuration. An invariant-based equivalent scalar plastic strain rate is defined here as $\dot{\varepsilon}^p_{eq} \triangleq \sqrt{\frac{2}{3}\tilde{\mathbf{d}}^p : \tilde{\mathbf{d}}^p}$. A measure of the fraction of the equivalent plastic strain rate associated with the fluctuations alone is denoted here as $\dot{\varepsilon}^p_{eq}\big|_\mu$, and may be computed from Eq. (2.1.7) with $\bar{\mathbf{D}}^p = \mathbf{0}$, i.e. $\dot{\varepsilon}^p_{eq}\big|_\mu = 2|\dot{r}_p| r_p^{-1}$, which may be alternatively expressed as $\dot{\varepsilon}^p_{eq}\big|_\mu = 2|\dot{a}_p|\, a_p^2 r_p^{-3}$. Finally, defining the porosity in the intermediate plastic configuration as $\varphi \triangleq (a_p/\ell^p_v)^3$ this equivalent plastic strain rate associated with microscale fluctuations is related to the porosity growth rate in the intermediate plastic configuration, i.e.

$$\dot{\varepsilon}^p_{eq}\big|_\mu = \frac{2}{3}\frac{a_p^3}{r_p^3}\frac{|\dot{\varphi}|}{\varphi - \varphi^2}. \tag{2.1.8}$$

While Eq. (2.1.7) may suffice for isotropic porous plasticity, e.g. Gurson (1977), here

we are interested in a crystal plasticity framework in which the plastic part of the velocity gradient tensor is a cumulative byproduct of the plastic slip rates $\dot{\gamma}_p^{(\alpha)}$ on each of the various slip systems (denoted by subscript α), i.e.

$$\tilde{\mathbf{l}}^p = \sum_{\alpha=1}^{n_{slip}} \dot{\gamma}_p^{(\alpha)} \mathbf{s}_0^{(\alpha)} \otimes \mathbf{n}_0^{(\alpha)}, \tag{2.1.9}$$

with $\mathbf{s}_0^{(\alpha)}$ and $\mathbf{n}_0^{(\alpha)}$ respectively denoting the unit slip direction and unit slip plane normal in the reference configuration and n_{slip} denoting the total number of slip systems. Likewise for the macroscale,

$$\tilde{\mathbf{L}}^p = \sum_{\alpha=1}^{n_{slip}} \dot{\Gamma}_p^{(\alpha)} \mathbf{s}_0^{(\alpha)} \otimes \mathbf{n}_0^{(\alpha)}, \tag{2.1.10}$$

with $\dot{\Gamma}_p^{(\alpha)}$ denoting the effective macroscale plastic slip rate. In most crystal plasticity frameworks, $\dot{\gamma}_p^{(\alpha)}$ is utilized to evolve internal state variables. As such, it will prove useful to formulate an approximate relation between $\dot{\gamma}_p^{(\alpha)}$ and $\dot{\Gamma}_p^{(\alpha)}$ through the use of $\dot{\varepsilon}_{eq}^p\big|_\mu$ in a Taylor factor-type argument, i.e.

$$M_T \, \dot{\varepsilon}_{eq}^p\big|_\mu \approx \left| \sum_{\alpha=1}^{n_{slip}} \dot{\gamma}_p^{(\alpha)}\big|_\mu \right|, \tag{2.1.11}$$

where M_T denotes the Taylor factor with $\dot{\gamma}_p^{(\alpha)}\Big|_\mu$ denoting the additional microscale fluctuations on each slip rate.

Here, we assume that microscopic slip rate may be sufficiently approximated (for our purposes) as the areal average over the polar coordinates at a particular radial coordinate. Moreover, it is assumed that the contribution from the fluctuation field to the magnitude of each of these slip rates will necessarily be identical. As a result, our final approximation for the magnitude of the spatially-varying microscale slip rates is taken as the sum contributions of the corresponding macroscale slip rates and the microscale fluctuations, i.e.

$$\left|\dot{\gamma}_p^{(\alpha)}\right| = \left|\dot{\Gamma}_p^{(\alpha)}\right| + \frac{M_T}{n_{slip}}\left.\dot{\varepsilon}_{eq}^{p}\right|_{\mu}. \tag{2.1.12}$$

Here we choose the Taylor factor associated with randomly oriented crystals, i.e. $M_T \approx 3.06$ (Stoller and Zinkle, 2000), in Eq. (2.1.12) since spherical void growth has no preferred orientation.

2.2 Constitutive equations

2.2.1 Microscale constitutive equations

2.2.1.1 Crystal elasticity

The microscopic second Piola-Kirchhoff stress, **s**, is assumed to be linearly related to elastic strain, $\mathbf{e}^e$, through the fourth-order elastic stiffness tensor, $\mathbb{C}$, i.e $\mathbf{s} = \mathbb{C} : \mathbf{e}^e$. The microscale Cauchy stress $\boldsymbol{\sigma}$ is related to the microscale second Piola-Kirchhoff stress via $\boldsymbol{\sigma} = \det\left(\mathbf{f}^{e-1}\right)\mathbf{f}^e\mathbf{s}\mathbf{f}^{eT}$. For simplicity, we assume a linear dependence of the elastic constants on pressure p and temperature ϑ.

$$C_{ijkl} = C_{ijkl}^0 + \frac{\partial C_{ijkl}}{\partial p}p + \frac{\partial C_{ijkl}}{\partial \vartheta}\left(\vartheta - \vartheta_0\right), \tag{2.2.1}$$

with C_{ijkl}^0 denoting the corresponding elastic constants at ambient pressure and temperature, i.e. $\vartheta_0 = 300\text{K}$.

2.2.1.2 Dislocation-based crystal plasticity

The total dislocation density $\varrho^{(\alpha)}$ on each α-th slip system is assumed to additively decompose into mobile and immobile populations:

$$\varrho^{(\alpha)} = \varrho_m^{(\alpha)} + \varrho_{im}^{(\alpha)}, \tag{2.2.2}$$

with subscripts m and im denoting the mobile and immobile populations, respectively. The microscale slip rate on each slip system is accommodated by the mean velocity $v_{\perp}^{(\alpha)}$ of mobile dislocations via Orowan's equation, i.e.

$$\dot{\gamma}_{p}^{(\alpha)} = b\varrho_{m}^{(\alpha)} v_{\perp}^{(\alpha)} \,, \tag{2.2.3}$$

with b denoting the magnitude of the Burger's vector. In this work, we adopt a mobility law suitable for the drag-dominated regime:

$$\left\{ \left| \tau^{(\alpha)} \right| - \tau_{cr}^{(\alpha)} \right\} \operatorname{sgn}\left(\tau^{(\alpha)} \right) = \frac{B_0}{b} \frac{v_{\perp}^{(\alpha)}}{1 - \left(v_{\perp}^{(\alpha)} / c_s^{(\alpha)} \right)^2} \,, \tag{2.2.4}$$

with B_0 denotes the drag coefficient at rest, $\tau^{(\alpha)}$ denotes the resolved shear stress, $\tau_{cr}^{(\alpha)}$ denotes the critical resolved shear stress, $c_s^{(\alpha)}$ denotes the shear wave speed along the α-th slip direction.

2.2.1.3 Nonlocal microscale hardening law

Here, we modify Taylor's hardening law to describe the hardening of the solid matrix material. Since the local nature of $\tau_{cr}^{(\alpha)}$ may be a poor approximation on the small length-scales associated with void growth, we modify $\tau_{cr}^{(\alpha)}$ here to approximate the long-range interaction of spatially-varying effective dislocation density, i.e.

$$\tau_{cr}^{(\alpha)}(\mathbf{x}) = \tau_0 + \int_0^{\infty} c_{\perp} \mu^{(\alpha)} b \sqrt{\varrho_{eff}^{(\alpha)}(\mathbf{y})}\, g\left(||\mathbf{y} - \mathbf{x}|| \right) d\, ||\mathbf{y} - \mathbf{x}||. \tag{2.2.5}$$

τ_0 denotes the Peierls stress, $\mu^{(\alpha)}$ denotes the shear modulus along the α-th slip system, and $c_{\perp}$ being a proportionality constant. The effective dislocation density is determined

from an interaction matrix, i.e.

$$\varrho_{eff}^{(\alpha)} = \sum_{\beta=1}^{n_{slip}} a_{\alpha\beta}\varrho^{(\beta)} \ , \tag{2.2.6}$$

with $a_{\alpha\beta}$ being the components of the $n_{slip} \times n_{slip}$ hardening interaction matrix, e.g. 12×12 for face-centered cubic crystals. For simplicity, we choose typical values (Kocks, 1970; Asaro, 1983) of unity along the diagonal (self-hardening) and 1.4 for off-diagonal entries (latent hardening), which was also justified by Kubin et al. (2008) in the absence of detailed data. $g\left(||\mathbf{y}-\mathbf{x}||\right)$ is a nonlocal kernel function that determines the influence of effective dislocation density at some arbitrary microscopic material point $\mathbf{y}$ on the critical resolved shear stress at $\mathbf{x}$ with $||\mathbf{y}-\mathbf{x}||$ denoting the distance between these two points. For convenience we employ a *top-hat* function with non-zero (constant) values inside the particular spherical shell under analysis, i.e.

$$\tau_{cr}^{(\alpha)} = \tau_0 + \frac{1}{\ell_v - a}\int_a^{\ell_v} c_{\perp}\mu^{(\alpha)} b\sqrt{\varrho_{eff}^{(\alpha)}}\, dr. \tag{2.2.7}$$

While Eq. (2.2.7) is certainly a crude approximation, it is our claim here that it may capture more of the pertinent physics of hardening associated with long-range interactions than a purely local approximation. Furthermore, it is shown in section 2.3 that Eq. (2.2.7) is mathematically convenient as it permits an analytic approximation that greatly reduces the computational overhead otherwise required.

2.2.1.4 Dislocation substructure evolution equations

To model the evolution of dislocation density during loading, we adopt dislocation substructure evolution equations similar to those proposed in Austin and McDowell (2011); Lloyd et al. (2014b); Luscher et al. (2017) with some modifications. In particular, the

evolution of mobile dislocation density is taken to be the resultant of the following mechanisms: (i) multiplication of mobile dislocation segments; (ii) trapping of mobile dislocation segments rendering them immobilized; (iii) mutual annihilation of mobile segments with opposite signed co-planar mobile or immobile dislocations; (iv) nucleation of fresh new dislocation segment. These mechanisms are approximated by the following microscale evolution equations:

$$\dot{\varrho}_m^{(\alpha)} = \dot{\varrho}_{mult}^{(\alpha)} + \dot{\varrho}_{nuc}^{(\alpha)} - \dot{\varrho}_{trap}^{(\alpha)} - \dot{\varrho}_{ann}^{m(\alpha)} - \dot{\varrho}_{ann}^{im(\alpha)} \tag{2.2.8}$$

$$\dot{\varrho}_{im}^{(\alpha)} = \dot{\varrho}_{trap}^{(\alpha)} - \dot{\varrho}_{ann}^{im(\alpha)}, \tag{2.2.9}$$

where subscripts $mult$, $trap$, ann and nuc denote these mechanisms, respectively. Suitable, albeit simple, approximate statistical models for the remaining substructure evolution equations are proposed here motivated by the work of Austin and McDowell (2011); Lloyd et al. (2014b); Luscher et al. (2017), i.e.

$$\dot{\varrho}_{mult}^{(\alpha)} = \frac{c_{mult}}{b^2}\left|\dot{\gamma}_p^{(\alpha)}\right| \tag{2.2.10}$$

$$\dot{\varrho}_{trap}^{(\alpha)} = \frac{c_{trap}}{b}\sqrt{\varrho_f^{(\alpha)}}\left|\dot{\gamma}_p^{(\alpha)}\right| \tag{2.2.11}$$

$$\dot{\varrho}_{ann}^{m(\alpha)} = c_{ann}^{m}\varrho_m^{(\alpha)}\left|\dot{\gamma}_p^{(\alpha)}\right| \tag{2.2.12}$$

$$\dot{\varrho}_{ann}^{im(\alpha)} = c_{ann}^{im}\varrho_{im}^{(\alpha)}\left|\dot{\gamma}_p^{(\alpha)}\right|, \tag{2.2.13}$$

where c_{mult}, c_{trap}, c_{ann}^{m} and c_{ann}^{im} are material constants with values representative of pure copper provided in Table 2.1. $\varrho_f^{(\alpha)}$ denotes the forest dislocation density on the α-th slip system, which is geometrically computed considering the total density of dislocations that

pierce through a particular slip system (Ma and Roters, 2004), i.e.

$$\varrho_f^{(\alpha)} = \sum_{\beta=1}^{n_{slip}} A_f^{\alpha\beta} \varrho^{(\beta)} \quad \text{with} \quad A_f^{\alpha\beta} \triangleq \frac{1}{2}\left|\mathbf{n}^{(\alpha)} \cdot \mathbf{s}^{(\beta)}\right| + \frac{1}{2}\left|\mathbf{n}^{(\alpha)} \cdot \left(\mathbf{n}^{(\beta)} \times \mathbf{s}^{(\beta)}\right)\right|, \quad (2.2.14)$$

where both edge and screw character dislocation densities have been assumed to exist in roughly equal proportion (Luscher et al., 2017).

It is known that dislocations can be homogeneously nucleated within the lattice under shock compression, reportedly at shock pressures as low as 15GPa (Austin and McDowell, 2012). Heterogeneous nucleation is known to occur in polycrystals and single crystals with impurities at much lower pressures (Austin and McDowell, 2011). Here we focus attention on incorporation of a heterogeneous dislocation nucleation term, although the framework and numerical implementation readily admits a source term for homogeneous nucleation as well.

Austin and McDowell (2012) proposed a relatively simple stress-based expression for the heterogeneous nucleation of dislocations, further extended to crystal plasticity by Lloyd et al. (2014b), i.e.,

$$\dot{\varrho}_{nuc}^{(\alpha)} = \alpha_{het}|\dot{\tau}^{(\alpha)}| \left(m_{het}+1\right) \frac{\left(|\tau^{(\alpha)}| - \tau_{min}\right)^{m_{het}}}{\left(\tau_{max} - \tau_{min}\right)^{m_{het+1}}} \quad (2.2.15)$$

where α_{het} is the scaling coefficient, m_{het} is a scalar parameter that defines the shape of the stress barrier to heterogeneous dislocation nucleation, which depends upon the current resolved shear stress $\tau^{(\alpha)}$, its rate $\dot{\tau}^{(\alpha)}$, and τ_{min} and τ_{max} are the lower and upper shear stress threshold for this mechanism to be activated. The nucleation parameters used here are those from Austin and McDowell (2012) with some adjustments for the present application to single crystals rather than polycrystalline copper.

Given Eqs. (2.2.8)–(2.2.13) it follows that the microscale spatial variation of the dislo-

Table 2.1: Material properties and substructure evolution parameters representative of single crystal pure copper.

Properties	Value	Units	Parameters	Value	Units
ρ_s	8.94×10^3	kg$-$m^{-3}	c_{mult}	8.96×10^{-5}	$-$
b	2.56	Å	c_{trap}	3×10^{-3}	$-$
$c_s^{(\alpha)}$	2.14	km$-$ s^{-1}	c_{ann}^{m}	0.5	$-$
B_0	30	μPa$-$s	c_{ann}^{im}	0.5	$-$
τ_0	10	MPa	$c_{\perp}$	0.5	$-$
$\mu^{(\alpha)}$	41	GPa	M_T	3.06	$-$

cation density will evolve in accordance with the microscale spatial variation of the magnitude of the microscale slip rates $\left|\dot{\gamma}_p^{(\alpha)}\right|$, which in turn are approximated here as a function of the macroscale slip rates $\left|\dot{\Gamma}_p^{(\alpha)}\right|$ and the approximate fluctuation field as prescribed in Eq. (2.1.12). This provides one key bridge between the microscale and macroscale with further linkages developed in the subsequent subsection.

2.2.2 Macroscale constitutive equations

2.2.2.1 Porous crystal elasticity

Here we adopt the notion of a macroscopic stress and strain that are taken to be the volume average of the microscopic stress and strain. Such notions are commonly adopted and are described in further detail elsewhere, e.g. Qu and Cherkaoui (2006). To denote volume averages over the microscale domain Ω_{micro} we make use of typical notation: $\langle f \rangle = \Omega_{micro}^{-1} \iiint_{\Omega_{micro}} f d\Omega_{micro}$. Additionally, we utilize a superscript s to denote a volume average over the microscale domain Ω_{micro}^s containing only the solid matrix material, i.e. $\langle f \rangle^s = {\Omega_{micro}^s}^{-1} \iiint_{\Omega_{micro}^s} f d\Omega_{micro}^s$. Following this notation, the macroscale Cauchy stress denoted as $\boldsymbol{\Sigma}$ is equal to the corresponding microscale volume average, i.e. $\boldsymbol{\Sigma} = \langle \boldsymbol{\sigma} \rangle$. Likewise, the macroscale Green-Lagrange elastic strain tensor $\mathbf{E}^e$ is related to

the microscale via $\mathbf{E}^e = \langle \mathbf{e}^e \rangle$. Moreover, since the microscale domain including only the voids is stress free it follows that $\boldsymbol{\Sigma} = (1-\varphi)\,\langle \boldsymbol{\sigma} \rangle^s$.

As with the microscale, the macroscale second Piola-Kirchhoff stress, $\mathbf{S}$, which is related to the macroscale Cauchy stress via $\boldsymbol{\Sigma} = J^{e-1}\mathbf{F}^e\mathbf{S}\mathbf{F}^{eT}$, is taken here to be a linear function of the macroscale Green-Lagrange elastic strain:

$$\mathbf{S} = \mathbb{C}^d : \mathbf{E}^e, \tag{2.2.16}$$

where $\mathbb{C}^d$ denotes the fourth-order damaged elastic stiffness tenor. Here our porous media may be considered as a two-phase composite with one phase (the voids) possessing nil stiffness and the other phase (solid matrix material) possessing a stiffness of $\mathbb{C}$. Mori and Tanaka (1973) derived an elegant approximation for $\mathbb{C}^d$ for such two-phase composites, i.e.

$$\mathbb{C}^d = (1-\varphi)\,\mathbb{C}\big(\varphi(\mathbb{I}-\mathbb{S})^{-1} + (1-\varphi)\,\mathbb{I}\big)^{-1} \tag{2.2.17}$$

with $\mathbb{I}$ denoting the fourth-order identity tensor and $\mathbb{S}$ denotes the fourth-order Eshelby tensor. A closed-form solution for $\mathbb{S}$ for the special case of spherical voids embedded with a cubic material have been developed elsewhere, e.g. Lin and Mura (1973); Mura (2013).

2.2.2.2 Macroscopic dislocation-based crystal plasticity

We now turn our attention to the formulation of an adequate model to determine the evolution of the macroscale plastic velocity gradient tensor in the intermediate plastic configuration, $\tilde{\mathbf{L}}^p$ as a function of the macroscale stress. $\tilde{\mathbf{L}}^p$ governs the deformation from the intermediate damaged configuration $\mathcal{B}_d$ to the intermediate plastic configuration $\mathcal{B}_d$. In our formulation, this deformation is assumed to be affine and unperturbed by microscale heterogeneities (voids). As such, we assume here that the evolution of $\tilde{\mathbf{L}}^p$ is governed by a uniform average measure of the Cauchy stress in the solid matrix material, i.e. $\langle \boldsymbol{\sigma} \rangle^s$.

Note that $\langle \boldsymbol{\sigma} \rangle^s$ is an amplification of the macroscale Cauchy stress by a factor $(1-\varphi)^{-1}$, i.e. $\langle \boldsymbol{\sigma} \rangle^s = (1-\varphi)^{-1} \boldsymbol{\Sigma}$; which provides one mechanism for the porosity φ to influence (accelerate) the evolution of $\tilde{\mathbf{L}}^p$.

Taking this uniform average stress as the driving force, a corresponding uniform effective dislocation velocity $\mathcal{V}_{\perp}^{(\alpha)}$ associated with $\tilde{\mathbf{L}}^p$ may be computed from a mobility relation similar to Eq. (2.2.4), i.e.

$$\left\{ \left| T_s^{(\alpha)} \right| - T_{cr}^{(\alpha)} \left(T_s^{(\alpha)}, \boldsymbol{\Sigma}, \varphi \right) \right\} \operatorname{sgn} \left(T_s^{(\alpha)} \right) = \frac{B_0}{b} \frac{\mathcal{V}_{\perp}^{(\alpha)}}{1 - \left(\mathcal{V}_{\perp}^{(\alpha)} / c_s^{(\alpha)} \right)^2}, \tag{2.2.18}$$

where $T_s^{(\alpha)}$ and $T_{cr}^{(\alpha)}$ denote the effective uniform resolved shear stress and the effective uniform critical resolved shear stress, respectively. $T_{cr}^{(\alpha)} \left(T_s^{(\alpha)}, \boldsymbol{\Sigma}, \varphi \right)$ is a non-negative scalar-valued function that accounts for the possibility of additional softening of the macroscale yield criterion due to porosity and other stress measures, e.g. first, second, and third macroscale stress invariants. An analytical formulation for $T_{cr}^{(\alpha)}$ will be provided in subsubsection 2.2.2.4. The effective resolved shear stress is computed via contraction of $\langle \boldsymbol{\sigma} \rangle^s$ on the Schmid tensor in the current macroscale configuration, i.e. $T_s^{(\alpha)} = \langle \boldsymbol{\sigma} \rangle^s : \left(\mathbf{S}^{(\alpha)} \otimes \mathbf{N}^{(\alpha)} \right)$. For simplicity, the effective uniform critical resolved shear stress ($T_{cr}^{(\alpha)}$) can be assumed to be the solid matrix domain volume average of the microscale critical resolved shear stress, i.e.

$$T_{cr}^{(\alpha)} = \left\langle \tau_{cr}^{(\alpha)} \right\rangle^s = \tau_0 + \frac{1}{\ell_v - a} \int_a^{\ell_v} c_{\perp} \mu^{(\alpha)} b \sqrt{\varrho_{eff}^{(\alpha)}} \, dr. \tag{2.2.19}$$

Likewise, the effective macroscale mobile dislocation density is taken as the solid matrix domain volume average of the α-th microscale mobile dislocation density, i.e. $\langle \varrho_m^{(\alpha)} \rangle^s$, for which a scheme will be proposed in section 2.3 to compute $\langle \varrho_m^{(\alpha)} \rangle^s$ via interpolation

functions. The macroscale slip rate follows the ensuing macroscale Orowan's equation, i.e. $\dot{\Gamma}_p^{(\alpha)} = b\langle \varrho_m^{(\alpha)} \rangle^s \mathcal{V}_\perp^{(\alpha)}$. Substitution of this macroscopic slip rate into Eq. (2.1.10), i.e.

$$\tilde{\mathbf{L}}^p = \sum_{\alpha=1}^{n_{slip}} b\langle \varrho_m^{(\alpha)} \rangle^s \mathcal{V}_\perp^{(\alpha)} \mathbf{s}_0^{(\alpha)} \otimes \mathbf{n}_0^{(\alpha)}, \tag{2.2.20}$$

completes the constitutive framework required to model the evolution of the plastic part of the macroscale deformation gradient tensor $\mathbf{F}^p$. It is worth noting that no new model parameters were introduced, as the development was based entirely on averaging concepts. In the next section, we develop a set of dynamic damage evolution equations necessary to compute the evolution of $\mathbf{F}^d$.

2.2.2.3 Dynamic evolution equation for porosity

The last remaining aspect of our macroscale constitutive framework is the development of a suitable model for the porosity evolution. Following the pioneering work of Knowles and Jakub (1965) and Carroll and Holt (1972), the balance of radial momentum of a spherically-symmetric, incompressible spherical shell subject to an external tensile pressure p_{out} (and nil applied pressure on the inner radius) may be expressed as

$$\rho_s \left(1 - \frac{a}{\ell_v}\right) a\ddot{a} + \rho_s \left(\frac{3}{2} - 2\frac{a}{\ell_v} + \frac{1}{2}\left(\frac{a}{\ell_v}\right)^4\right) \dot{a}^2 = p_{out} - \underbrace{\int_a^{\ell_v} \frac{2}{r}\sigma_{eq}\, dr}_{\triangleq \mathcal{R}}, \tag{2.2.21}$$

where ρ_s denotes the mass density of the solid matrix material and the equivalent Mises stress. $\mathcal{R}$ captures the material-specific resistance of the solid matrix material to isochoric deformation. Following the arguments of Wright and Ramesh (2008), we extend Eq. (2.2.21) to porous media by replacing p_{out} with the mean macroscale Cauchy stress Σ_m and replace the inner radius of the representative spherical shell with the porosity in

the intermediate damaged configuration, i.e.

$$\frac{1}{3}\rho_s \ell_v^2 \left(\frac{1-\sqrt[3]{\varphi}}{\sqrt[3]{\varphi}(1-\varphi)}\ddot{\varphi} - \frac{1-12\varphi+11\varphi^{4/3}}{6\varphi^{4/3}(1-\varphi)^2}\dot{\varphi}^2 \right) = (\Sigma_m - \mathcal{R}) \operatorname{sgn}\{\dot{\varphi}\}, \tag{2.2.22}$$

where ℓ_v preserves the length-scale dependence. Note that the function $\operatorname{sgn}\{\dot{\varphi}\}$ has been appended to the net driving force to artificially prevent reverse yielding of the solid matrix, which is not necessarily adequately captured by Eq. (2.2.21), see Wright and Ramesh (2008) for more details on this aspect.

The microscale crystal plasticity constitutive equations outlined in Eqs. (2.2.1)–(2.2.14) are relatively complex for obtaining a concise closed-form solution. The subsequent section is devoted to obtaining a closed-form approximation to $\mathcal{R}$ that will reduce Eq. (2.2.22) to a simple, second-order ordinary differential equation.

2.2.2.4 Degradation of the macroscopic CRSS using a porosity dependent single crystal yield function

Our macroscopic dislocation-based crystal plasticity presented in subsubsection 2.2.2.2 could likely not accurately reproduce the observed crystallographic orientation dependence of the far-field deviatoric stresses under simple-shear deformation modes. This is because of the approximation made in the former model that the shear stresses driving crystallographic slip throughout the crystal are unaffected by the presence of the void. In reality, the void does affect the distribution of shear stresses throughout the crystal. Alternately, this can be viewed as a degradation to the effective macroscale slip resistance, or critical resolved shear stress (CRSS), in terms of the far-field stresses. For example, for an isotropic perfectly-plastic material Gurson (1977) developed a well-known analytical expression for an approximate upper bound of the macroscopic threshold stress state for plastic deformation in the vicinity of a growing void. The Gurson yield surface and flow potential have been modified and used extensively to model void growth in isotropic

ductile metals including dynamic spallation (Tvergaard and Needleman, 1984; Johnson and Addessio, 1988; Wang and Jiang, 1997). The Gurson surface has also been extended for modeling pore growth in anisotropic single crystals by Han et al. (2013), Ling et al. (2016), and Paux et al. (2015, 2018), who have demonstrated the applicability of the yield function in this context by comparison with DNS of a unit cell containing a single void embedded within single crystal matrix. In order to account for this coupling omitted from our previous model, we extend the theory by using a modified Gurson surface to define a degraded macroscopic CRSS for each slip system according to

$$\left(\frac{T_{cr}^{(\alpha)}}{T_s^{(\alpha)}}\right)^2+\frac{2}{45}\chi\varphi\left(\frac{\Sigma_{eq}}{T_s^{(\alpha)}}\right)^2+2q_1\varphi\cosh\left[q_2\sqrt{\frac{3}{20}}\frac{\Sigma_m}{T_s^{(\alpha)}}\sqrt[5]{\frac{\Sigma_{eq}}{T_s^{(\alpha)}}}\right]-1-q_1^2\varphi^2=0. \quad (2.2.23)$$

Noting the traditional decomposition of the macroscale Cauchy stress into mean and deviatoric components, $\mathbf{\Sigma}=\Sigma_m\mathbf{I}+\mathbf{\Sigma}'$ where $\Sigma_m=\text{Trace}\mathbf{\Sigma}/3$ is the mean stress, $\Sigma_{eq}=\sqrt{3/2\mathbf{\Sigma}':\mathbf{\Sigma}'}$, the void volume fraction is denoted by φ, and q_1 and q_2 are the GTN (Tvergaard and Needleman, 1984) model parameters. The term including the parameter χ was added by Han et al. (2013) to extend the applicability of the GTN (Tvergaard and Needleman, 1984) surface to crystal plasticity (i.e. anisotropic plasticity). We have further modified the argument of the cosh function to include a scaling by $\sqrt[5]{\frac{\Sigma_{eq}}{T_s^{(\alpha)}}}$ in order to reduce the effect of mean stress Σ_m when the ratio of hydrostatic stress and equivalent stress (stress triaxiality) is large, such as encountered under uniaxial strain loading associated with spallation. Han et al. (2013) used this expression to solve for the effective macroscopic resolved shear stress ($T_s^{(\alpha)}$, i.e. the denominator on the first term from the left of Eq. (2.2.23)). Here, we are instead using the expression to identify an effective degraded macropscopic CRSS in terms of the macrosopic resolved shear stress $T_s^{(\alpha)}$, mean stress Σ_m, equivalent stress Σ_{eq} and porosity φ. The phenomenological relationship implied by

Eq. (2.2.23) is consistent between our approach and that of Han et al. (2013), but the connection with the remainder of the void growth and crystal plasticity behavior remains quite different.

2.2.2.5 Equation of state

Under increasingly larger shock pressures, the extension of linear thermoelasticy to include pressure- and temperature-dependent second-order elastic moduli becomes insufficient to describe the pressure, p, specific volume (per mass), v, and temperature, T, relationship necessary for adequately representing a shock wave (Luscher et al., 2013). For these larger amounts of compression, an equation of state (EOS) is more appropriate to describe this nonlinear thermoelastic behavior. However, for the range of the shock compression considered in the simulations presented in this dissertation (i.e. less than 15 GPa), the effect of temperature evolution on pressure is negligible (cf. Luscher et al., 2013, Fig. 1 for an example). Future improvements of this model to include the temperature evolution as in Luscher et al. (2018) will enable consideration of an extended range of loading conditions; here we ignore the effect of temperature evolution on pressure recognizing the restriction to present magnitudes of shock compression, such that the Mie-Grüneisen EOS for the solid matrix simplifies to

$$p_s^{eos} = \frac{K_0\chi_s(1-0.5\Gamma_0\chi_s)}{(1-s\chi_s)^2} + \rho_0\Gamma_0 E \tag{2.2.24}$$

In this equation, ρ_0 is the initial *solid matrix* mass density, K_0 is the ambient bulk modulus ($K_0 = \rho_0 C_0^2$ with C_0 is the bulk wave speed at rest), $\chi_s = 1 - \frac{\rho_0}{\rho_s} = 1 - \frac{J}{J_d}$, ρ_s is the current *solid matrix* mass density, Γ_0 is the Grüneisen parameter at initial state, s is the slope correlating shock velocity and particle velocity, E is the internal strain energy due to the compressed lattice per unit mass ($\dot{E} = \mathbf{S} : \dot{\mathbf{E}}$, where $\mathbf{S}$ is the second Piola-Kirchhoff

Table 2.2: Naming convention utilized here for face-centered cubic slip systems in reference configuration.

α	1	2	3	4	5	6	7	8	9	10	11	12
$\mathbf{n}_0^{(\alpha)}$	(111)	(111)	(111)	$(\bar{1}11)$	$(\bar{1}11)$	$(\bar{1}11)$	$(1\bar{1}1)$	$(1\bar{1}1)$	$(1\bar{1}1)$	$(\bar{1}\bar{1}1)$	$(\bar{1}\bar{1}1)$	$(\bar{1}\bar{1}1)$
$\mathbf{s}_0^{(\alpha)}$	$[1\bar{1}0]$	$[\bar{1}01]$	$[01\bar{1}]$	[101]	$[\bar{1}\bar{1}0]$	$[01\bar{1}]$	$[\bar{1}01]$	$[0\bar{1}\bar{1}]$	[110]	$[\bar{1}10]$	[101]	$[0\bar{1}\bar{1}]$

stress and $\mathbf{E}$ is the Green-Lagrange strain). The macroscopic mean stress on the porous volume element can be scaled down by $\Sigma_m = -(1-\varphi)p_s^{eos}$, which is consistent with our volume average notion for *macroscopic* stress here.

2.3 Closed-form approximations via reduced-order dislocation-based crystal plasticity

For a class of constitutive relations that additively decompose similar to Eq. (2.2.4), Wilkerson and Ramesh (2014) argued that $\mathcal{R}$ may be additively decomposed, i.e. $\mathcal{R} = \mathcal{R}_{cr} + \mathcal{R}_{dd}$. Here, $\mathcal{R}_{cr}$ denotes the quasi-static critical resistance associated with the quasi-static yield strength, i.e. $\tau_{cr}^{(\alpha)}$, and $\mathcal{R}_{dd}$ denotes the viscoplastic resistance associated with the visoplastic over-stress, i.e. $\tau^{(\alpha)} - \tau_{cr}^{(\alpha)}$. The crystal plasticity relations in Eqs. (2.2.1)–(2.2.14) used to represent the microscale response are more complicated than the J_2 viscoplasticity used by Wilkerson and Ramesh, 2014. While the latter enabled a simple closed-form expression, here we develop accurate approximations of $\mathcal{R}_{cr}$ and $\mathcal{R}_{dd}$ for single crystals that obviates some of the unnecessary complexity. Toward this aim, it is necessary to first propose a reduced-order dislocation-based crystal plasticity model that is more amenable to such analytic solutions.

2.3.1 Reduced-order dislocation-based crystal plasticity

Consider representing the full crystal plasticity constitutive equations, i.e. Eqs. (2.2.1)–(2.2.14), by a sufficiently accurate approximation between equivalent Mises stress, σ_{eq},

and equivalent plastic strain rate, $\dot{\varepsilon}^{p}_{eq}$, of a similar functional form to the J_2 relations utilized in Wilkerson and Ramesh (2014), i.e.

$$\{\sigma_{eq} - \sigma_y\} \propto \frac{B_0}{b} \frac{v^{eq}_{\perp}}{1 - (v^{eq}_{\perp}/c_s)^2}, \tag{2.3.1}$$

where σ_y denotes the yield strength and $v^{eq}_{\perp}$ is an effective scalar measure of the magnitude of dislocation velocities on the various active slip systems. Similarly, we define an effective scalar measure of the mobile dislocation density, i.e. ϱ^{eq}_{m}, such that the equivalent plastic strain rate may be expressed by an Orowan-type relation, i.e.

$$\dot{\varepsilon}^{p}_{eq} = b \varrho^{eq}_{m} v^{eq}_{\perp}. \tag{2.3.2}$$

Ideally, a weighting average scheme for ϱ^{eq}_{m} and $v^{eq}_{\perp}$ could be developed such that these two simple relations will produce the same equivalent stress – equivalent strain rate relation as the full crystal plasticity equations, i.e. Eqs. (2.2.1)–(2.2.14). Here I simply approximate the equivalent mobile dislocation density:

$$\varrho^{eq}_{m} = \zeta^{[ijk]} \sqrt{\frac{1}{n_{act}} \sum_{\alpha \in \{act\}} \left(\varrho^{(\alpha)}_{m} \right)^2}, \tag{2.3.3}$$

with $\zeta^{[ijk]}$ denotes the inverse Schmid factor for particular loading direction.

2.3.2 Closed-form approximation of $\mathcal{R}_{dd}$

I now turn our attention to the development of a similarly simple modified J_2 theory that is appropriate for utilization in $\mathcal{R}_{dd}$. Here I propose the following modified J_2 theory to approximate the equivalent stress in the single crystalline material surrounding a

dynamically growing void:

$$\{\sigma_{eq} - \sigma_y\} = M_T \frac{\zeta^{rand}_{v_\perp \to c_s}}{\zeta^{rand}_{v_\perp/c_s \to 0}} \frac{B_0}{b} \frac{\dfrac{\dot{\varepsilon}^p_{eq}}{b\varrho^{eq}_m}}{1 - \left(\dfrac{\dot{\varepsilon}^p_{eq}}{b\varrho^{eq}_m c_s}\right)^2}, \tag{2.3.4}$$

with $\zeta^{rand}_{v_\perp \to c_s} = 2.83$, $\zeta^{rand}_{v_\perp/c_s \to 0} = 2.07$ denote the inverse Schmid factor for loading in random orientation of fcc crystal when dislocation velocity approach shear wave speed and zero respectively. Effective mobile dislocation density is expressed as,

$$\varrho^{eq}_m = \zeta^{rand}_{v_\perp \to c_s} \sqrt{\frac{1}{n_{slip}} \sum_{\alpha_{slip}=1}^{n_{slip}} \left(\varrho_m^{(\alpha_{slip})}\right)^2}, \tag{2.3.5}$$

With our modified J_2 theory in hand, i.e. Eqs. (2.3.4) and (2.3.5), we return to $\mathcal{R}_{dd}$, which is defined as the part of $\mathcal{R}$ (expressed in Eq. (2.2.21)) associated with the over-stress $\sigma_{eq} - \sigma_y$ in the intermediate damaged configuration, i.e.

$$\mathcal{R}_{dd} \triangleq \int_{a_p}^{\ell^p_v} \frac{2}{r_p} \{\sigma_{eq} - \sigma_y\}\, dr_p = M_T \frac{\zeta^{rand}_{v_\perp \to c_s}}{\zeta^{rand}_{v_\perp/c_s \to 0}} \frac{B_0}{b} \int_{a_p}^{\ell^p_v} \frac{2}{r_p} \frac{\dfrac{\dot{\varepsilon}^p_{eq}\big|_\mu}{b\varrho^{eq}_m}}{1 - \left(\dfrac{\dot{\varepsilon}^p_{eq}\big|_\mu}{b\varrho^{eq}_m c_s}\right)^2} dr_p, \tag{2.3.6}$$

where Eq. (2.3.4) has been substituted into the integral definition of $\mathcal{R}_{dd}$. Moreover, given that $\mathcal{R}$ in Eq. (2.2.21) provides the constitutive resistance to spherical void growth in the intermediate damage configuration, the associated microscale plastic rate $\dot{\varepsilon}^p_{eq}\big|_\mu$ is employed in Eq. (2.3.6). In order to evaluate the integral in Eq. (2.3.6), the spatial dependence of $\dot{\varepsilon}^p_{eq}\big|_\mu$ and ϱ^{eq}_m must be prescribed as a function of the microscale intermediate plastic radial coordinate r_p. Recall that the spatial dependence of $\dot{\varepsilon}^p_{eq}\big|_\mu$ is known to decay with the inverse cube of r_p according to Eq. (2.1.8). However, the spatial dependence of the

equivalent mobile dislocation density is unknown *a priori*, as it evolves according to the dislocation density evolution equations outlined in Eqs. (2.2.8)–(2.2.14). That said, Wilkerson and Ramesh (2014) demonstrated that an integral of the form shown in Eq. (2.3.6) may be obtained in closed-form for a family of power-law functions describing the spatial distribution of ϱ_m^{eq}, i.e.

$$\varrho_m^{eq} = \tilde{\varrho}_m^{eq} \left(\frac{r_p}{a_p} \right)^{\eta}, \tag{2.3.7}$$

with η denoting an unknown power-law exponent and the $\tilde{\varrho}_m^{eq}$ denoting the equivalent mobile dislocation density at the void surface ($r_p = a_p$). Likewise, $\hat{\varrho}_m^{eq}$ denotes the equivalent mobile dislocation density at $r_p = \ell_v^p$. Here I will utilize $\tilde{\cdot}$ and $\hat{\cdot}$ to generally denote such evaluations of a microscale field quantity at a particular microscale spatial location, i.e. ($r_p = a_p$) and ($r_p = \ell_v^p$), respectively. Taking the spatial dependence of ϱ_m^{eq} to follow Eq. (2.3.7) and the spatial dependence of $\dot{\varepsilon}_{eq}^p\big|_\mu$ to follow Eq. (2.1.8), a closed-form solution for $\mathcal{R}_{dd}$ is readily obtainable, i.e.

$$\mathcal{R}_{dd} = \frac{M_T}{3+\eta} \frac{\zeta_{v_\perp \to c_s}^{rand}}{\zeta_{v_\perp/c_s \to 0}^{rand}} \frac{B_0}{b} \ln \left| \frac{b\tilde{\varrho}_m^{eq} c_s + \frac{2}{3} \frac{|\dot{\varphi}|}{\varphi - \varphi^2}}{b\tilde{\varrho}_m^{eq} c_s - \frac{2}{3} \frac{|\dot{\varphi}|}{\varphi - \varphi^2}} \cdot \frac{b\tilde{\varrho}_m^{eq} c_s - \frac{2}{3} \frac{|\dot{\varphi}|\, \varphi^{\eta/3}}{1-\varphi}}{b\tilde{\varrho}_m^{eq} c_s + \frac{2}{3} \frac{|\dot{\varphi}|\, \varphi^{\eta/3}}{1-\varphi}} \right| \tag{2.3.8}$$

for $\eta \neq -3$ with φ denoting porosity as before.

The question remains, if we are to make use of Eq. (2.3.8) what is the appropriate choice for η? Our strategy here is to treat Eq. (2.3.7) as an interpolation function between two known values of the equivalent dislocation density ϱ_m^{eq}, namely $\tilde{\varrho}_m^{eq}$ and $\hat{\varrho}_m^{eq}$. In our approach, the values of $\tilde{\varrho}_m^{(\alpha)}$ and $\hat{\varrho}_m^{(\alpha)}$ are explicitly computed at each time step according to their respective evolution equations, i.e. Eq. (2.1.12) and Eqs. (2.2.8)–(2.2.14) appended with $\tilde{\cdot}$ and $\hat{\cdot}$ over all associated microscale field quantities. For example, the evolution of $\tilde{\varrho}_m^{(\alpha)}$ is driven by the plastic slip rate at the void surface $\dot{\tilde{\gamma}}_p^{(\alpha)}$ and, likewise, the evolution of

$\hat{\varrho}_m^{(\alpha)}$ is driven by the plastic slip rate $\dot{\hat{\gamma}}_p^{(\alpha)}$ at $r_p = \ell_v^p$; then $\tilde{\varrho}_m^{eq}$ and $\hat{\varrho}_m^{eq}$ are similarly known via Eq. (2.3.5). In addition to evaluation at these two microscale spatial locations, such a computational procedure may be utilized to compute ϱ_m^{eq} at any other number of microscale spatial locations. Clearly this can quickly become quite computationally burdensome; therefore, I assume that all unknown values of the microscale field quantity ϱ_m^{eq} fall near enough to the interpolation function to be suitably approximated by it. As such, η is purposefully chosen such that it forces the value of Eq. (2.3.7) at $r_p = l_v^p$ to be exactly equal to its known value $\hat{\varrho}_m^{eq}$, i.e.

$$\eta = \ln^{-1} \varphi \ln \frac{\tilde{\varrho}_m^{eq}}{\hat{\varrho}_m^{eq}}. \tag{2.3.9}$$

2.3.3 Closed-form approximation of $\mathcal{R}_{cr}$

I turn our attention to the development of an approximation of $\mathcal{R}_{cr}$, which denotes the quasi-static critical resistance associated with the quasi-static yield strength, i.e. $\tau_{cr}^{(\alpha)}$. Following our modified J_2 approach outlined in subsection 2.3.2, I seek an approximation for a J_2 measure of quasi-static yield strength, i.e. σ_y, as a weighted average of the critical resolved shear stress on all n_{slip} slip systems. As with $\mathcal{R}_{dd}$, here I invoke a Taylor-type approximation:

$$\sigma_y = M_T \frac{\sum_{\alpha=1}^{n_{slip}} \tau_{cr}^{(\alpha)} \left| \dot{\gamma}_p^{(\alpha)} \right|}{\sum_{\alpha=1}^{n_{slip}} \left| \dot{\gamma}_p^{(\alpha)} \right|}. \tag{2.3.10}$$

For the purpose of computing $\mathcal{R}_{cr}$, I further assume that the magnitude of the microscale slip rate is much larger than the macroscale slip rate, i.e. $\left| \dot{\gamma}_p^{(\alpha)} \right| \gg \left| \dot{\Gamma}_p^{(\alpha)} \right|$. Given this approximation, Eq. (2.3.10) simplifies to $\sigma_y \approx M_T n_{slip}^{-1} \sum_{\alpha=1}^{n_{slip}} \tau_{cr}^{(\alpha)}$, where Eq. (2.1.12) has

been employed. The approximation for quasi-static critical resistance is thus expressed as

$$\mathcal{R}_{cr} \triangleq \int_{a_p}^{\ell_v^p} \frac{2}{r_p}\sigma_y \, dr_p = \frac{M_T}{n_{slip}} \int_{a_p}^{\ell_v^p} \frac{2}{r_p} \sum_{\alpha=1}^{n_{slip}} \tau_{cr}^{(\alpha)} \, dr_p. \tag{2.3.11}$$

In general $\tau_{cr}^{(\alpha)}$ spatially varies across the microscale domain, thereby limiting the evaluation of Eq. (2.3.11) to numerical approaches. However, here I have chosen a particular nonlocal hardening law, i.e. Eq. (2.2.7), which enables an exact integration of Eq. (2.3.11):

$$\mathcal{R}_{cr} = \frac{2}{3}\frac{M_T}{n_{slip}} \ln\left(\frac{1}{\varphi}\right) \sum_{\alpha=1}^{n_{slip}} \tau_{cr}^{(\alpha)}. \tag{2.3.12}$$

While this solution is a convenient approximation of $\mathcal{R}_{cr}$ from a computational expediency standpoint, a numerical approximation of the integral in Eq. (2.2.7) is nevertheless required to close the framework. Given current values for the effective dislocation density at inner and outer surface of the spherical shell, integration of Eq. (2.2.7) may be obtained through any suitable numerical integration technique, e.g.

$$\tau_{cr}^{(\alpha)} = \tau_0 + \frac{1}{2} c_{\perp} \mu^{(\alpha)} b \left(\sqrt{\varrho_{eff}^{(\alpha)}\Big|_{r_p=\ell_v^p}} + \sqrt{\varrho_{eff}^{(\alpha)}\Big|_{r_p=a_p}} \right). \tag{2.3.13}$$

One subtle issue associated with the solution of $\mathcal{R}_{cr}$ expressed in Eq. (2.3.12) is the neglect of elasticity, which tends to slightly soften the critical resistance (Huang et al., 1991). In order to account for this second-order effect, I must modify the integrand in Eq. (2.3.11) to replace σ_y with $\min(\sigma_{eq}^e, \sigma_y)$, where σ_{eq}^e denotes the corresponding value of the equivalent stress if the total microscale deformation was purely elastic. For simplicity, I take this equivalent elastic stress as a linear approximation of the equivalent strain ε_{eq}, i.e. $\sigma_{eq}^e = 3\mu_{eq}\varepsilon_{eq}$ with μ_{eq} being an isotropic equivalent measure of the shear moduli. Here I take $\mu_{eq} = \mu^{(\alpha)}$ for lack of any better model. Following the same integral transformation

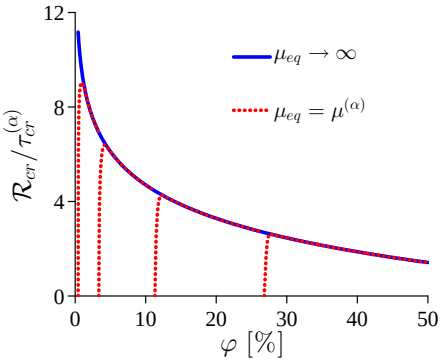

Fig. 2.2: Demonstration of the role of finite stiffness, i.e. $\mu_{eq} \neq \infty$, in softening the critical resistance term $\mathcal{R}_{cr}$ according to Eq. (2.3.14) (with $M_T = 3.06$ and $\tau_{cr}^{(\alpha)} = 310$ MPa). Each dotted line corresponds to a value of initial porosity: $\varphi_0 \in [4.19\times10^{-3}, 3.35\times 10^{-2}, 11.31 \times 10^{-2}, 26.81 \times 10^{-2}]$.

utilized by Huang et al. (1991), substitution of $\min(\sigma_{eq}^{e}, \sigma_y)$ in Eq. (2.3.11) leads to

$$\mathcal{R}_{cr} = 2 \int_{1}^{\sqrt[3]{1/\varphi}} \min\left(2\mu_{eq} \ln \frac{\xi^3}{\xi^3 + a_0^3/a^3 - 1}, \frac{M_T}{n_{slip}} \sum_{\alpha=1}^{n_{slip}} \tau_{cr}^{(\alpha)}\right) \frac{d\xi}{\xi}, \tag{2.3.14}$$

where $\xi = r/a$. In the limit of rigid elasticity, i.e. $\mu_{eq} \to \infty$, Eq. (2.3.12) is exactly recovered from Eq. (2.3.14). For finite elasticity, Eq. (2.3.14) approximates the second-order softening effects of elastic deformation on $\mathcal{R}_{cr}$ that are neglected in the closed-form solution expressed in Eq. (2.3.12). Figure 2.2 provides a comparison of these two approximations, i.e. Eq. (2.3.12) versus Eq. (2.3.14). Clearly, the correction factor is negligible in the late stages of void growth, i.e. $\varphi \gg \varphi_0$. However, in the earliest stages of void growth, i.e. $\varphi \sim \varphi_0$, $\mathcal{R}_{cr}$ may be over-estimated when the elastic correction is neglected. It is left to the user of this model to ascertain the necessity of accounting for the elastic correction in their particular application.

3. VALIDATION ASSESSMENT OF THE FRAMEWORK AGAINST DIRECT NUMERICAL SIMULATIONS

3.1 Material, geometry, and computational details

Here I focus our analysis on a porous face-centered cubic single crystal with a uniform distribution of spherical voids on a simple cubic lattice. An appropriately chosen representative volume element (RVE) for such a material is a single cubic unit cell (UC) comprising of a single spherical void embedded within a cube of homogeneous single crystal matrix subject to appropriate periodic boundary conditions. In the reference configuration $\mathcal{B}_0$, the chosen UC of interests has an undeformed length of $l_0 = 10$ μm along each edge and an undeformed void radius of a_0, thereby resulting in an initial porosity of $\varphi_0 = \frac{4}{3}\pi a_0^3 \ell_0^{-3}$. For the simulation results discussed in this section, I considered initial void sizes and initial porosity values of $a_0 \in [1, 2, 3, 4]$ μm.

The DNS involve the explicit determination of the *exact* microscale field quantities as determined through the solution of the microscale constitutive equations outlined in subsection 2.2.1, i.e. Eqs. (2.2.1)–(2.2.14). The microscale constitutive equations have been implemented as a user-defined subroutine (VUMAT) within Abaqus/explicit (Hibbit et al., 2012). The single crystal matrix material within the UC is discretized into a computational mesh of eight-node hexahedral elements employing linear shape functions and reduced integration, similar to the mesh depicted in Fig. 3.1. Details of the numerical algorithms utilized here may be found in Luscher et al. (2017). The macroscale constitutive

The present chapter is based on publication by Nguyen et al. (2017).

equations governing the CPD model, i.e. Eqs. (2.2.16)–(2.2.22) along with Eq. (2.3.8) and Eq. (2.3.14), have likewise been implemented into Abaqus/explicit via a separate VUMAT (see the appendix for implementation). Throughout the remainder of this section, comparisons between DNS and CPD are made for the same initial conditions (including void geometry and crystallographic orientation), macroscale geometry, and macroscale loading conditions in order to facilitate an appropriate comparison.

In the remainder of this section, DNS and CPD simulations will be carried out for macroscopically homogenous loading conditions, i.e. $\mathbf{Grad}(\mathbf{F}) = \mathbf{0}$. As such, the macroscale response predicted by the CPD framework may be modeled as a single cubic element with edge length equal to that of the UC (again making use of C3D8R elements in Abaqus). In both the DNS and CPD simulations, loading is achieved through displacement control by prescribing constant velocity boundary conditions on the external boundary, which is equivalent to controlling the macroscopic deformation gradient $\mathbf{F}$. The use of affine displacement boundary conditions in DNS likely poses a higher resistance to void growth in elastic loading and softening regimes as compared to the periodic boundary condition that can also be used to model the same macroscopic deformation.

Most of the simulations are carried out for macroscopic uniaxial deformation, e.g. $\mathbf{F} = \dot{\epsilon}t\mathbf{e}_1 \otimes \mathbf{e}_1 + \mathbf{I}$, or macroscopic triaxial deformation, i.e. $\mathbf{F} = (1 + \dot{\epsilon}t)\,\mathbf{I}$, with $\dot{\epsilon}$ denoting a constant engineering strain rate and $\mathbf{e}_1, \mathbf{e}_2, \mathbf{e}_3$ denoting 3 orthogonal unit vectors parallel to the edges of UC (the UC axes). Additional simulations are carried our for the case of macroscopic simple shear, e.g. $\mathbf{F} = \dot{F}_{12}t\mathbf{e}_1 \otimes \mathbf{e}_2 + \mathbf{I}$. Unless otherwise noted, the simulations are carried out with the lattice cubic axes aligned with the UC axes, e.g. $\mathbf{e}_1$ parallel with [100]. For simulations explicitly investigating orientation effects, Euler angles (denoted here as ϕ_1, ϕ_2, and Φ) are utilized to describe the orientation of the lattice cubic axes relative to the UC axes.

Since our interests here are in dynamic ductile failure, all simulations are carried out

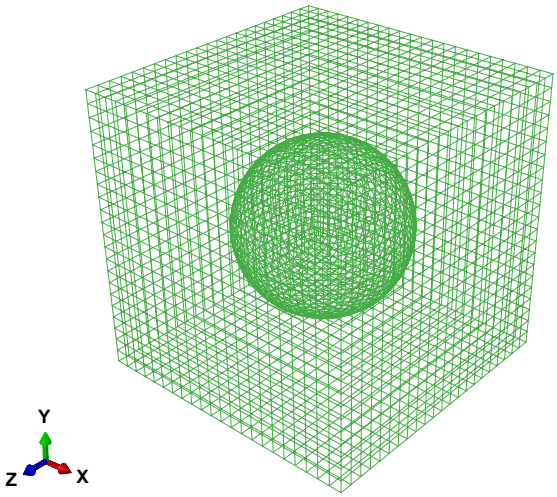

Fig. 3.1: A representative finite element mesh of the unit cell.

at high engineering strain rates, e.g. $\dot{\epsilon} = 10^5$ s^{-1}, $\dot{\epsilon} = 10^6$ s^{-1}, or $\dot{F}_{12} = 10^6$ s^{-1}. However, such high loading strain rates applied instantaneously to the external surfaces of an otherwise resting body will induce significant wave dynamics within the solid matrix. While the DNS naturally captures this phenomena, the CPD model is incapable of reproducing such fine details. In order to minimize this effect, an affine initial microscale velocity field is prescribed to all material points within the UC, i.e. $\mathbf{v}|_{t=0} = \dot{\mathbf{F}} \cdot \mathbf{x_0}$, in both DNS and CPD calculations. In the CPD this affine velocity field implies $\dot{a}_{t=0} = a_0 l_0^{-1} \dot{l}_{t=0}$, which in turn implies a nil initial condition on the rate of porosity, i.e. $\dot{\varphi}_{t=0} = 0$. Spatially homogeneous initial conditions are assumed for both the mobile and immobile dislocation densities. The initial temperature is specified as $\vartheta_{t=0} = 300$ K throughout the domain, and simulations are carried out under isothermal conditions to facilitate a simpler interpretation of the model results in the context of validation assessment.

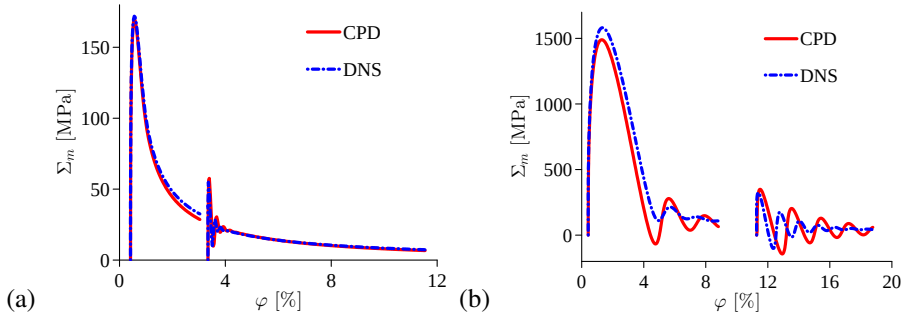

Fig. 3.2: Comparisons of mean macroscopic stress Σ_m as a function of evolving void volume fraction φ as predicted by DNS and our CPD theory. Macroscopic triaxial deformation, i.e. $\mathbf{F} = (1 + \dot{\epsilon}t)\,\mathbf{I}$, is applied at a constant engineering strain rate of a) $\dot{\epsilon} = 10^5$ s^{-1} and b) $\dot{\epsilon} = 10^6$ s^{-1} for varying values of initial porosity with a constant uniform mobile dislocation density of $\rho_m^{(\alpha)} = 10^{14}$ m^{-2}.

3.2 Constant dislocation density structure

In order to systematically assess the predictive quality of the CPD in relation to DNS, I begin with comparisons for a frozen dislocation density structure, i.e. $\dot{\varrho}_m^{(\alpha)} = \dot{\varrho}_{im}^{(\alpha)} = 0$, that is spatially homogeneous across the microscale domain. Such simulations enable us to remove any potential discrepancies between CPD and DNS that may arise due to the spatial distribution (or its effects) not be adequately captured in the CPD theory.

3.2.1 Isolating effects of micro-inertia and $\mathcal{R}_{dd}$ in the absence of $\mathcal{R}_{cr}$

In this subsection, I make an additional effort to isolate features by forcing the critical resolved shear stress on all slip systems to be zero, i.e. $\tau_{cr}^{(\alpha)} = 0$. The effect of this simplification on the CPD theory is that the quasi-static critical resistance is exactly equal to zero, i.e. $\mathcal{R}_{cr} = 0$. While the critical resolved shear stress is neglected, here I maintain the contribution of the over-shear stress, i.e. $\left|\tau^{(\alpha)}\right| - \tau_{cr}^{(\alpha)}$, associated with relativistic drag effects, cf. Eq. (2.2.4).

Comparisons of the evolution of macroscopic mean stress (Σ_m) as a function of evolv-

ing porosity φ are presented in Fig. 3.2 and Fig. 3.3. For these plots, simulation cases include different initial void volume fractions and constant uniform dislocation density on all slip systems, e.g. $\rho_m^{(\alpha)} = 10^{14}\ \mathrm{m}^{-2}$. Figure 3.2(a) and Fig. 3.2(b) compare the evolution of mean stress versus porosity for triaxial loading with constant engineering strain rates of $10^5\ \mathrm{s}^{-1}$ and $10^6\ \mathrm{s}^{-1}$, respectively, for various initial values of porosity. The CPD theory captures the overall effective softening response and viscous resistance quite well.

The results presented in Fig. 3.3 demonstrate the very strong dependence of the mechanical response of the UC on the dislocation density, and that this effect is captured quite well by the CPD theory. Comparisons of the evolution of macroscopic mean stress and equivalent Mises stress as predicted by DNS and the CPD theory are presented in Fig. 3.4 for uniaxial deformation, e.g. $\mathbf{F} = \dot{\epsilon} t \mathbf{e}_1 \otimes \mathbf{e}_1 + \mathbf{I}$ at an engineering strain rate of $10^6\ \mathrm{s}^{-1}$. Figure 3.4(a) provides additional evidence of the utility of our model for $\mathcal{R}_{dd}$ even for a non-spherically symmetric deformation. Moreover, the remarkable agreement between DNS and CPD in Fig. 3.4(b) provides some degree of confidence in Eq. (2.2.18), which governs the evolution of the macroscopic slip rates, i.e. $\Gamma_p^{(\alpha)}$, and macroscopic deviatoric

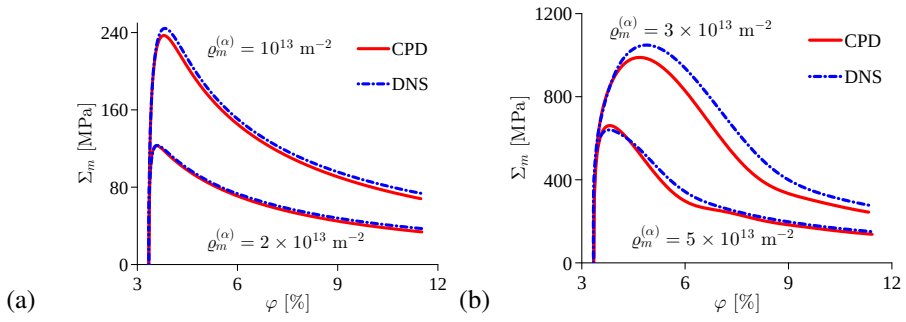

Fig. 3.3: Comparisons of mean macroscopic stress Σ_m as a function of evolving void volume fraction φ as predicted by DNS and our CPD theory. Macroscopic triaxial deformation, i.e. $\mathbf{F} = (1 + \dot{\epsilon} t)\, \mathbf{I}$, is applied at a constant engineering strain rate of a) $\dot{\epsilon} = 10^5\ \mathrm{s}^{-1}$ and b) $\dot{\epsilon} = 10^6\ \mathrm{s}^{-1}$ for the same initial porosity, but various constant mobile dislocation densities.

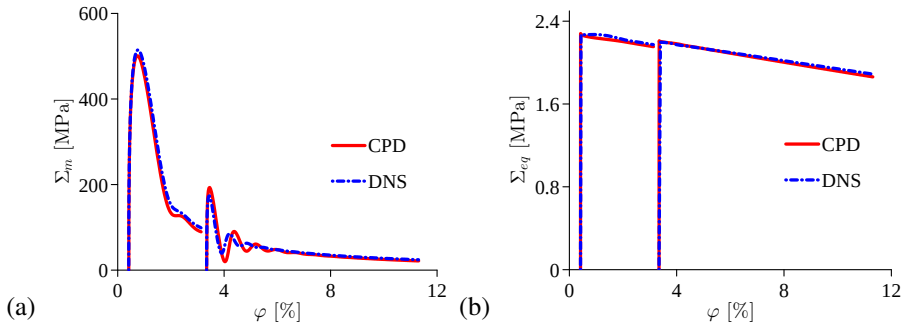

Fig. 3.4: Comparisons of a) mean macroscopic stress Σ_m and b) equivalent Mises macroscopic stress Σ_{eq} as a function of evolving void volume fraction φ as predicted by DNS and our CPD theory. Macroscopic uniaxial deformation, e.g. $\mathbf{F} = \dot{\epsilon} t \mathbf{e}_1 \otimes \mathbf{e}_1 + \mathbf{I}$, is applied at a constant engineering strain rate of $\dot{\epsilon} = 10^6$ s^{-1} for varying values of initial porosity with a constant uniform dislocation density of $\rho_m^{(\alpha)} = 10^{14}$ m^{-2}.

stress $\boldsymbol{\Sigma}'$ in our CPD theory.

In order to evaluate the theory under more complex loading cases, simulations of the UC loaded under uniaxial deformation, e.g. $\mathbf{F} = \dot{\epsilon} t \mathbf{e}_1 \otimes \mathbf{e}_1 + \mathbf{I}$, with an instantaneous transition (jump) in engineering strain rate from $\dot{\epsilon} = 10^5$ s^{-1} to 10^6 s^{-1} at an axial engineering strain of 1% (at $t = 0.1\mu$s) were conducted. For this case, the UC has an constant uniform dislocation density of $\rho_m^{(\alpha)} = 10^{14}$ m^{-2}. Figure 3.5(a) and Fig. 3.5(b) show that the evolution of mean and equivalent macroscopic stress as a function of evolving porosity from DNS is captured well by our CPD model.

3.2.2 Combined influence of micro-inertia, $\mathcal{R}_{dd}$, and $\mathcal{R}_{cr}$ without degradation of the macroscopic CRSS using a porosity dependent single crystal yield function

Having demonstrated some degree of confidence in the validity of our CPD theory in the absence of the quasi-static critical resistance term $\mathcal{R}_{cr}$, I now turn our attention to a validation assessment of $\mathcal{R}_{cr}$ by *turning on* the critical resolved shear stress (i.e. $\tau_{cr}^{(\alpha)} \neq 0$) in conjunction with inertia and $\mathcal{R}_{dd}$.

To assess $\mathcal{R}_{cr}$, DNS and CPD calculations were conducted for cases of constant uni-

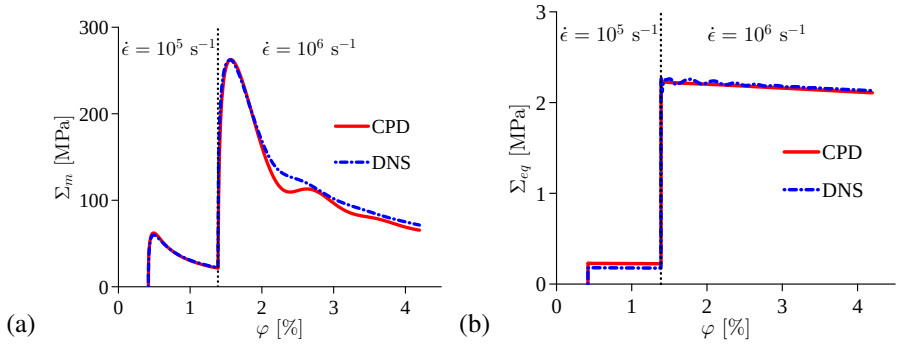

Fig. 3.5: Comparisons of a) mean macroscopic stress Σ_m and b) equivalent Mises macroscopic stress Σ_{eq} as predicted by DNS and our CPD theory. Macroscopic uniaxial deformation, e.g. $\mathbf{F} = \dot{\epsilon}t\mathbf{e}_1 \otimes \mathbf{e}_1 + \mathbf{I}$, is applied with an instantaneous transition (marked by the vertical dotted line) in engineering strain rate from $\dot{\epsilon} = 10^5$ s^{-1} to 10^6 s^{-1} at an axial engineering strain of 1% (at $t = 0.1$ μs). ($\rho_m^{(\alpha)} = 10^{14}$ m^{-2}).

form dislocation density of $\rho_m^{(\alpha)} = \rho_{im}^{(\alpha)} = 10^{14}$ m^{-2} with the UC loaded under macroscopic triaxial deformation, $\mathbf{F} = (1 + \dot{\epsilon}t)\,\mathbf{I}$, at engineering strain rates of $\dot{\epsilon} = 10^5$ s^{-1} and $\dot{\epsilon} = 10^6$ s^{-1}. Comparisons of DNS and CPD for this case are shown in Fig. 3.6 for two initial porosities (namely $\varphi_0 = 3.35\%$ and $\varphi_0 = 11.3\%$). The agreement between DNS and

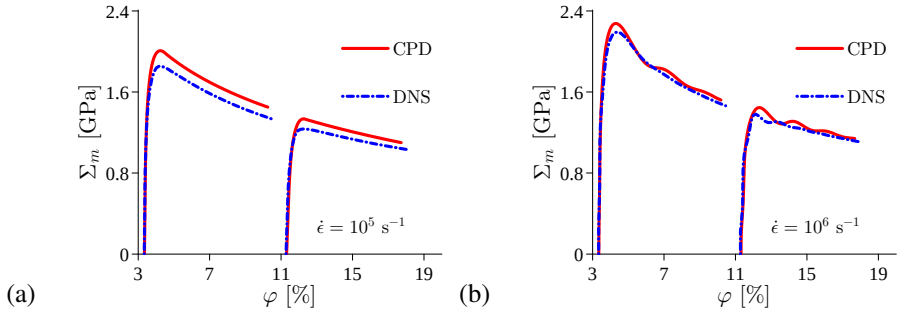

Fig. 3.6: Comparisons of mean macroscopic stress Σ_m as a function of evolving void volume fraction φ as predicted by DNS and our CPD theory with $\tau_{cr}^{(\alpha)} \neq 0$. Macroscopic triaxial deformation, i.e. $\mathbf{F} = (1 + \dot{\epsilon}t)\,\mathbf{I}$, is applied at a constant engineering strain rate of a) $\dot{\epsilon} = 10^5$ s^{-1} and b) $\dot{\epsilon} = 10^6$ s^{-1} for two values of initial porosity with a constant uniform dislocation density of $\rho_m^{(\alpha)} = \rho_{im}^{(\alpha)} = 10^{14}$ m^{-2}.

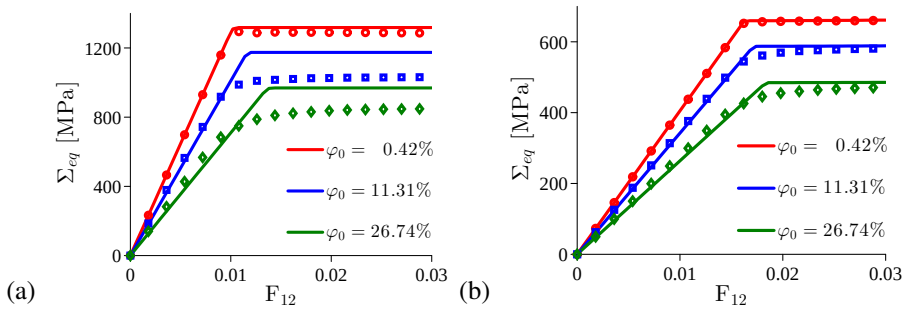

Fig. 3.7: Comparisons of equivalent macroscopic stress Σ_{eq} as a function of evolving macroscopic shear deformation F_{12} as predicted by DNS (markers) and our CPD theory (solid lines) with $\tau_{cr}^{(\alpha)} \neq 0$. Macroscopic shear deformation, i.e. $\mathbf{F} = F_{12}t\mathbf{e}_1 \otimes \mathbf{e}_2 + \mathbf{I}$, is applied at a constant engineering strain rate of $\dot{\mathrm{F}}_{12} = 10^6$ s^{-1}. The lattice axes are aligned such that a) $[100]$ and $[010]$ and b) $[110]$ and $[\bar{1}10]$ directions are parallel to the respective UC axes $\mathbf{e}_1$ and $\mathbf{e}_2$. ($\rho_m^{(\alpha)} = \rho_{im}^{(\alpha)} = 10^{14}$ m^{-2}).

CPD theory is remarkable given the numerous assumptions and approximations invoked in section 2.3.

Moreover, it is encouraging to note that discrepancy between the CPD and DNS at the lower strain rate case shown in Fig. 3.6(a) is essentially a constant over-prediction of about 10% throughout the entire loading history. I can reasonably attribute nearly all of this error in the CPD prediction to an error in our model for $\mathcal{R}_{cr}$ by recognizing that the agreement between DNS and CPD is nearly perfect under the same loading conditions with $\mathcal{R}_{cr}$ *turned off* (cf. Fig. 3.2(a)). As such, one could seemingly reduce the error in our model for $\mathcal{R}_{cr}$ to perhaps no more than a few percent by amending Eq. (2.3.14) to include a pre-factor correction constant of about 0.9 (at least for these loading conditions).

In order to assess the capability of the CPD theory to capture crystallographic orientation effects predicted by DNS, a number of macroscopic simple shear deformation, i.e. $\mathbf{F} = \dot{F}_{12}t\mathbf{e}_1 \otimes \mathbf{e}_2 + \mathbf{I}$, simulations were carried out at a deformation rate of $\dot{F}_{12} = 10^6$ s^{-1}. For cases of loading under macroscopic simple shear, there are only negligible changes in

the void volume fraction. Consequently, for these cases I instead compare the evolution of macroscopic equivalent stress Σ_{eq} with the evolving macroscopic shear deformation F_{12} in Fig. 3.7 and Fig. 3.8. Comparisons of macroscopic stress-macroscopic deformation curves as predicted by DNS (markers) and CPD theory (solid lines) are shown in Fig. 3.7 from simple shear loading for various initial void volume fractions and two different crystallographic orientations. The agreement between CPD and DNS in the inelastic region depends strongly on the initial porosity and the crystallographic orientation. For the case where the cubic crystal axes are aligned with the unit cell axes, i.e. Fig. 3.7(a), the results indicate that our CPD model over-predicts the inelastic response in comparison to DNS. Whereas, for cases in which the shearing direction $\mathbf{e}_1$ is aligned with any of the $\langle 110 \rangle$ lattice directions, i.e. Fig. 3.7(b), the agreement is significantly better. Regardless of the crystallographic orientation, a trend is observed that the discrepancy between CPD and DNS is fairly negligible at low initial porosities, e.g. $\varphi_0 \lesssim 0.5\%$. Such an observation is somewhat encouraging, given that we are primarily interested in applying our CPD framework as a ductile failure theory for initially dense, i.e. $\varphi_0 \ll 0.5\%$, single crystals.

In order to further explore the accuracy of our model across a wider range of crystallographic orientations, I conducted an additional 364 DNS and CPD macroscopic simple shear simulations to sweep through crystallographic orientation space. Each of these simulations results in an equivalent macroscopic stress – macroscopic shear deformation curve similar to those shown in Fig. 3.7. From each of these 364 simulated stress-deformation curves I extract a single data point of the equivalent macroscopic stress at a shear deformation of $F_{12} = 0.03$[1] (i.e. $\Sigma_{eq}|_{F_{12}=0.03}$) predicted by DNS and CPD. The resulting 728 total data points obtained from DNS and CPD simulations are reported in Fig. 3.8 as a function of the Euler angles. Four sets of Euler angles are chosen, namely

[1]Note that this choice of shear deformation is well into the inelastic region for all orientations considered.

- $\phi_1 = 0°, \Phi = 30°,$ and $\phi_2 \in [0°, 90°]$ with a $1°$ interval;
- $\phi_1 = 0°, \Phi = 45°,$ and $\phi_2 \in [0°, 90°]$ with a $1°$ interval;
- $\phi_1 = 10°, \Phi = 25°,$ and $\phi_2 \in [0°, 90°]$ with a $1°$ interval;
- $\phi_1 = 50°, \Phi = 12°,$ and $\phi_2 \in [0°, 90°]$ with a $1°$ interval,

for which I note that this choice of ϕ_2 completely spans the symmetry of face-centered cubic materials. For these simulations, each UC was assigned a constant uniform dislocation density of $\rho_m^{(\alpha)} = \rho_{im}^{(\alpha)} = 10^{14}\ \mathrm{m}^{-2}$ and an initial void volume fraction of $\varphi_0 = 11.31\%$, which is a large enough porosity to produce fairly significant discrepancies between CPD and DNS for some crystallographic orientations (cf. Fig. 3.7).

Overall, our CPD theory captures the general trends of the crystallographic orientation dependence as predicted by DNS, but appears to over emphasize the orientation dependence of the effective yield stress. While our model exhibits relatively high accuracy for several orientations (cf. Fig. 3.8(a)), it results in up to 18% error in some others (Fig. 3.8(b)). This discrepancy suggests that the effect of voids on macroscopic shear strength is more complex than can be represented $T_{cr}^{(\alpha)} = \tau_{cr}^{(\alpha)}$.

3.2.3 Combined influence of micro-inertia, $\mathcal{R}_{dd}$, and $\mathcal{R}_{cr}$ with degradation of the macroscopic CRSS using a porosity dependent single crystal yield function

In this subsection, we repeated the crystal plasticity-damage finite element (CPD-FE) and DNS calculations of simple shear deformation presented in the last subsection using the theory for degradation of the macroscopic CRSS using a porosity dependent single crystal yield function. We identify the parameters in Eq. (2.2.23) to be $q_1 = 1.20, q_2 = 1.25$ and $\chi = 3$ upon comparing the macroscopic shear response from the CPD-FE and DNS. The results of CPD-FE using the theory for degradation of the macroscopic CRSS (red curve) are compared with previous subsection result (green curve) and the DNS results (blue markers) in Fig. 3.9 across a range of crystal orientations. As can be seen in Fig. 3.9,

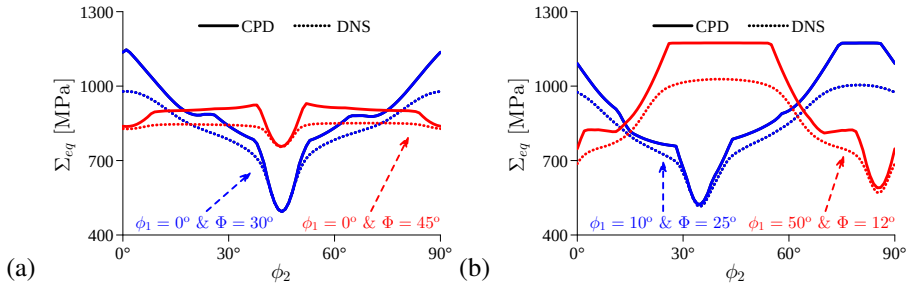

Fig. 3.8: Results of a high-throughput analysis comparing equivalent macroscopic stress at a simple shear deformation $F_{12} = 0.03$ (i.e. $\Sigma_{eq}|_{F_{12}=0.03}$) as a function of various crystallographic orientations as predicted by DNS (dotted line) and our CPD theory (solid lines) with $\tau_{cr}^{(\alpha)} \neq 0$. Macroscopic simple shear deformation, i.e. $\mathbf{F} = \dot{F}_{12} t \mathbf{e}_1 \otimes \mathbf{e}_2 + \mathbf{I}$, is applied at a constant engineering strain rate of $\dot{\mathrm{F}}_{12} = 10^6$ s^{-1}. For each choice of ϕ_1 and Φ, $\phi_2 \in [0°, 90°]$ with 1° intervals. ($\varphi_0 = 11.31\%$ and $\rho_m^{(\alpha)} = \rho_{im}^{(\alpha)} = 10^{14}$ m^{-2}).

the extension based on Eq. (2.2.23) substantially improves the agreement between the homogenized crystal plasticity damage theory with the DNS results.

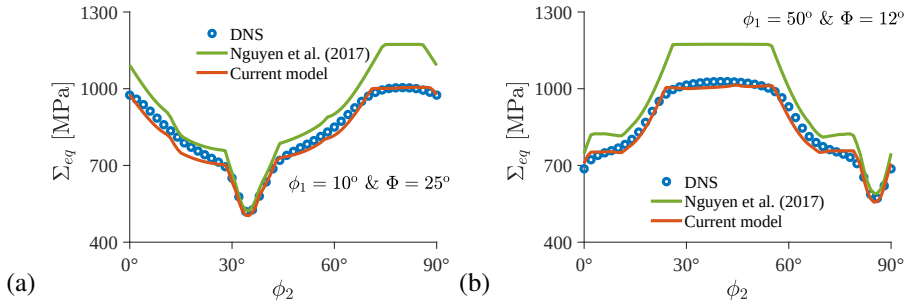

Fig. 3.9: Results of a high-throughput analysis comparing equivalent macroscopic stress at a simple shear deformation $F_{12} = 0.03$ (i.e. $\Sigma_{eq}|_{F_{12}=0.03}$) as a function of various crystallographic orientations as predicted by DNS (markers), Nguyen et al. (2017) model (solid green lines) and the current CPD model (solid red lines) with $\tau_{cr}^{(\alpha)} \neq 0$. Macroscopic simple shear deformation, i.e. $\mathbf{F} = \dot{F}_{12} t \mathbf{e}_1 \otimes \mathbf{e}_2 + \mathbf{I}$, is applied at a constant engineering strain rate of $\dot{\mathrm{F}}_{12} = 10^6$ s^{-1}. For each choice of ϕ_1 and Φ, $\phi_2 \in [0°, 90°]$ with 1° intervals. ($\varphi_0 = 11.31\%$ and $\rho_m^{(\alpha)} = \rho_{im}^{(\alpha)} = 10^{14}$ m^{-2}). Nguyen et al. (2017) model simplified the effect of void on shear strength, i.e. $T_{cr}^{(\alpha)} = \tau_{cr}^{(\alpha)}$. The current CPD model account for the effect of void on shear strength using Eq. (2.2.23).

DNS of cases of simple shear deformation were used to *calibrate* Eq. (2.2.23) within the extended CPD-FE approach; CPD-FE simulations of uniaxial strain loading conditions were conducted and compared with DNS to build further confidence of the extended model in cases where the shear and hydrostatic stresses are of the same order of magnitude. Three crystallographic loading directions, i.e. $\langle 100 \rangle$, $\langle 110 \rangle$, $\langle 111 \rangle$ were included in these calculations. The computed evolution of macroscopic equivalent stress with respect to axial engineering strain is compared with the DNS results in Fig. 3.10(a) and Fig. 3.10(b) for the model without or with the theory for degradation of the macroscopic CRSS, respectively. The improved agreement between CPD-FE and DNS in both the peak effective deviatoric stress and the subsequent softening using the present extension to our previous model is apparent from these figures. In the results obtained without degraded macroscopic CRSS (Eq. (2.2.23)), i.e. Fig. 3.10(a), the effective deviatoric stress after yielding gradually softens as a result of increasing porosity, with the degradation equal to ratio of $(1 - \varphi)$. In the results from the current model, i.e. Fig. 3.10(b), the effective deviatoric stress softens more rapidly upon yielding because of the contribution of the hydrostatic stress, Σ_m, significantly increasing the $\cosh$ term in Eq. (2.2.23) leading to a pronounced reduction in the effective shear resistance. While the new model exhibits a more rapid degradation in effective deviatoric stress than the DNS, the value approaches that of the DNS as the strain is further increased (i.e. to 6%) leading to generally better agreement than the previous model. On the other hand, these extensions have not reduced the accuracy of the computed evolution of the mean stress (cf. Fig. 3.10(c)) under these conditions of uniaxial strain. We note that the evolution of mean stress for the three crystallographic loading directions are strongly similar for DNS results and identical for the CPD-FE results under these cases where hardening was excluded by holding dislocation density constant. These results, in particular from the DNS, suggest that much of the observed orientation dependence of spall strength (Turley et al., 2018) may result from the

anisotropic (static and dynamic) hardening due to dislocation evolution during the initial shock compression of the material, especially in consideration of the identical initial slip resistance assumed for all crystal slip systems.

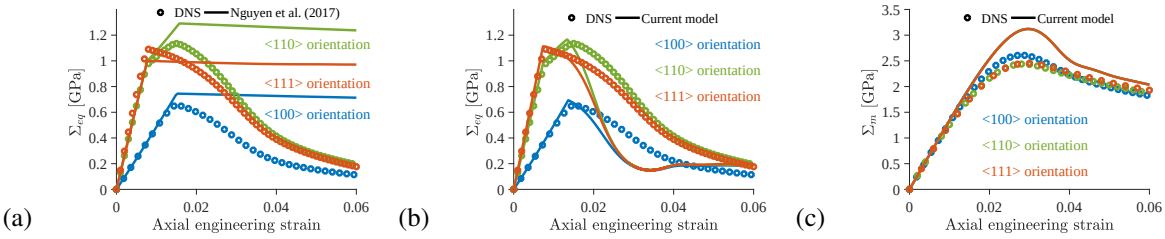

Fig. 3.10: Comparisons of (a,b) equivalent macroscopic stress Σ_{eq}, (c) mean macroscopic stress Σ_m and as a function of axial engineering strain as predicted by DNS, CPD without degraded macroscopic CRSS (a), and CPD with degraded macroscopic CRSS (Eq. (2.2.23)) (b and c). Macroscopic uniaxial deformation, i.e. $\mathbf{F} = \dot{\epsilon} t \mathbf{e}_1 \otimes \mathbf{e}_1 + \mathbf{I}$, is applied at a constant engineering strain rate of $\dot{\epsilon} = 10^6$ s^{-1} with a *constant uniform dislocation density* of $\varrho_m^{(\alpha)} = \varrho_{im}^{(\alpha)} = 10^{14}$ m^{-2} ($\varphi_0 = 0.42\%$).

3.3 Implications of an evolving dislocation substructure

In the present subsection, attention is turned to cases where dislocation density evolves with inelastic deformation according to dislocation interaction and evolution mechanisms by using values of model parameters (c_{trap}, c_{mult}, c_{ann}^{m}, c_{ann}^{im}) as listed in Table 2.1. Again for these calculations, as with those discussed in subsection 3.2.1, the threshold stress for dislocation glide is first held to zero, i.e. $\tau_{cr}^{(\alpha)} = 0$, in an effort to isolate the role of viscous resistance $\mathcal{R}_{dd}$.

3.3.1 Isolating effects of micro-inertia and $\mathcal{R}_{dd}$ in the absence of $\mathcal{R}_{cr}$

Within one set of comparative calculations shown in Fig. 3.11, the chosen UC was constructed with an initially spatially homogeneous and initially uniform (on all slip sys-

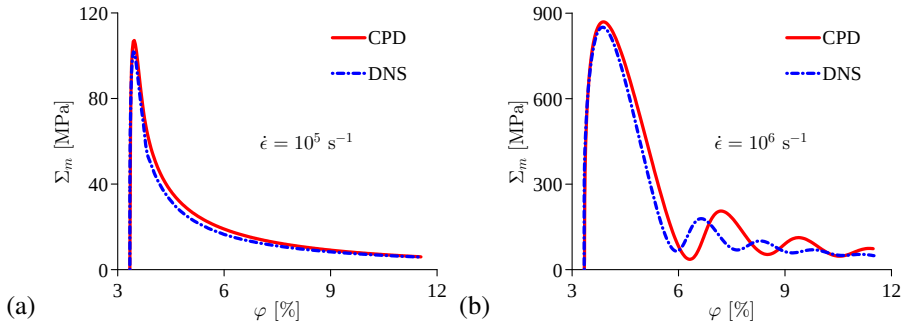

Fig. 3.11: Comparisons of mean macroscopic stress Σ_m as a function of evolving void volume fraction φ (and dislocation density) as predicted by DNS and our CPD theory. Macroscopic triaxial deformation, i.e. $\mathbf{F} = (1 + \dot{\epsilon}t)\,\mathbf{I}$, is applied at a constant engineering strain rate of a) $\dot{\epsilon} = 10^5$ s^{-1} and b) $\dot{\epsilon} = 10^6$ s^{-1} with an initially uniform dislocation density of $\varrho^{(\alpha)}_{m,0} = \varrho^{(\alpha)}_{im,0} = 2 \times 10^{13}$ m^{-2} (for $\varphi_0 = 3.34\%$).

tems) dislocation density of $\varrho^{(\alpha)}_{m,0} = \varrho^{(\alpha)}_{im,0} = 2 \times 10^{13}$ m^{-2} with an initial void volume fraction of $\varphi_0 = 3.34\%$. These UCs were loaded under macroscopic triaxial deformation, i.e. $\mathbf{F} = (1 + \dot{\epsilon}t)\,\mathbf{I}$, at a constant engineering strain rate of $\dot{\epsilon} = 10^5$ s^{-1} and $\dot{\epsilon} = 10^6$ s^{-1}. Again, the agreement between CPD and DNS is remarkable. This rather complex mecha-

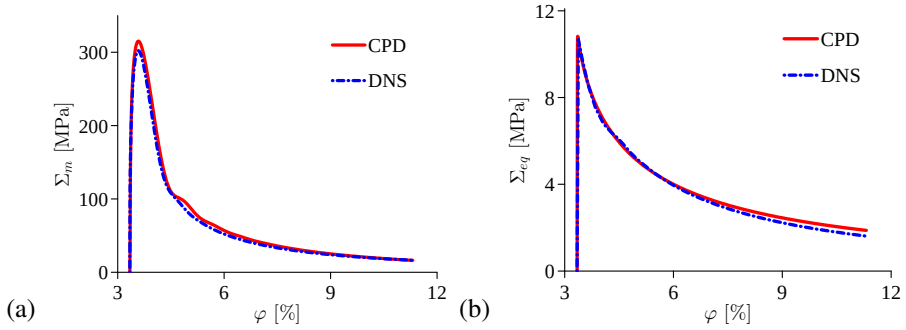

Fig. 3.12: Comparisons of a) mean macroscopic stress Σ_m and b) equivalent Mises macroscopic stress Σ_{eq} as a function of evolving void volume fraction φ as predicted by DNS and our CPD theory. Macroscopic uniaxial deformation, i.e. $\mathbf{F} = \dot{\epsilon}t\mathbf{e}_1 \otimes \mathbf{e}_1 + \mathbf{I}$, is applied at a constant engineering strain rate of $\dot{\epsilon} = 10^6$ s^{-1} with an initially uniform dislocation density of $\varrho^{(\alpha)}_{m,0} = \varrho^{(\alpha)}_{im,0} = 2 \times 10^{13}$ m^{-2} (for $\varphi_0 = 3.34\%$).

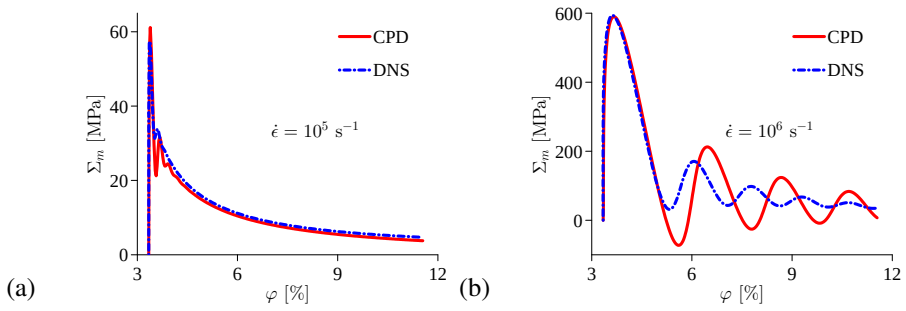

Fig. 3.13: Comparisons of mean macroscopic stress Σ_m as a function of evolving void volume fraction φ (and dislocation density) as predicted by DNS and our CPD theory. Macroscopic triaxial deformation, i.e. $\mathbf{F} = (1 + \dot{\epsilon}t)\,\mathbf{I}$, is applied at a constant engineering strain rate of a) $\dot{\epsilon} = 10^5$ s^{-1} and b) $\dot{\epsilon} = 10^6$ s^{-1} with a uniform initial immobile dislocation density of $\varrho^{(\alpha)}_{im,0} = 10^{13}$ m^{-2}, and a non-uniform initial mobile dislocation density of $\varrho^{(\alpha)}_{m,0} = \alpha \times 10^{13}$ m^{-2} (for $\varphi_0 = 3.34\%$).

nism of evolving dislocation density is captured remarkably well in our CPD theory by a fairly simple set of equations governing substructure evolution, and an approximation for the spatial distribution of the substructure across the microscale domain.

Respective comparisons of the evolution of macroscopic mean stress and equivalent Mises stress ($\Sigma_{eq} \triangleq \sqrt{\frac{3}{2}\boldsymbol{\Sigma}' : \boldsymbol{\Sigma}'}$) as predicted by DNS and the CPD theory are presented in Fig. 3.12(a) and Fig. 3.12(b) for uniaxial deformation, e.g. $\mathbf{F} = \dot{\epsilon}t\mathbf{e}_1 \otimes \mathbf{e}_1 + \mathbf{I}$ at an engineering strain rate of 10^6 s^{-1}. Moreover, the remarkable agreement between DNS and CPD in Fig. 3.4(b) provides some degree of confidence in Eq. (2.2.18) and Eq. (2.2.20), which govern the evolution of the macroscopic slip rates $\Gamma^{(\alpha)}_p$ and macroscopic deviatoric stress $\boldsymbol{\Sigma}'$ in our CPD theory.

In order to assess accuracy of the CPD model under a broader range of conditions, a set of UC calculations starting with an initially non-uniform distribution of mobile dislocation density across various slip-systems, i.e. $\varrho^{(\alpha)}_m \neq \varrho^{(\beta)}_m$ for $\alpha \neq \beta$, is compared in Fig. 3.13. More specifically, initial mobile dislocation densities on each slip system

were assigned according to $\varrho_{m,0}^{(\alpha)} = \alpha \times 10^{13}\,\mathrm{m}^{-2}$ following the slip system convention detailed in Table 2.2. The initial immobile dislocation density was specified uniformly as $\varrho_{im,0}^{(\alpha)} = 10^{13}\,\mathrm{m}^{-2}$. Otherwise, the geometry and loading conditions are identical to those utilized in Fig. 3.11. As evidenced by the results depicted in Fig. 3.13, this approach renders a CPD theory that is in reasonably good agreement with DNS even for such a disparate set of initial conditions.

3.3.2 Combined influence of micro-inertia, $\mathcal{R}_{dd}$, and $\mathcal{R}_{cr}$

Due to our particular choice of non-local microscale hardening law, i.e. Eq. (2.2.7), the critical resolved shear stress $\tau_{cr}^{(\alpha)}$ is obliged to be spatially homogeneous across the microscale domain (at a particular macroscopic point). As such, the relatively small deficiencies (cf. Fig. 3.6) in our CPD model for the quasi-static critical resistance $\mathcal{R}_{cr}$, i.e. Eq. (2.3.14), are essentially the same regardless of whether dislocation density is frozen or evolving. Given this argument, there is no particular need to carry out additional DNS of UCs with evolving dislocation density for $\tau_{cr}^{(\alpha)} \neq 0$.

4. CALIBRATION OF THE FRAMEWORK AGAINST SINGLE CRYSTAL EXPERIMENTS

4.1 A straightforward procedure for model calibration

In this section, we calibrate our model parameters by direct comparison with published experimental data. A typical calibration procedure for dynamic ductile failure models is through comparing the free surface velocity history from a plate impact test and its simulation counterpart. Using this approach, the crystal plasticity parameters can be calibrated from the shock front profile or the first part of the velocity history, i.e. when the velocity rises from zero to maximum value or shock wave reaches the target plate free surface (e.g. Austin and McDowell, 2011, 2012; Lloyd et al., 2014b). The damage model parameters could then be calibrated from the pullback velocity, i.e. the difference between the maximum velocity and the pullback signal. In addition to plate impact tests, crystal plasticity parameters can also be calibrated from comparing the stress-strain responses measured from Split-Hopkinson pressure bar (SHPB $-$ also known as Kolsky bar) experimental data and extracted from the simulation counterpart. The calibration procedure using plate impact test accesses more analagous strain rates ($> 10^4$ s^{-1}) and stress state from impact events, but involves fairly small strains ($< 10\%$). In contrast, the calibration procedure using SHPB can access larger strains (from 10% to 50%), but at lower strain rates ($\sim 10^3$ s^{-1}) and stresses. As such, we recommend the crystal plasticity models that will be utilized for physics-based spall predictions to be calibrated against both velocity history as well as a method to evaluate the large strain response (e.g. SHPB, or Taylor anvil experiments). On the other hand, calibration against plate impact test can be a cumbersome process due to the restrictions of i) small time increment for numerical stability,

ii) small element size to properly model shock wave propagation inside flyer and target plates. Therefore, for the time being we calibrate our crystal plasticity model parameters against SHPB using an eight-node volume element loaded under nominally uniaxial stress conditions for computational efficiency. The damage distribution parameters would then be calibrated using also an eight-node volume element subjected to compression/tension cyclic loading as to be explained in the following.

4.1.1 Plasticity calibration

In this subsection, we calibrate the dislocation evolution parameters using solid (i.e. $\varphi = 0$) single crystal copper SHPB experiments performed by Rittel et al. (2012). Due to the relatively low strain rate to observe the effect of heterogenous dislocation nucleation, the nucleation parameters was taken or adjusted from (Austin and McDowell, 2012) rather than being calibrated here. With that being said, this subsection calibrate $c_{mult}, c_{trap}, c_{ann}^{m}$ and c_{ann}^{im}.

Uniaxial stress compression is the typical representation of loading with Split-Hopkinson pressure bar experiment. In order to simulate uniaxial stress compression in a single three-dimensional element of Abaqus C3D8R type, the loading direction face on the left (i.e. $X = -$) was held fixed, the loading direction face on the right (i.e. $X = +$) was given a prescribed velocity. The remaining faces (i.e. $Y = \pm, Z = \pm$) are unconstrained. The $\langle 123 \rangle$ crystal orientation is aligned with the loading direction (**X**). The volume element was subjected to the target true strain rates from 3000 s^{-1} to 5800 s^{-1}. The true stress versus true strain from experiment results and their simulation counterparts are presented in Fig. 4.1. By adjusting the dislocation evolution parameters ($c_{mult}, c_{trap}, c_{ann}^{m}$ and c_{ann}^{im}), the simulation result is brought into a reasonably good agreement with experimental data, especially for true strain rates of 4150 s^{-1} and up. The calibrated value of parameters $c_{mult}, c_{trap}, c_{ann}^{m}$ and c_{ann}^{im} are presented in Table 4.1. As can be seen in Fig. 4.1, the present

crystal plasticity model provides a good fitting for single crystal data up to strains of 0.3-0.4, at which point the model deviates from the experiment data. This result implies that dislocation density does not come to the equilibrium value as it should in the experiment. The agreement between our simulation results and experiment data up to the large strain of 0.3 provides confidence for our spallation modeling later on, in which the spall strength occurs at fairly low strains (Wright and Ramesh, 2008).

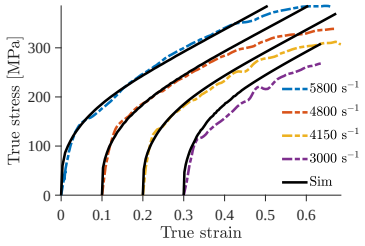

Fig. 4.1: Comparison of true stress - true strain behavior from Split Hopkinson pressure bar experiments (dashed line) and simulations (black solid lines) for loading orientation $\langle 123 \rangle$ (Rittel et al., 2012) and different loading rates.

4.1.2 Damage distribution calibration

In this subsection, we calibrate our damage parameters, i.e. φ_0 and ℓ_v, using acoustic limit of spall strength (i.e. Eq. (1.1.10)) estimated from plate impact tests (Turley et al., 2018).

As mentioned in chapter 1, the deformation on spall plane is usually idealized to be uniaxial strain due to high aspect ratio between plates' radius and thickness (e.g. Grady, 1988). Under the uniaxial strain condition, the total strain is restricted to be uniaxial rather than its elastic/inelastic components, which enables general 3D dislocation slip. The uniaxial strain deformation can be described with the deformation gradient $\mathbf{F} = (F_{11} -$

Table 4.1: Material parameters for single crystal copper subjected to high rate ductile damage process used in this chapter. Other model paramters were given in the previous tables.

Parameters	Value	Unit	Reference
Initial material state			
ϱ_{m0}	10^{-3}	$\mu\mathrm{m}^{-2}$	
ϱ_{im0}	10^{-2}	$\mu\mathrm{m}^{-2}$	
Strength parameters			
b	2.56	Å	
τ_0	10	MPa	
$c_\perp$	0.5	–	
μ	$41 \cdot 10^3$	MPa	
Dislocation density evolution parameters			
c_{mult}	$7.68 \cdot 10^{-5}$	–	Calibrated
c_{trap}	$5 \cdot 10^{-3}$	–	Calibrated
c_{ann}^{m}	1	–	Calibrated
c_{ann}^{im}	1	–	Calibrated
α_{het}	$1.4 \cdot 10^3$	$\mu\mathrm{m}^{-2}$	(Austin and McDowell, 2012)
τ_{min}	16	MPa	(Austin and McDowell, 2012)
τ_{max}	$\frac{\mu}{15}$	–	(Austin and McDowell, 2012)
m_{het}	0.7	–	(Austin and McDowell, 2012)
Damage distribution parameter			
ℓ_v	10	μm	Calibrated
φ_0	$5 \cdot 10^{-3}$	–	Calibrated
Equation of state			(Meyers, 1994)
ρ_0	8940	Kg/m^3	
C_0	3930	m/s	
s	1.49	–	
Γ	2.0	–	
Elastic modulus			(Every and McCurdy, 1992)
C_{11}	169	GPa	
C_{12}	122	GPa	
C_{44}	75.3	GPa	

$1)\mathbf{e}_1 \otimes \mathbf{e}_1 + \mathbf{I}$. Due to uniaxial strain loading condition, the relative volume is equal to the axial stretch, i.e. $J \equiv \det \mathbf{F} = F_{11}$. By controlling the rate of change of F_{11}, a

Table 4.2: Comparison of predicted spall strength from the model, and the spall strength measured from experiments (Turley et al., 2018).

Shot	Crys. Ori.	Impact vel. (ms^{-1})	u_{fs}^{max} (ms^{-1})	P (GPa)	$\dot{\varepsilon}$ (μs^{-1})	Δu_{pb} (ms^{-1})	$\Sigma_{sp}^{(Exp.)}$ (GPa)	$\Sigma_{sp}^{(Sim.)}$ (GPa)	$\Delta\Sigma_{sp}$ %
8	$\langle 100 \rangle$	280	279	5.19	0.7	96	1.69	1.68	0.48
11	$\langle 100 \rangle$	284	286	5.26	2.2	157	2.76	2.68	2.91
3	$\langle 100 \rangle$	297	297	5.52	1.3	121	2.13	2.08	2.28
4	$\langle 100 \rangle$	460	456	8.8	0.95	110	1.94	1.95	0.46
5	$\langle 100 \rangle$	598	598	11.7	0.75	120	2.11	1.88	12.30
6	$\langle 100 \rangle$	705	701	14.1	0.62	118	2.08	1.84	13.05
7	$\langle 100 \rangle$	296	294	5.5	0.65	95	1.67	1.65	1.11
9	$\langle 100 \rangle$	600	595	11.8	1.5	147	2.59	2.34	10.67
10	$\langle 100 \rangle$	500	498	9.63	1.4	124	2.18	2.25	3.07
1	$\langle 110 \rangle$	500	496	9.63	1.19	108	1.9	2.25	15.58
2	$\langle 111 \rangle$	502	494	9.67	0.8	85	1.5	1.86	19.36

compression/tension cycle can be obtained as below,

$$F_{11} = \begin{cases} 1 - \dot{\varepsilon}t & \text{for} \quad \mathrm{t} < \mathrm{t_{comp}} \\ 1 - \dot{\varepsilon}t_{comp} + \dot{\varepsilon}(t - t_{comp}) & \text{for} \quad \mathrm{t} \geq \mathrm{t_{comp}} \end{cases} \tag{4.1.1}$$

In the above equation, t_{comp} denotes compression loading time; $\dot{\varepsilon}$ denotes engineering strain rate ($\dot{\varepsilon} > 0$). By changing the value of compression time duration, i.e. t_{comp}, different relative volume J or compression pressure was obtained. The value of compression time duration t_{comp} was set so as to obtain the compression pressure in (Turley et al., 2018) for comparison purposes. Here, the strain rates during compression and tension are taken to be the same value. In reality, the compression rate is typically higher than the tension rate, due to the attenuation of the shock wave during propagation (Meyers, 1994).

Three crystallographic orientations $\langle 100 \rangle$, $\langle 110 \rangle$ and $\langle 111 \rangle$ are used as loading direc-

tions in these simulations, for a direct comparison with experiment data in Turley et al. (2018). The strain rate $\dot{\varepsilon}$ was taken as the associated experimental counterpart from the published hydrodynamic computer simulations (Turley et al., 2018) for $\langle 100 \rangle$ orientation. The strain rates from hydrodynamic computer simulations excludes $\langle 110 \rangle$ and $\langle 111 \rangle$ crystal orientations in Turley et al. (2018). Therefore, we use strain rates of 6 times the corresponding rates estimated from the unloading part of the velocity history, as calculated by Turley et al. (2018) for $\langle 100 \rangle$ orientation. The peak hydrostatic stress from our one element simulations is then compared to the acoustic spall strength from the experiment (Turley et al., 2018).

The damage parameters φ_0 and ℓ_v are then calibrated from shots 8 and 11, which are in close loading pressures (5.225 ± 0.035 GPa) but on two magnitude of strain rates (0.7 and 2.2 μs^{-1}), so that there is a reasonably good agreement between simulation and experiment spall strength, as showed in the first two rows of Table 4.2. The values of φ_0 and ℓ_v are given in Table 4.1. The calibrated parameters are then used to simulate the rest of plate impact tests in (Turley et al., 2018). The simulation results and experimental counterparts are presented in Table 4.2. The last column in Table 4.2 shows the relative errors between the simulated spall strength and the measured (acoustic) spall strength, i.e. $\frac{|\Sigma_{sp}^{(exp.)} - \Sigma_{sp}^{(sim.)}|}{\Sigma_{sp}^{(exp.)}}$. The magnitude difference in relative errors between 3 loading orientations of similar shock pressure (shots 10, 1, 2) implies that our parameters calibrated for $\langle 100 \rangle$ orientation are not optimal for other loading directions, i.e. $\langle 110 \rangle$ and $\langle 111 \rangle$.

In addition, our simulation spall strength agrees with the experimental data that the spall strength does not scale with Taylor factor. In particular, spall strength of $\langle 100 \rangle$ (2.45 Taylor factor), is higher than spall strength of $\langle 111 \rangle$ (3.67 Taylor factor), given the similar compression pressures (~ 10 GPa). The Taylor factor is a measure of the yield strength of a particular orientation. The fundamental reason for this nontrivial orientation dependence of spall strength is the objective of a future work.

4.2 Prediction of the pressure dependence of single crystal spall strength

Shock pressure can either harden and/or soften single crystal spall strength through inducing plastic deformation and the associated thermal energy. In particular, the temperature rise due to shock wave propagation (e.g. McQueen and Marsh, 1960) and plastic dissipation assists dislocations in overcoming short-range obstacles (Austin and McDowell, 2011). This thermal activation promotes void growth through plastic deformation of surrounding solid matrix, and therefore alleviates the material spall strength. Thermal softening seems to be the dominant factor for reducing spall strength with increasing pressure in the MD calculation of Luo et al. (2009a).

In this work, temperature evolution is omitted. Therefore, the sources for pressure dependence of spall strength are only i) typical strain hardening (i.e. due to the (total/net) dislocation density accumulation with increasing total applied strain), ii) dynamic softening (i.e. due to the mobile dislocation density accumulation). In particular, the over stress on each slip system (at microscale) ($|\tau^{(\alpha)}| - \tau_{cr}^{(\alpha)}$) on the drag regime is approximately proportion to dislocation velocity ($v_{\perp}^{(\alpha)}$) (e.g. Austin and McDowell, 2011, equation (10)), i.e. $|\tau^{(\alpha)}| - \tau_{cr}^{(\alpha)} \approx B_0 v_{\perp}^{(\alpha)}/b$, with B_0 and b denoting the dislocation phonon drag viscosity and Burger's vector respectively. B_0 is a function of temperature (Luscher et al., 2017). Using Orowan's equation, dislocation velocity is inversely correlated to mobile dislocation density, i.e. $v_{\perp}^{(\alpha)} = \dot{\gamma}^{(\alpha)}/b\varrho_m^{(\alpha)}$, at a given strain rate ($\dot{\gamma}^{(\alpha)}$). Therefore the viscosity of the crystalline material ($\eta^{(\alpha)} = (|\tau^{(\alpha)}| - \tau_{cr}^{(\alpha)})/\dot{\gamma}^{(\alpha)}$) is inversely correlated to the mobile dislocation density, i.e. $\eta^{(\alpha)} = B_0/b^2\varrho_m^{(\alpha)}$. While the viscosity is proportion to the spall dynamic resistance (see Johnson, 1981, equation 30), increasing mobile dislocation density consequently softens the spall strength of the crystalline material.

In this subsection, we use our calibrated model to explore the pressure dependence of single crystal copper spall strength on a range of strain rates. The same uniaxial strain

BVP as described previously is used here. We choose to model $\langle 100 \rangle$ orientation as a representative orientation due to availability of data for the orientation in Turley et al. (2018), which we can compare with. Compression pressure values on the range of [4-15] GPa and strain rate values on the range of [0.05-3.5] μs^{-1} are considered here. The simulated spall strength is presented in Fig. 4.2(a) as a contour plot.

As can be seen in Fig. 4.2(a), our model can capture the reported pressure dependence and rate dependence of spall strength in (Turley et al., 2018). In particular, given similar compression pressure $\sim$ 5.5 GPa, increasing the loading rate leads to an increase in the simulated spall strength (shots 7, 8 and 3); given similar strain rate $\sim$ 1.4 μs^{-1}, increasing the compression pressure leads to an increase in the simulated spall strength (shots 3, 10, 9). On this lower range of strain rate (less than 2 μs^{-1}), the spall strength is dominated by the quasistatic resistance which is a function of the total dislocation density accumulated with increasing total applied strain (or applied pressure). As a result, the spall strength monotonically increase with increasing compression pressure at low strain rate. On the other hand, as strain rate increases, the effect of pressure on spall strength reduces. At strain rate $\sim$ 2 μs^{-1}, the effect of rate dependence dominates spall strength.

Based on the experiment data for $\langle 100 \rangle$ orientation for shock stress of less than 15 GPa, (Turley et al., 2018) proposed an empirical model of spall strength, which is linear dependent on the shock pressure (P) and the strain rate ($\dot{\varepsilon}$) as below

$$\Sigma_{sp} = \Sigma_0 + k_1 P + k_2 \dot{\varepsilon}. \tag{4.2.1}$$

In this equation, k_1 and k_2 are the linear correlation coefficients between spall strength and pressure, strain rate respectively. The variation of our simulated spall strength on pressure at different strain rate values is presented in Fig. 4.2(b). While for each strain rate value, there is a linear correlation between pressure and spall strength, their linear

correlation coefficient reduces with increasing strain rate. The linear correlation coefficient approximated from our simulation result, denoted as $\partial\Sigma_{sp}/\partial P$, is presented in Fig. 4.2(c). The error bars show the 95% confidence interval for the coefficient. The emperical model value, k_1, of Turley et al. (2018) and the linear correlation coefficient from MD data of Luo et al. (2009a) are also showed in Fig. 4.2(c) (blue and red lines, respectively) for comparison purpose. In addition, three pairs of Turley et al. (2018) experimental data were chosen for computing the coefficients (square markers in Fig. 4.2(c)), such that the pairs are in the similar strain rates (less than 0.1 μs^{-1} difference) and wide ranges of pressure (more than 4 GPa difference). From the left of Fig. 4.2(c), they are shots 6, 7; shots 8, 5; shots 3, 10. The three data points (squares) show the same trend of decreasing $\partial\Sigma_{sp}/\partial P$ with increasing strain rate as in our simulation results. The comparison implies that a constant value of k_1, as in the empirical model (Eq. (4.2.1)), is posed for a low approximation accuracy at high loading rate. In other words, the effect of pressure and strain rate on spall strength should be coupled.

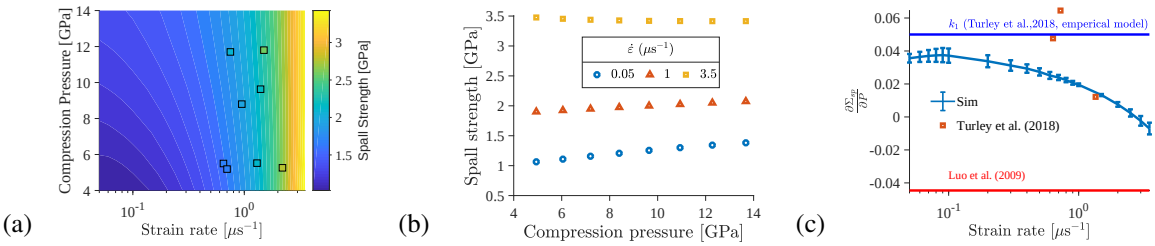

Fig. 4.2: a) Spall strength of $\langle 100 \rangle$ crystal loading orientation for a range of compression pressure and strain rate. Markers are acoustic limits from experiments of Turley et al. (2018). b) Variation of spall strength with pressure for strain rates 0.05, 1, 3.5 μs^{-1} (extracted from a)). c) Linear correlation coefficient betwen spall strength and pressure. Simulation results are presented as error bar. The bars correspond to 95% confidence interval in obtaining the correlation coefficients. The square markers are the correlation coefficients calculated from pairs of plate impact tests of Turley et al. (2018).

In the following, we will analyze the pressure dependence of spall strength. As the first step, we decompose the spall strength into the quasistatic ($\mathcal{R}_{cr}$), dynamic ($\mathcal{R}_{dd}$) and microinertia part ($\mathcal{R}_{iner}$) as described in chapter 2,

$$\Sigma_{sp} = \mathcal{R}_{cr} + \mathcal{R}_{dd} + \mathcal{R}_{iner}. \tag{4.2.2}$$

We then seek an approximation of the quasistatic spall strength, $\mathcal{R}_{cr}$, as a linear function of pressure using a simple isotropic rate-independent linear hardening and linear elasticity model. The volume element on spall plane, which is subjected to uniaxial compression/unloading, has an approximate equivalent strain of $\epsilon_{eq} = 4|\epsilon_v|/3$ (see Meyers, 1994, equation 14.1), with ϵ_v denoting the volumetric strain at peak compression pressure P. If a linear relationship between P and ϵ_v is assumed, i.e. $P = K_0|\epsilon_v|$, then the yield strength of the material after compression and unloading is

$$\Sigma_y = \sigma_{y0} + H\epsilon_{eq} = \sigma_{y0} + \frac{4H}{3K_0}P, \tag{4.2.3}$$

with σ_{y0} and H denote initial yield strength and the hardening modulus, respectively. The quasistatic spall strength is scaled with the yield strength of the material as $\mathcal{R}_{cr} = \frac{2}{3}\sigma_y \ln(\frac{1}{\varphi_0})$ (Huang et al., 1991). Therefore the quasistatic spall strength is linearly dependent on pressure, i.e.

$$\mathcal{R}_{cr} = \frac{2}{3}\sigma_{y0}\ln(\frac{1}{\varphi_0}) + \frac{8H}{9K_0}\ln(\frac{1}{\varphi_0})P. \tag{4.2.4}$$

If we approximate the copper hardening modulus H from Johnson-Cook model (Johnson and Cook, 1985, table 2) at constant temperature, $\epsilon_{eq} = 0.02$ and $\dot{\epsilon}_{eq} = 0$, then $H \approx 1.35$ GPa. By substituting the bulk modulus at rest, K_0, and our calibrated initial void volume fraction, $\varphi_0 = 0.005$, then we get $\frac{\partial \mathcal{R}_{cr}}{\partial P} = 0.046$. This value of $\frac{\partial \mathcal{R}_{cr}}{\partial P}$ is close to the k_1 value

of Turley et al. (2018) empirical model, and also to our value of $\frac{\partial \Sigma_{sp}}{\partial P}$ at low strain rate.

Following the phenomenological approach of Johnson and Cook (1985), the homologous temperature $\vartheta^* = \frac{\vartheta_{sp}-\vartheta_0}{\vartheta_m-\vartheta_0}$ can be added to account for the effect of temperature on the quasistatic strength. In here subscripts $_{sp}, _m$ and $_0$ denote spall, melting and initial condition. In addition, the homologous temperature scales down the quasistatic strength of copper in an almost linear fashion according to (Johnson and Cook, 1985, table 2). Therefore, the quasistatic strength for copper can be rewritten as

$$\mathcal{R}_{cr} = \left(\underbrace{\frac{2}{3}\sigma_0 \ln\left(\frac{1}{\varphi_0}\right)}_{\text{Incipient spall}} + \underbrace{\frac{8}{9}\frac{H}{K_0}\ln\left(\frac{1}{\varphi_0}\right)P}_{\text{Shock hardening}} \right) \underbrace{\left(1 - \frac{\vartheta_{sp}-\vartheta_0}{\vartheta_m-\vartheta_0}\right)}_{\text{Shock softening}} \tag{4.2.5}$$

The first two terms in Eq. (4.2.5) (i.e. incipient spall and shock hardening) are limited by the quasistatic spall strength of the fully saturated material, i.e. $\frac{2}{3}\sigma_\infty \ln\left(\frac{1}{\varphi_0}\right)$. The spall temperature (ϑ_{sp}) should be a physic-based function of initial temperature, shock pressure and plastic dissipation on the spall plane. For dislocation-free crystals in MD calculation of Luo et al. (2009a), the hardening can be ignored while the the initial yield strength σ_{y0} can be as high as 2.3 GPa (Schiøtz and Jacobsen, 2003). According to the published data (Luo et al., 2009a, table II) for $\langle 100 \rangle$ orientation, the dependence of homologous temperature on pressure can be approximated as $\frac{\partial \vartheta^*}{\partial P}$ =0.0051 GPa^{-1}. By substituting $\sigma_{y0} = 2.3$ GPa and $\frac{\partial \vartheta^*}{\partial P}$ =0.0051 GPa^{-1} into Eq. (4.2.5), the value of $\frac{\partial \Sigma_{sp}}{\partial P}$ becomes -0.0414, which is close to the our calculation of linear correlation coefficient from MD calculation data of Luo et al. (2009a) (cf. Fig. 4.2(c)). Therefore Eq. (4.2.5) provides a simple scalling law for quasistatic spall strength as a function of initial porosity, pressure and temperature, which is in agreement with both experimental data (Turley et al., 2018) and MD calculation (Luo et al., 2009a).

Toward the high range of strain rate, spall strength is also controlled by dynamic re-

sistance (through viscosity, η) and microinertia. At a given strain rate, the microinertia is independent of pressure, but the dynamics resistance ($\mathcal{R}_{dd}$) is sensitive compression pressure (Nguyen et al., 2017) through the generation of mobile dislocation density as mentioned above. That is, $\mathcal{R}_{dd}$ is proportional to viscosity (Johnson, 1981), which decreases nonlinearly with increasing pressure, i.e. $\partial\eta/\partial P < 0$. The viscosity effect on dynamic void growth was derived by Cortés (1992a) for isotropic material to be

$$\mathcal{R}_{dd} = \frac{4}{9}\eta\sigma_{y0}\frac{1-\varphi_0}{\varphi_0}\dot{\varepsilon}. \tag{4.2.6}$$

Therefore, the empirical parameter k_2 in Eq. (4.2.1) is better be a function of pressure P, i.e. $k_2 = \frac{4}{9}\eta\sigma_{y0}\frac{1-\varphi_0}{\varphi_0}$ and $\partial k_2/\partial P < 0$.

It should be noted that, the pressure dependence studied in here is for pressure of less than 15 GPa, i.e. before homogeneous dislocation nucleation is activated. Homogeneous dislocation nucleation process would lead to a dramatic change in dislocation density (Austin and McDowell, 2012, figure 9b), and potentially increases or decreases the pressure dependence of spall strength significantly.

5. PREDICTING STATISTICS OF INTERGRANULAR DAMAGE IN POLYCRYSTALS

In this chapter, we seek to analyze the dominant factors governing experimental observation of the correlation of intergranular damage localization and GB misorientation angles (Wayne et al., 2010; Brown et al., 2015) in a systematic manner. We singled out the effect of cohesive GB strength on this intergranular damage localization study. The details of the method and the results are to be provided in the following sections.

5.1 Methodology

In order to evaluate the roles of inherent GB weakness versus the mechanics of GBs behind observed trends in the preferential localization of intergranular damage, we single out the mechanics (i.e. elasticity and plasticity) of neighboring grains by explicitly modeling individual GBs as perfectly bonded interfaces, i.e. without any intrinsic local degradation of strength associated with various GB characteristics.

5.1.1 Idealized BVP for high-throughput analysis

In order to study the damage localization preference we confine our attention to a simplified bicrystal structure (see Fig. 5.1), rather than modeling the full polycrystal microstructure. As such, the effects of misorientation across GBs can be isolated from the effects of GB alignment with respect to loading direction, which are also known to be significant in certain loading cases (Krishnan et al., 2015; Fensin et al., 2014). In particular, it has been observed from incipient spallation shock loading experiments of polycrystalline

The present chapter is based on a publication by Nguyen et al. (2019).

copper that the population of GBs on which voids first nucleate is primarily those GBs whose interface normal direction is closely aligned with the direction of shock wave propagation (Fensin et al., 2014). Therefore, we focus our attention on those perpendicular GBs that are most susceptible to incipient failure.

Figure 5.1 shows a schematic of the two-dimensional (2D) model of a GB structure loaded under conditions of macroscopic uniaxial tensile strain together with microscopic plane strain employed within this work. The length and height of the domain of the GB structure are $L = 120$ μm in the **X** direction and $H = 120$ μm in **Y** direction, respectively. For all cases investigated in this work, the GB is at the mid-thickness of the specimen with the corresponding interface normal, $\mathbf{n}_{\text{gb}}$, aligned along the **X** direction. The GB interface is modeled as having the same inherent strength as material points in the grain interior. In other words, we introduce no *ad hoc* rules to represent an *a priori*-assumed inherent interface weakness. The structure is meshed with 240 elements of Abaqus C3D8R type, comprising a layer of one element throughout the thickness along the out-of-plane direction (**Z** direction). To achieve plane strain conditions, kinematic constraints are applied to

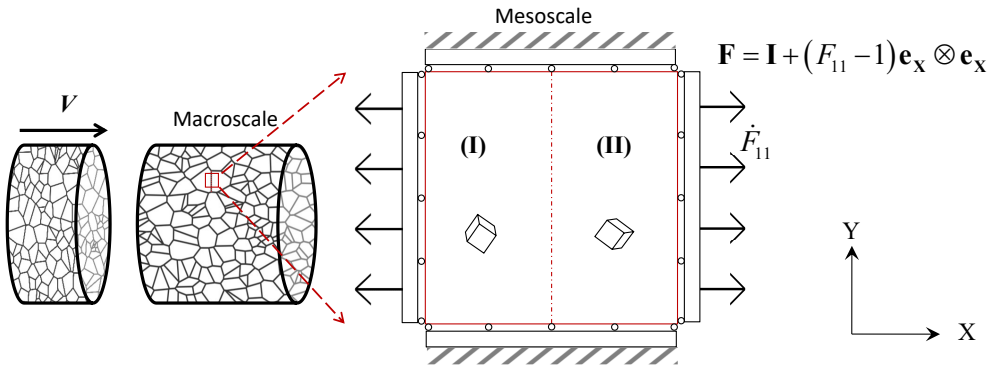

Fig. 5.1: On the left, a schematic of a plate impact experiment with a target plate being impacted by a thinner flyer plate at an impacted velocity $\boldsymbol{V}$. On the right, an idealized GB structure near the spall plane with the GB interface marked as a dashed line. Displacement is prescribed on the boundary of the GB structure in order to obtain macroscopic uniaxial strain at constant engineering strain rate.

the front ($Z = +$) and back ($Z = -$) nodes, such that the total out-of-plane strain is zero. As a result of this plane strain condition, the combination of elastic and plastic strain in the **Z** direction is zero, while plastic slip in the out-of-plane direction is generally non-zero. Twelve elements are equally spaced vertically across the specimen height (Y direction), while the mesh is more refined with 20 elements along the **X** direction and biased such that the element length is reduced to 1.47 μm near the interface to capture the stronger gradients in the vicinity. A mesh convergence study was performed to determine that this particular mesh resolution is adequate, i.e. doubling the total number of elements resulted in less than a 3% change in our quantities of interest (ε_{f}), which will be described further in the subsequent section.

Due to the high aspect ratio between the diameter and the thickness of a target plate in a plate impact test, the deformation at a material point inside the plate can be simply approximated as uniaxial deformation (Lloyd et al., 2014a; Austin and McDowell, 2012), i.e. $\mathbf{F} = \mathbf{I} + (F_{11} - 1)\mathbf{e_x} \otimes \mathbf{e_x}$, with $F_{11} < 1$ during the compression phase and with $F_{11} > 1$ during the tension phase caused by interaction of rarefaction waves. These boundary conditions imposed on each GB BVP were selected in order to enforce "macroscopic" uniaxial deformation across the GB. This condition is nominally and macroscopically achieved for an isotropic solid under shock compression and rarefaction because of the inertial resistance to transverse motion and the alignment of the polarization of the longitudinal wave with the direction of wave propagation. In actuality, the anisotropy of the individual crystals will lead to local wave dynamics which do not precisely satisfy this condition locally. Including details of actual wave dynamics at a grain boundary would require a full polycrystal calculation, such as in Moore et al. (2018). On the other hand, we are interested in understanding the extent to which grain boundary damage can be understood through simple approximations. Consequently, we make the approximation of uniaxial strain imposed along the boundaries of each GB, recognizing that this is a simplified representation of

the full in-situ response of a GB. Furthermore, because the BVP incorporates elastoplastic deformation, the compression phase may enhance the effect of plasticity (incompatibility) on the damage localization (e.g. via dislocation/GB interaction). However, we further simplify the analysis by addressing only the deformation associated with tensile loading, while acknowledging that the observed effects of plasticity on damage localization may be modified in a full compression/tension cycle. The value of the axial (engineering) strain rate is $\dot{F}_{11} = 10^6 \text{s}^{-1}$ throughout all calculations discussed here. While there are not direct measurements of the stress history from experimental efforts at incipient spall, Escobedo et al. (2011) performed plate impact experiments on polycrystalline copper impacted by a Quartz projectile at approximately 80 m/s and estimated spall strengths of approximately 1.3-1.4 GPa for copper and the resulting strain rates. Perez-Bergquist et al. (2011) performed similar experiments of polycrystalline copper flyer impacting a copper bicrystal at 170 m/s and observed orientation dependence of the ensuing void nucleation. While they did not provide an estimate of the stress magnitudes, **?** simulated these experiments with a single crystal model that did not include damage nucleation and showed peak tensile stresses on the order of 2GPa and strain rates of 10^6-10^7 s^{-1}. From those results, one can infer the rate of tensile stress accumulation of approximately 25 GPa per microsecond during interaction of the rarefaction waves. Turley et al. (2018) provided an estimate of tensile strain rates and spall strength (order 2GPa) based on analysis of velocimetry from several single crystal copper plate impact experiments. Advances in in-situ diagnostics, such as diffraction to measure lattice dimensions, will lead to a more detailed assessment of the stress history in the future. In the meantime, the evolution of deformation and stress provided by our simple loading conditions is consistent with that observed in the present literature; within our calculations, the rate of tensile stress accumulation is on the order of 100 GPa per microsecond approaching spall strengths of the order of 3 GPa

The GB structures are loaded in uniaxial tensile strain through the prescription of the

following boundary and initial conditions. Nodes along the left-most edge ($X = 0$) are restrained such that $V_{\mathbf{X}}(X = 0, t) = \mathbf{0}$. Nodes along the right-most edge are pulled in tension at constant velocity such that $V_{\mathbf{X}}(X = L, t) = \dot{F}_{11}L$. The vertical velocities along these edges ($X = 0$ or $X = L$) are unconstrained. The bottom and top edges ($Y = 0$ and $Y = H$, respectively) are restrained to ensure macroscopically uniaxial strain conditions, i.e. $V_{\mathbf{Y}}(Y = 0, t) = V_{\mathbf{Y}}(Y = H, t) = 0$, while the longitudinal velocities along these edges remain unconstrained. In order to avoid an artificial tensile wave emanating from the right-most boundary at $t = 0$ and to minimize artificial local wave dynamics throughout the domain, we apply an affine initial velocity field $\mathbf{v}(\mathbf{X}, t = 0) = \dot{\mathbf{F}} \cdot \mathbf{X}$. This initial condition is consistent with a quasi-uniform and quasi-steady deformation. These loading constraints idealize the nearly constant strain rate at the spall plane that has been commonly observed in spallation studies (e.g. Grady, 1988).

In-situ grain boundaries are likely affected by two scales of inertial response. Microscopically, there is an inertial resistance of the material surrounding nucleated voids, which serves to impede or accentuate their instantaneous growth rate. Mesoscopically, the material inertia affects the local wave dynamics in the interaction zone of the dominant macroscopic wave. The GB BVP used here includes the microscopic effects of inertia associated with damage accumulation through the constitutive equations which include pertinent terms in damage evolution (Nguyen et al., 2017), while omitting the mesoscopic inertia consistent with our simplified representation that excludes local wave dynamics. In other words, the microinertia of void growth is not affected by the manner of the deformation (i.e. whether it is induced by homogeneous loading or local wave dynamics).

A further departure from the in-situ polycrystal behavior is made by our analysis, in that we omit the shock induced hardening associated with an initial compression wave. Including these effects require a consideration of a large range of initial compressive shock wave magnitudes. We believe that the trends and conclusion obtained from the present

analysis is important as it isolates the elastic and plastic mismatch across gain boundaries without adding further complications of differing levels of post-shock slip resistance; while this would be an interesting aspect to isolate and study in its own regard, it is outside the scope of the present investigation.

Crystallographic orientations were assigned (either randomly or selectively) in each grain to obtain misorientation across the GB; details of crystallographic orientation are given in section 5.2. We have used numerical simulations of this BVP with the help of an appropriate constitutive model to perform a high-throughput analysis generating sufficient statistics to understand the role of the mismatch in elastic and plastic properties on the process of damage localization at GBs.

5.1.2 Constitutive model selection

Predicting the failure of polycrystals subjected to high strain rate requires an appropriate plasticity and damage model to account for relevant physics and crystallography. Classical mean-field micromechanics, such as Mori-Tanaka self-consistent (Qu and Cherkaoui, 2006) and viscoplastic self-consistent (Lebensohn and Tomé, 1993), are not capable of the large stress and strain gradients that develop near a GB without further enhancements to consider nearest neighbor interactions. These methods are indeed attractive for bulk response of polycrystals subject to fairly uniform deformation fields, but are poor choices for localization problems. A crystal plasticity (CP) approach can predict a more accurate stress distribution in the vicinity of a GB, but is alone incapable of predicting damage initiation and propagation. Focusing on the inherent cohesive strength of GB, CP together with the cohesive zone approach (Clayton, 2005; Vogler and Clayton, 2008) can be used to model interface debonding. However, such models (Clayton, 2005; Vogler and Clayton, 2008) are incapable of modeling transgranular void growth, which is commonly observed in experiments (Escobedo et al., 2011; Perez-Bergquist et al., 2011), and *a priori* assume

that there is an intrinsic strength associated to GBs. The approach of using CP with explicitly resolved individual voids (Lebensohn et al., 2013) is appealing, but the associated computational cost is not feasible for the present desired high-throughput study. Therefore, we use the current framework for modeling dynamic void growth within single crystals.

In addition to calculations performed in Abaqus/Explicit employing the CPD-FE model, a smaller subset of quasi-static calculations were performed in Abaqus/Standard using its anisotropic elasticity model for the purpose of isolating the effects of crystal elasticity from elastoplasticity.

5.2 Results and discussion

5.2.1 Comparison of model with experiments: the role of mechanics as distinct from GB disorder

Motivated by the experimental observations of GB characteristics (e.g. misorientation angle) associated with preferential nucleation and growth of damage during incipient spallation experiments (Wayne et al., 2010; Brown et al., 2015), we use the GB structure setup described in the previous section and Fig. 5.1 to explore the role of elastic and plastic anisotropy in discerning between GBs that are more or less favorable for damage localization.

In order to focus on the effect of GB misorientation on damage localization, the effects of initial distributions of material substructure (i.e. dislocation density and void distribution) are suppressed by assigning an identical and uniform distribution of substructure for all GB structures (see Table 5.1 for detail), and identical crystal elastic stiffness (as written in the crystallographic basis), plasticity and damage parameters (see Nguyen et al. (2017) for detail).

In Table 5.1, the spacing of void nucleation sites, $\ell_v = 30$ μm, is (coarsely) approximated from the dimple spacing on the fracture surface of spalled single crystal copper

Table 5.1: Various initial microstructural parameters utilized in the current CPD-FE predictions. The values of all other model parameters not explicitly reported here are provided in Nguyen et al. (2017).

Microstructural parameter	Symbol	Value	Unit
Initial mobile dislocation density	$\varrho_{m,0}^{(\alpha)}$	50	μm^{-2}
Initial immobile dislocation density	$\varrho_{im,0}^{(\alpha)}$	50	μm^{-2}
Spacing of void nucleation sites	ℓ_v	30	μm
Initial porosity	φ_0	0.005	$-$

identified from Perez-Bergquist et al. (2011). The initial porosity, $\varphi_0 = 0.005$, is set so as to obtain an approximate single crystal spall strength $\mathcal{R}_{cr} \sim 2$ GPa with the given initial dislocation density (see Nguyen et al. (2017)). $\mathcal{R}_{cr}$ is an approximation for incipient spall strength, which was measured in Turley et al. (2018) to be $\sim$ 2 GPa for single crystal copper.

We define the macroscopic strain at incipient failure, ε_{f}, as the value of axial engineering strain recorded when any point within the specimen reaches the coalescence porosity (i.e. $\varphi^{max} = \varphi_{cr}$). The coalescence porosity, $\varphi_{cr} = 0.5$, is chosen as an upper bound for sufficient level of local damage that was detected (by EBSD) in Brown et al. (2015), where disk and needle-shaped voids were observed on the boundary, implying the presence of coalesced voids. We note that the trends observed from the present investigation, which are presented in the following sections, are not highly sensitive to the value of coalescence porosity. We associate smaller values of ε_{f} with an increased likelihood for the particular GB structure to develop damage localization under spall conditions.

Figure 5.2 shows contour plots of the porosity field at incipient failure for five GBs of various misorientation angles (θ). The first four columns correspond to a particular GB structure formed by initially aligning the [001] and [110] crystal directions with the respective **X** and **Z** (out-of-plane) axis in the specimen coordinate system for both crystals.

Then grain **(I)** is rotated by an angle θ about the **Z** axis. The last column corresponds to a $\Sigma 3\{111\}$ twin boundary (TB). Each contour plot corresponds to the state when the local porosity first reaches the coalescence porosity, which corresponds with the incipient failure strain, ε_{f}, whose value is indicated at the bottom of each contour plot. In all of the examined GBs, though porosity evolves inside either (or both) of the grains, porosity localizes at the interface, which is in agreement with experimental observations (Wayne et al., 2010; Brown et al., 2015). Noting that all positions within each grain have the same initial conditions and properties, this localized failure is solely due to the elastic and plastic incompatibilities across the GB.

In these cases, the damage more dominantly accumulates within one grain, particularly for the θ = 45° and non-twin θ = 60°; this behavior is in agreement with experimental observation (Krishnan et al., 2015). Furthermore, the strain at incipient failure, ε_{f}, varies with respect to misorientation angle. In the leftmost four columns (cases with the same [110] rotation axis), the strain at incipient failure reduces with increasing misorientation angle. However, given the same misorientation angle of 60°, the strain at incipient failure is considerably larger (i.e. higher GB resistance to failure) for the TB than for the non-twin 60° GB. This result implies that misorientation angle by itself is not an adequate GB characteristic to predict intergranular damage localization.

In addition, the damage tends to localize toward the upper or lower boundaries of the bicrystal. This is largely an artifact of the anisotropy of the crystals. The elastic moduli coupling between axial and transverse deformation (e.g. C_{61} and C_{51} in the specimen orientation) are generally non-zero and different between the two grains. For the cases in Fig. 5.2, C_{61} in grain **(I)** is roughly 3-15% of C_{11} and zero in grain **(II)** (right) for the non-twin structures, and approximately zero in both grains for the $\Sigma 3\{111\}$ case. Therefore, imposing zero vertical displacement on upper/lower boundaries as well as plane strain boundary conditions induces a small (but non-negligible) stress concentration at either

the upper or lower interface edges. This slightly biases GB failure toward those edges. Note that we carried out an additional set of calculations (not shown here) utilizing periodic boundary conditions on all lateral boundaries. These periodic simulations fully suppressed the small bias for damage localization towards the upper/lower boundaries shown in Fig. 5.2. That said, the general trend of the dependence of GB misorientation on conditional probabilities shown in Fig. 5.4 was fairly insensitive to the precise nature of lateral boundary conditions, i.e. rigid displacement constraints versus periodic boundary conditions.

In order to better understand the statistical nature of intergranular spall failure, a large suite of 2,000 simulations, each with randomly chosen orientations for grain **(I)** and **(II)** shown in Fig. 5.1, was conducted. The orientations for each crystal were randomly selected from a uniform distribution over all possible orientations in SO(3), leading to a Mackenzie distribution of all possible distinctive disorientation angles over the interval [0°, 62.8°], for materials with cubic symmetry (Mackenzie, 1958; Handscomb, 1958). Each of the 2,000 GB structures was loaded under tension to an applied strain of 20%, which roughly corresponds to the total strain imposed during incipient spall failure.

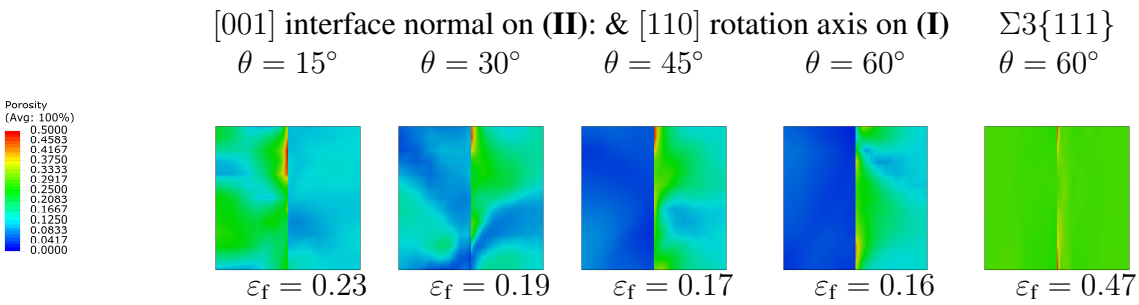

Fig. 5.2: Porosity contours at incipient failure when the bicrystal is subject to plane strain constraints. Axial strain is written at the bottom of each contour. The first four structures correspond to [001] interface direction and [110] rotation axis.

The Bayesian conditional probability to find a GB with incipient failure prior to reaching axial strain $\varepsilon_{\text{app}} = 0.2$, given a misorientation angle of θ was computed as $\mathrm{P}\left(\varepsilon_{\mathrm{f}} < \varepsilon_{\text{app}} \left| \theta \right.\right) = \mathrm{P}\left(\theta \left| \varepsilon_{\mathrm{f}} < \varepsilon_{\text{app}} \right.\right) \times \mathrm{P}\left(\varepsilon_{\mathrm{f}} < \varepsilon_{\text{app}}\right) / \mathrm{P}\left(\theta\right)$ from the results of the 2,000 simulations. By computing the conditional probabilities, any bias associated with the nonuniform distribution of misorientation angle is eliminated (Wayne et al., 2010; Brown et al., 2015). The axial engineering strain ε_{app} is a limit that (while selected somewhat arbitrarily) is indeed in the reasonable range of magnitudes for tensile strain associated with incipient spall (yet, perhaps not complete failure) of polycrystalline copper. In order to enable direct comparison with the experimental results of Brown et al. (2015), we use the same bins of 5° in the interval [0°,65°] used in their study for our calculations. The margin of error for 95% confidence interval is also calculated for each bin of misorientation angle. The margins of error are computed by simply multiplying the z-score ($Z^* = 1.96$ for 95% confidence interval) by the standard error of the statistic, i.e. $\sqrt{\frac{p_{\text{bin}}(1-p_{\text{bin}})}{n_{\text{bin}}}}$, where n_{bin} is the GB count in each bin, and p_{bin} is the proportion that satisfy the condition $\varepsilon_{\mathrm{f}} < \varepsilon_{\text{app}}$, of the corresponding bin (Lohr, 2009). This margin of error maximizes at $p_{\text{bin}} = 0.5$ and increases as the sampling size in each bin decreases (e.g. when misorientation approaches upper and lower

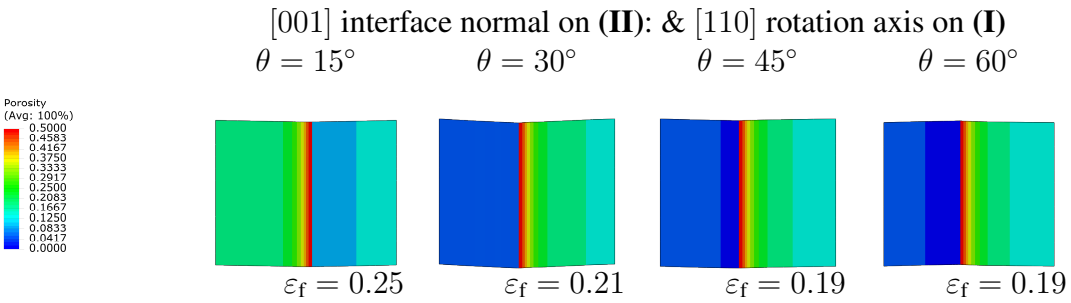

Fig. 5.3: Porosity contours at incipient failure when the bicrystal is subject to 3D periodic boundary condition instead of plane strain constraints. Axial strain is written at the bottom of each contour.

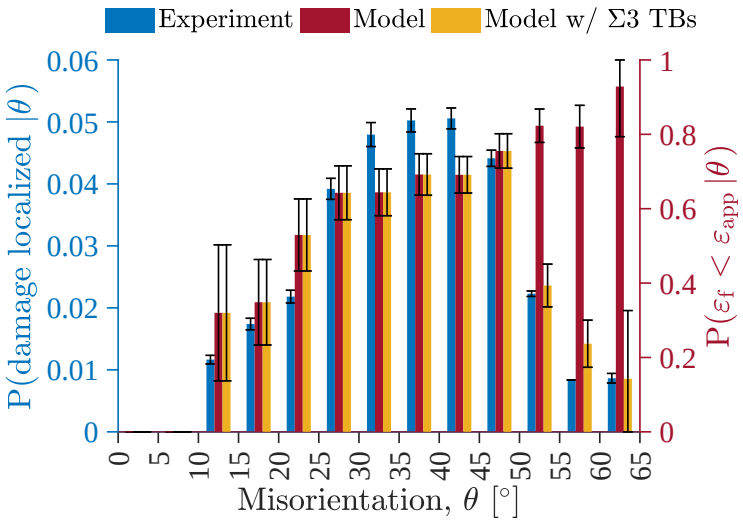

Fig. 5.4: Conditional probability from experiment and simulations: (blue) probability to find damage localized at GB at given misorientation angle θ, experimental result for as-received material, reproduced here from Brown et al. (2015); (maroon) probability to find a GB with $\varepsilon_{\text{f}} < \varepsilon_{\text{app}}$ at given misorientation angle θ, simulation result from 2000 randomly generated misorientation structures; (yellow) probability to find a GB with $\varepsilon_{\text{f}} < \varepsilon_{\text{app}}$ at given misorientation angle θ, simulation result from 2,000 randomly generated misorientation structures with 74% of $\Sigma 3$ TBs.

limits in Mackenzie's distribution). The same margin of error concept is used throughout the chapter.

The resulting conditional probabilities (in maroon) are plotted in Fig. 5.4 and compared with corresponding observations from experiments of Brown et al. (2015) (in blue). The margin of error is plotted as an error bar for each bin. Differences in the absolute magnitudes of these conditional probabilities between experiment and simulation are expected due to the position of the examined cross section area within the polycrystalline experimental specimen, i.e. the volume of the material subjected to tensile loading surrounding the precise spall plane. A larger examined volume results in a smaller fraction of damaged boundaries ($\frac{1164}{50438} = 0.0231$ for data set reproduced in Fig. 5.4 Brown et al. (2015)). Therefore, we focus not on specific magnitudes, rather similarities or differences

in the trends observed from the previous experiments and these results.

Despite the idealizations associated with the simulated GB structures, including uniaxial strain boundary conditions, neglecting initial shock compression, and the omission of any variations in GB cohesive strength as a function of GB character, the CPD-FE model reproduces most of the trends observed in the experiments, adding to the credibility of the model's capabilities. As seen in Fig. 5.4, the conditional probability for experiments and model is negligible at small misorientation angle ($\theta \leq 5^{\circ}$) and continues to increase up to $\theta \approx 40^{\circ}$. The trends in P($\varepsilon_{\mathrm{f}} < \varepsilon_{\mathrm{app}} \,|\theta$) increasing with misorientation angle in the interval $0 \leq \theta \leq 40^{\circ}$ imply an increased likelihood of damage localization with respect to misorientation angle over this range, which is consistent with the conclusions reported by both Wayne et al. (2010) and Brown et al. (2015). The agreement between our model, which makes no explicit accounting for inherent GB weakness, and the experimental observations suggests that the preferential selection of GBs for the development of ductile damage over the range of misorientation angle $0 \leq \theta \leq 40^{\circ}$ can be explained by mechanics alone. In other words, the mismatch in elastoplastic properties across the GB, rather than inherent weakness attributed to GB disorder, may effectively define the role of a GB in ductile damage processes. This plausible dependency is analyzed in greater detail in subsection 5.2.3 of the chapter.

On the other hand, as the misorientation angle increases through the range $50^{\circ} \leq \theta \leq 62.8^{\circ}$, the conditional probability of failure from the simulation results does not exhibit the same decline as observed in experimental data. Based on results from their incipient spall plate impact experiments on polycrystalline copper, Escobedo et al. (2011) report that the most prevalent GB structure with a misorientation $\theta \approx 60^{\circ}$ is the $\Sigma 3$ $\{111\}$ TB and that it is indeed more resistant to the development of damage than other, less prevalent, GBs with $\theta \approx 60^{\circ}$. Consequently, they conclude that damage preferentially localizes at other high angle GB (c.f. figure 11 in Escobedo et al. (2011)). The remarkably

higher resistance to intergranular damage of $\Sigma 3$ $\{111\}$ TB as compared to other GBs was also reported in various experimental observations (Cerreta et al., 2012; Escobedo et al., 2013; Yang et al., 2016). There is an ongoing debate on whether the GBs' characteristics or mechanics is the dominant factor for the relatively high resistance (to intergranular damage) of $\Sigma 3$ $\{111\}$ TBs. It is plausible that this effect is associated with the relatively small GB energy for $\Sigma 3$ $\{111\}$ TBs in comparison to other high angle GBs (Wolf and Phillpot, 1989), which would manifest as a higher coherent GB strength unaccounted for in the present modeling framework. However, it is also plausible that this observation can be described by mechanics of the elastoplasticity in the vicinity of the TBs due to the continuity in elastic stiffness (in interface normal and interface in-plane directions) and maximum Schmid factor along the interface normal direction. Under uniaxial loading across the interface, this continuity in properties leads to more uniform elastic and plastic deformation fields across the $\Sigma 3$ $\{111\}$ TBs than for general GBs of 60° misorientation angle.

Further support of these observations are found in the literature. GB characteristics such as GB energy and free volume were concluded to be insignificant in determining spall strength from molecular dynamics simulations (Fensin and Hahn, 2017). $\Sigma 3$ $\{111\}$ TBs were shown to be able to dissociate and/or transmit dislocations during interaction due to their local mechanics compatibility across the GB (Dewald and Curtin, 2007; Jin et al., 2008). Escobedo et al. (2013) and Cerreta et al. (2012) provide related experimental observations of this compatibility effect on damage localization when comparing the lattice misorientation surrounding separation sites of a high-angle GB. In their experiments, non-special high-angle GBs led to intergranular damage, while $\Sigma 3$ $\{111\}$ TBs resulted in transgranular damage. They postulated that the observed relationship is attributed to the relative difference in line defect/interface interactions, e.g. dislocation pile-up versus transmission, rather than on the mismatch in anisotropic elastic or plastic properties.

From our simulation results we observe that the strain at incipient failure, ε_{f}, varies widely for all GBs with $\theta = 60^{\circ}$, depending on the rotation axis. The pertinent simulation results are summarized in Table 5.2, where it is clear that ε_{f} for $\Sigma 3$ $\{111\}$ is more than double the average value for general cases of $\theta = 60^{\circ}$. In other words, even in our purely mechanics framework that does not incorporate inherent GB energy, $\Sigma 3\{111\}$ TBs are significantly more damage resistant than all other 60° GBs.

The structures studied here include randomly generated orientations such that there is no preferential occurrence of $\Sigma 3$ $\{111\}$ TBs (or any other special GB). On the other hand, the actual polycrystalline specimens naturally exhibit a larger proportion of the GBs with $\theta \approx 60^{\circ}$ represented by the special $\Sigma 3$ $\{111\}$ boundaries (more than 60% in Escobedo et al. (2011) and more than 35% in Brown et al. (2015)). Consequently, our conditional probabilities depicted by maroon bars in Fig. 5.4 do not capture the influence of the more resistant $\Sigma 3$ $\{111\}$ TBs near $\theta \approx 60^{\circ}$. However, our inspection of the mechanical behavior of these special boundaries relative to random GBs of the same misorientation is entirely consistent with a mechanics-based discrimination of GBs preferential for the development of damage.

We consider again the analysis leading to the conditional probabilities indicated by maroon bars in Fig. 5.4, but here take into account the special $\Sigma 3$ TBs as follows. In the FCC polycrystalline copper material used (as-received) in the experimental investigation of Brown et al. (2015), approximately 74% of GBs with $\theta \sim 60^{\circ}$ were determined to be $\Sigma 3$ TBs (Brown et al., 2015). According to Brandon's criterion (Brandon, 1966), GBs of $\theta \approx 60^{\circ} \pm 8.66^{\circ}$ can be considered as $\Sigma 3$ TBs in FCC materials. Correspondingly, we have introduced the effects of this more prevalent GB by randomly selecting 74% of the GBs in our simulation suite that satisfy Brandon's criterion to be replaced with $\Sigma 3$ TBs. By repeating the analysis of conditional probabilities on this modified population of simulation results, the Bayesian probability model predictions are brought into remarkably

Table 5.2: Comparison of strain at incipient failure for a single crystal of loading orientation <111>, a $\Sigma 3$ {111} TB, a pure tilt GB and 100 random GBs each with $\theta = 60°$.

Structure	θ	ε_{f}
Single crystal	$0°$	0.53
$\Sigma 3$ {111} TB	$60°$	0.47
Pure tilt with respect to <110>	$60°$	0.15
100 random rotation axes	$60°$	0.18 ± 0.03

good agreement with the experimental observations (see yellow bars in Fig. 5.4). This agreement indicates that the entire trend of Bayesian probability observed in the Brown et al. (2015) experiments can be captured by elastoplastic mechanics without the need to invoke the concept of inherent GB weakness or disorder. Note that this may not necessarily be true for alloys, for example, with significant segregation of impurities to the GBs.

5.2.2 Decomposition of misorientation into tilt and twist

While the previous section considered correlations in the crystallographic characteristics of randomly selected GBs, here we turn attention to the relationships observed by controlled variation of tilt and twist angles. The geometry of a general GB can be defined by no fewer than five macroscopic degrees of freedom (DOFs), including three DOFs representing the rotation that brings both grains into a single crystallographic alignment (e.g. three Euler angles or two components of a rotation axis plus the misorientation angle θ), and two additional DOFs to represent the interface normal direction (Wolf and Yip, 1992; Sutton and Balluffi, 1995; Lejček, 2010). For example, pure tilt and twist GBs correspond to those whose axis of relative rotation is aligned perpendicular or parallel to the GB normal direction, respectively. For low misorientation angles (i.e. less than $15°$ (Brandon, 1966)), tilt and twist GBs can be described by particular configurations of edge and screw dislocations, respectively. Thus, relating GB behavior to a single characteristic such as

total misorientation angle may mask important relationships.

In general, any misorientation can be decomposed into a nonunique combination of tilt and twist. One decomposition of misorientation into tilt and twist is expressed as

$$\mathbf{exp}\left[\theta\widehat{\mathbf{n}}\right] = \mathbf{\Delta R} = \mathbf{R}_{II}\mathbf{R}_{I}^{T} = \mathbf{exp}\left[\theta_{\text{twst}}\widehat{\mathbf{n}}_{\text{twst}}\right]\mathbf{exp}\left[\theta_{\text{tilt}}\widehat{\mathbf{n}}_{\text{tilt}}\right], \tag{5.2.1}$$

where $\mathbf{n}$, $\mathbf{n}_{\text{tilt}}$ and $\mathbf{n}_{\text{twst}}$ correspond to the rotation axes for the total GB misorientation rotation, tilt, and twist angles, θ, θ_{tilt}, and θ_{twst}, respectively. The twist axis, $\mathbf{n}_{\text{twst}}$, is aligned with the GB normal, and the tilt axis is orthogonal, i.e. $\mathbf{n}_{\text{tilt}} \cdot \mathbf{n}_{\text{twst}} = 0$. Note that we use the $\widehat{\cdot}$ operator to denote the skew tensor whose axial vector is given by the argument, $\cdot$. $\mathbf{R}_I$ and $\mathbf{R}_{II}$ are the (sometimes referred to as "active") rotation tensors from specimen coordinate system to the corresponding crystal **(I)** and **(II)** coordinate systems. Due to the cubic symmetry of FCC, there is more than one equivalent tilt/twist decomposition for the same physical GB. To eliminate this ambiguity, $\mathbf{\Delta R}$ is selected to be the disorientation (which is defined as the $\mathbf{\Delta R}$ with the minimal rotation angle around an axis in the fundamental zone (FZ) (Mackenzie, 1958)), so that the tilt/twist decomposition is unique for each physical GB. For example, the decomposition of $\Sigma 3$ TB using Eq. (5.2.1) results in $\theta_{\text{twst}} = 60^\circ$ with $\mathbf{n}_{\text{twst}} = \frac{1}{\sqrt{3}}[111]$ and $\theta_{\text{tilt}} = 0^\circ$.

A statistical analysis of the correlation between misorientation, twist, tilt, and ε_{f} for the set of 2,000 GBs introduced in subsection 5.2.1 is presented in Fig. 5.5. The plots along the diagonal of Fig. 5.5 are the kernel density estimates of the probability distribution function for each corresponding measure (using a normal distribution). The scatter plots below the diagonal show possible correlations between each pair of corresponding measures. A linear regression is superposed over the top of each scatter plot with a red line to indicate trends. The Spearman correlation coefficient (r_s) is printed above each scatter plot to characterize the monotonic correlation of the particular pair of measures.

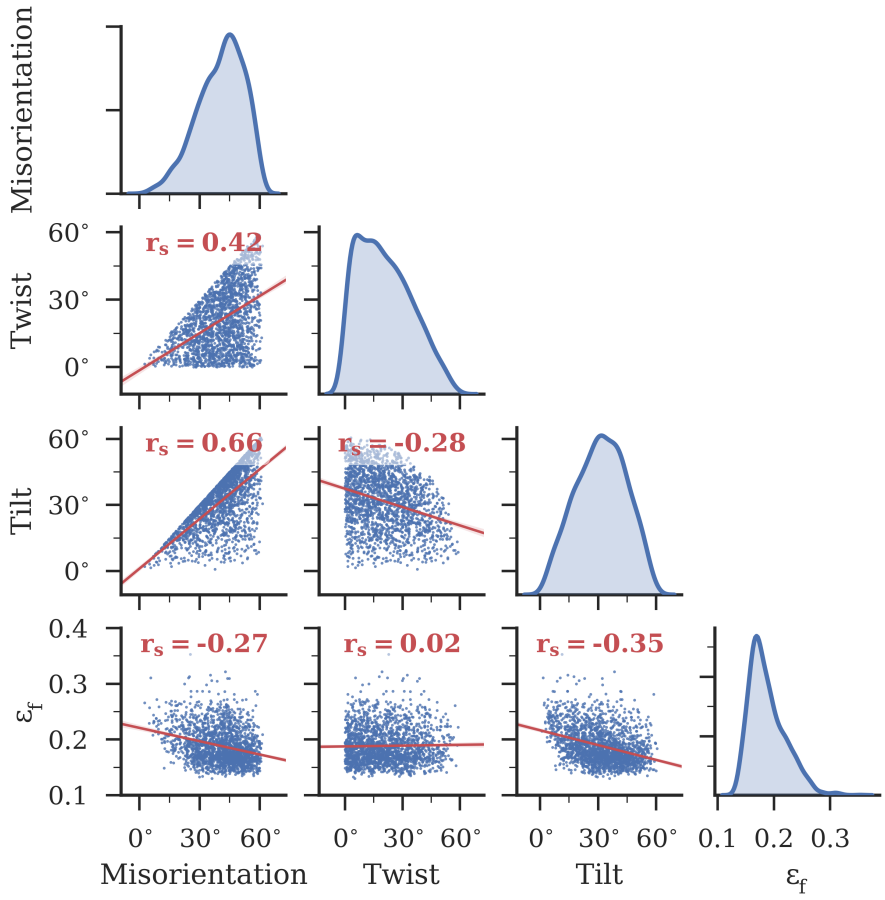

Fig. 5.5: Kernel distribution estimates (on the diagonal) of misorientation, twist, tilt and ε_f. Scatter plots (below diagonal) with superimposed linear regressions and Spearman's correlation coefficients for the corresponding row and column measures.

As can be seen clearly in Fig. 5.5, the distributions of all geometric parameters (misorientation, tilt and twist) are nonuniform as a result of the cubic symmetry. The distribution of misorientation angle is approximately the Mackenzie distribution for unique disorientation within the FZ (Mackenzie, 1958). The upper and lower limits of tilt and twist are the same as those of misorientation, due to the choice of the minimal rotation decomposition. The scatter plots of tilt and twist angle with respect to misorientation angle each exhibit the expected strong relationship (cf. Eq. (5.2.1)) between these descriptors of the

relative rotation. While tilt and twist are orthogonal, and hence independent characteristics in randomly constructing a GB, they are strongly correlated when subjected to the constraint of computing relative disorientation within the FCC FZ. Consider, as the twist angle increases towards its upper limit, the range of viable tilt angles associated with a total disorientation within the FZ necessarily decreases. This relationship is clearly exhibited by the non-linear upper boundary of the range of tilt angles and the apparent correlation with twist angle.

Consistent with the previous sub-section 5.2.1, Fig. 5.5 shows that the strain to failure, ε_{f}, is inversely proportional to the misorientation angle; as the GB misorientation is increased it becomes more susceptible to the growth of voids and localization of damage. However, the decomposition of the GB misorientation into tilt and twist angle enables a more specific observation, namely that it is the GB tilt angle which is dominantly related to the apparent strength of a GB.

This observation is quantified by the order of magnitude difference between the Spearman correlation coefficients, which indicate negligible correlation between ε_{f} and twist ($\mathrm{r_s} = 0.02$), while indicating a moderate monotonic relationship between ε_{f} and tilt ($\mathrm{r_s} = -0.35$).

Recalling that $\Sigma 3$ TBs can be constructed by a pure twist, i.e. $\theta_{\mathrm{tilt}} = 0^{\circ}$, their high strain at incipient failure (Table 5.2) is entirely consistent with our mechanics-based assessment of GB strength. In addition, these results suggest that stochastic nature of the relationship between the misorientation angle and the liklihood for development of damage on a particular grain boundary apparent in Fig. 5.4 and in Brown et al. (2015) may be less ambiguously understood through relationships with twist and tilt. In other words, the misorientation angle, without consideration of rotation axis, is an insufficient description of GB character in the context of ductile damage. The higher Spearman coefficient relating tilt angle and ε_{f} ($\mathrm{r_s} = -0.35$) as compared to that relating misorientation angle and ε_{f}

($r_s = -0.27$), combined with the effectively uncorrelated relationship between twist angle and ε_f supports our conclusion that the tilt angle is a better GB descriptor than misorientation angle in characterizing damage localization. However, there is only a moderate, i.e. not a strong, quantitative correlation between the tilt angle and GB resistance to damage. Recall that we have chosen to use a characterization of the GB that is based on the disorientation (i.e. smallest misorientation within FZ of FCC symmetry) decomposed into tilt and twist components. This characterization is unambiguous on account of Eq. (5.2.1) for the decomposition of a disorientation. However, a given characterization of GB in this approach could equally be described by a symmetrically equivalent rotation that is not the disorientation. Some such equivalent relative orientations may be decomposed using our tilt/twist decomposition into a description that is actually a smaller tilt angle. For example, the symmetric twin boundaries $\Sigma5$, $\Sigma7$, $\Sigma9$, and $\Sigma11$ are all described using Eq. (5.2.1) as pure tilt boundaries, yet they are equivalently described as a pure twist of 180° about the tilt boundary normal. Thus, it is plausible that the observed correlation would be stronger if one considered a "minimum tilt angle" description of each GB; however, we prefer to use the more canonical description of the GB and accept that the correlation with tilt angle is only moderate in this regard.

5.2.3 Key governing factors: elastic and plastic anisotropy

The agreement between our modeling results and the previous experimental observations (c.f. Fig. 5.4) implies that the mechanics at interfaces may be sufficient to explain the preferential growth of damage at certain types of GBs without invoking inherent GB disorder or weakness. This subsection aims to provide a better understanding of the underlying interfacial discontinuity in elastoplastic properties that gives rise to these GB relationships, by further exploring the role of the mismatch in elasticity and plasticity across GBs and the corresponding relationships with observed damage localization.

In our framework, the main driving force for ductile void growth is the hydrostatic stress, while the inertia associated with mass surrounding a void and the matrix flow stress provide the resistance to void growth (Nguyen et al., 2017). Therefore, at an equivalent state of macroscopic, or far-field stress, a higher local fluctuation in the pressure associated with a stress concentration factor (SCF) will promote early void growth. Here we define SCF as the maximum hydrostatic stress near the interface normalized by the volume-averaged mean hydrostatic stress. Prior to any appreciable void growth, the SCF for a GB structure is determined based on the mismatches in elastic stiffness and the ease of plastic slip across the GB. Although plastic slip is isochoric, the associated heterogeneous deformation affects the distribution of stresses throughout the structure, thus modifying the pressure distribution.

It is convenient to introduce a parameterization of the mismatch in anisotropic elasticity similar to Dundur's parameter (Schmauder and Meyer, 1992). In this work, we quantify the mismatch in anisotropic elasticity in a given direction, $\boldsymbol{\beta}$, across a GB interface according to

$$\eta_{\boldsymbol{\beta}} = 2\frac{\left|C_{\boldsymbol{\beta}}^{(I)} - C_{\boldsymbol{\beta}}^{(II)}\right|}{C_{\boldsymbol{\beta}}^{(I)} + C_{\boldsymbol{\beta}}^{(II)}}, \tag{5.2.2}$$

where superscripts (I) and (II) refer to respective crystals, and $\boldsymbol{\beta}$ is the direction of interest. The mismatch factor is a function of both misorientation and the elastic coefficients (i.e. C_{11}, C_{12}, C_{44}). The hydrostatic SCF depends nonlinearly on the stiffness incompability factors in each specimen direction, $\eta_{\mathbf{X}}$, $\eta_{\mathbf{Y}}$ and $\eta_{\mathbf{Z}}$. The three incompatibility factors in specimen directions, $\eta_{\mathbf{X}}$, $\eta_{\mathbf{Y}}$ and $\eta_{\mathbf{Z}}$, all have the same order of magnitude. Among the three factors, $\eta_{\mathbf{X}}$ corresponds to the variation in axial stress normal to the GB. This factor, i.e. $\eta_{\mathbf{X}}$, is similar to Dundur's parameter, which uses the directional Young's modulus to quantify the elasticity mismatch of a composite consisting of two different isotropic elastic materials (Schmauder and Meyer, 1992). Dundur's parameter is frequently applied to indicate

the relative likelihood for crack propagation along a composite interface. Our selection of the crystal stiffness across the interface, rather than Young's modulus, is motivated by the macroscopic uniaxial strain conditions associated with incipient spallation in plate impact experiments. The directional stiffness coefficient can be computed by rotating the fourth-order elastic stiffness tensor from the crystal basis to specimen basis (Bower, 2009) and selecting the appropriate coefficients. Application of an arbitrary twist, c.f. Eq. (5.2.1), to either of the two crystals does not affect the uniaxial stiffness along the interface normal direction, thus demonstrating the independence of $\eta_{\mathbf{X}}$ on GB twist angle.

We choose a measure of plasticity mismatch that is in a close analogy to the elasticity counterpart. Here, a normalized Taylor factor (Taylor, 1938) difference between the two crystals is used, i.e.,

$$\Delta M_{\mathrm{T}}/M_{\mathrm{T}} = 2\frac{\left|M_{\mathrm{T}}^{(I)} - M_{\mathrm{T}}^{(II)}\right|}{M_{\mathrm{T}}^{(I)} + M_{\mathrm{T}}^{(II)}}, \tag{5.2.3}$$

where $M_{\mathrm{T}}^{(I)}$ and $M_{\mathrm{T}}^{(II)}$ are Taylor factors in each crystal computed for loading normal to the GB. The Taylor factor is associated with the relative ability for a crystal with a particular orientation relative to the axis of loading to accommodate an imposed deformation via plastic flow, and can be used to predict the relative strength of textured polycrystals. An absolute Taylor factor difference, i.e. $\left|M_{\mathrm{T}}^{(I)} - M_{\mathrm{T}}^{(II)}\right|$, was used in (Lieberman et al., 2016) to quantify the plasticity mismatch in polycrystals. Our choice of normalizing the Taylor factor difference is motivated by Dundur's parameters, which intend to quantify the relative change rather than the absolute value change of stress across the interface. Our Taylor factor calculations represent the case of triaxial incompressible plastic deformation assuming equal plastic strain rates in both directions orthogonal to the grain boundary normal (Bunge, 1970; Przybyla et al., 2007). This assumption leads to the independence of Taylor factor on the crystallographic directions aligned with the specimen directions **Y** and **Z**, such that $\Delta M_{\mathrm{T}}/M_{\mathrm{T}}$ is independent of twist angle.

Scatter plots in Fig. 5.6 show the dependence of SCF and ε_{f} on $\eta_{\mathbf{X}}$, $\eta_{\mathbf{Y}}$ and $\Delta M_{\mathrm{T}}/M_{\mathrm{T}}$. A red line corresponding to a linear regression is superposed over each scatter plot along with the Spearman correlation coefficient to better visualize and quantify possible relationships. The SCF is calculated using crystal plasticity without damage at 1% axial engineering strain.

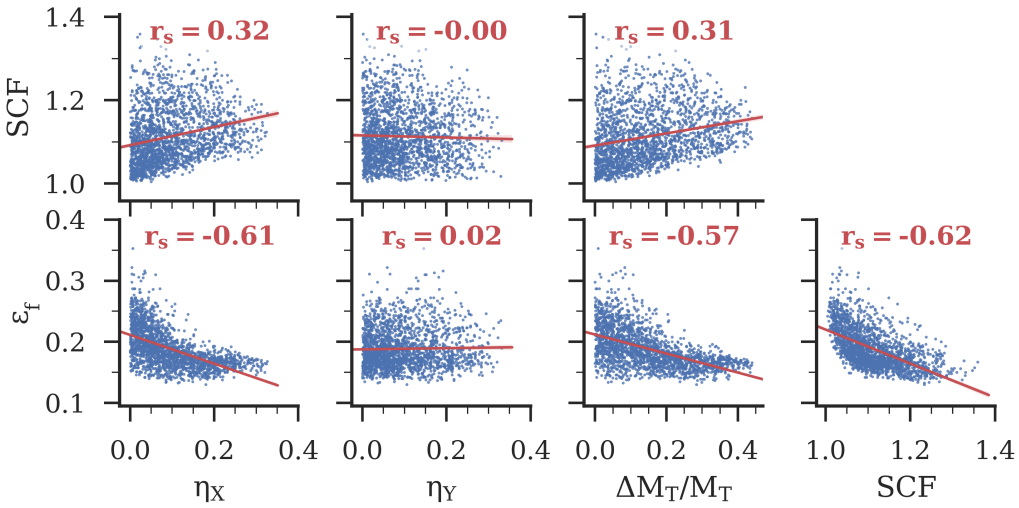

Fig. 5.6: Scatter plots with superimposed linear regressions and Spearman's correlation coefficients for the relationship between ε_{f}, SCF, elasticity and plasticity mismatches.

The order of magnitude difference between the Spearman correlation coefficients in Fig. 5.6 implies that SCF and ε_{f} are more strongly correlated with $\eta_{\mathbf{X}}$ and $\frac{\Delta M_{\mathrm{T}}}{M_{\mathrm{T}}}$ than $\eta_{\mathbf{Y}}$. $\eta_{\mathbf{Y}}$ is selected as representative of both of the lateral elasticity mismatch parameters $\eta_{\mathbf{Y}}$ and $\eta_{\mathbf{Z}}$ and the apparent lack of correlation between failure strain and $\eta_{\mathbf{Y}}$ is similarly exhibited by $\eta_{\mathbf{Z}}$. This result indicates that, perhaps expectedly, the elasticity mismatch in directions transverse to the GB normal are unimportant to the SCF and the strain to failure. Furthermore, the similarity between Spearman correlation coefficients relating SCF with $\eta_{\mathbf{X}}$ ($\mathrm{r_s} = 0.32$) and $\frac{\Delta M_{\mathrm{T}}}{M_{\mathrm{T}}}$ ($\mathrm{r_s} = 0.31$) implies that elasticity and plasticity incompatibilities

could equally explain the variations in the computed SCF for copper under purely tensile loading.

The values of the Spearman correlation coefficients relating failure strain, ε_{f}, with $\eta_{\mathbf{X}}$, $\frac{\Delta M_{\mathrm{T}}}{M_{\mathrm{T}}}$, and SCF are all greater than 0.50, which implies reasonably strong associations between the GB strength and these variables. In particular, ε_{f} is observed to decrease with increasing values of $\frac{\Delta M_{\mathrm{T}}}{M_{\mathrm{T}}}$ and $\eta_{\mathbf{X}}$, thus we conclude that GBs with larger differences in their elastic stiffnesses and their Taylor factors are more susceptible to incipient damage localization. While both $\eta_{\mathbf{X}}$ and $\frac{\Delta M_{\mathrm{T}}}{M_{\mathrm{T}}}$ are independent of twist from construction, Fig. 5.6 helps explain the observed independence of ε_{f} on twist. Moreover, this analysis provides a mechanistic understanding of why GB tilt angle is a more predictive GB characteristic than misorientation angle when assessing the likelihood of damage localization. Lieberman et al. (2016) arrived at a similar conclusion when correlating the damage location sites and Taylor factor difference of neighboring grains, although elastic incompatibility across GBs was not considered in that work. This mechanics mismatch may provide a key to explain the high damage resistance of $\Sigma 3$ TBs (with an SCF $= 1$ under these loading conditions) relative to other high-angle GBs observed in experiments (Cerreta et al., 2012; Escobedo et al., 2013), given that there has not been a clear link identified between other GB characteristics (e.g. energy, free volume) and fracture strength (Fensin and Hahn, 2017).

To visualize the effect of elastic and plastic incompatibility on the SCF, we compare the SCF at 1% axial engineering strain for the GBs constructed by tilt and twist operations (i.e. Eq. (5.2.1)), with [001] twist axis and [110] tilt axis, in the range of [0°, 45°] rotation angles. Figure 5.7 depicts the effect of variations in GB misorientation on the hydrostatic SCF for 3 scenarios: (i) with anisotropic elasticity ($A \triangleq \frac{2C_{44}}{C_{11}-C_{12}} \neq 1$) and no plasticity; (ii) with isotropic elasticity ($A = 1$) and crystal plasticity; (iii) with anisotropic elasticity ($A \neq 1$) and crystal plasticity. The tilt angle is varied along the x-axis of these plots, while

variations attributed to variation in twist angle are indicated by an error bar for each value of tilt. For case (i), plasticity, porosity and inertia were omitted from the BVP of Fig. 5.1 in order to isolate the effects of crystal elasticity on SCF. For these purely elastic, quasi-static simulations, Abaqus Standard was used to solve the BVP. The material behavior was specified using Abaqus' orthotropic elasticity model with copper elastic moduli of $C_{11} = 169$ GPa, $C_{12} = 122$ GPa and $C_{44} = 75.3$ GPa (Every and McCurdy, 1992). In case (ii), isotropic elasticity with $C_{11} = 215.12$ GPa, $C_{12} = 121.0$ GPa and $C_{44} = 47.06$ GPa (note, $A = \frac{2C_{44}}{C_{11}-C_{12}} = 1$) was used within our crystal plasticity model, in order to highlight the effects of anisotropy due solely to crystalline slip on the hydrostatic SCF. In case (iii), the general anisotropic elasticity and plasticity crystal model was used.

Comparing the three SCF curves in Fig. 5.7 reveals that both anisotropic elasticity and crystal plasticity influence the SCF; in particular, both cases that included anisotropic elasticity (with and without crystallographic slip indicated by purple and yellow curves, respectively) exhibit larger SCF than for the case with isotropic elasticity indicated by the blue curve. The role of plasticity is to reduce the variation of SCF with respect to tilt angle in comparison with the purely anisotropic elastic case. Note that the variation in SCF for the full model with anisotropic elasticity and crystallographic slip is not a simple superposition of the independent variations for the other two cases. This result suggest that, even prior to plastic deformation, the mismatch in anisotropic elasticity across a GB is significant in establishing the driving force for subsequent void growth. Consequently, we would expect materials exhibiting low elastic anisotropy to have GBs of higher ductility.

5.2.4 Extrapolation to other metals and implications for GB engineering

Up to this point in the chapter, the focus has been on copper as a representative crystalline material. In this section, we extrapolate the observations to other crystalline materials.

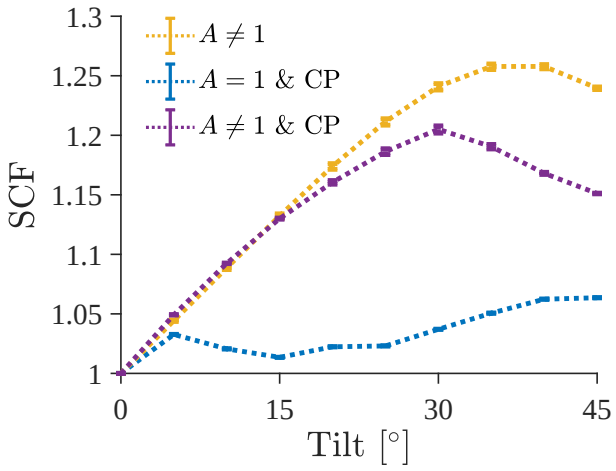

Fig. 5.7: The hydrostatic SCFs computed for three cases including (i) (in yellow) with anisotropic elasticity and no plasticity (i.e. $A \neq 1$); (ii) (in blue) with isotropic elasticity (i.e. Zener ratio, $A = 1$) and anisotropic crystal plasticity; (iii) (in purple) with anisotropic elasticity and crystal plasticity ($A \neq 1$). The SCF values are computed at 1% axial engineering strain. Error bars represent variations associated with the twist of grain **(II)** relative to [001] at fixed angles of tilt.

The negligible influence of interface in-plane elasticity mismatch and the strong influence of interface out-of-plane elasticity and Taylor factor mismatches on ε_{f} (see the bottom graphs of Fig. 5.6) motivates a prediction of SCF for general cubic materials based on the two parameters: $\eta_{\mathbf{X}}$ and $\frac{\Delta M_{\mathrm{T}}}{M_{\mathrm{T}}}$. However, it is beyond on the scope of this chapter to address the coupled manner in which $\eta_{\mathbf{X}}$ and $\frac{\Delta M_{\mathrm{T}}}{M_{\mathrm{T}}}$ can affect SCF, which is deemed to be complicated. Instead, we simply introduce a straightforward decomposition of SCF as

$$\mathrm{SCF} = \Delta\mathrm{SCF}^{\mathrm{el}}(\eta_{\mathbf{X}}) + \Delta\mathrm{SCF}^{\mathrm{pl}}(\frac{\Delta M_{\mathrm{T}}}{M_{\mathrm{T}}}) + 1, \tag{5.2.4}$$

where $\Delta\mathrm{SCF}^{\mathrm{el}}$ and $\Delta\mathrm{SCF}^{\mathrm{pl}}$ are contributions from elasticity and plasticity incompatibilities. The two functions are required to vanish where interface discontinuities vanish. The simple linear approximations that satisfy the condition are $\Delta\mathrm{SCF}^{\mathrm{el}} = \lambda^{\mathrm{el}}\eta_{\mathbf{X}}$ and

$\Delta\text{SCF}^{\text{pl}} = \lambda^{\text{pl}}\frac{\Delta M_{\text{T}}}{M_{\text{T}}}$. It should be noted that the elasticity mismatches depend on the ratio between the elastic coefficients (i.e. $C_{11} : C_{12} : C_{44}$) rather than the magnitude of individual coefficient. The Zener parameter A is a scalar index that captures this proportionality effect, which implies that $\eta_{\mathbf{X}}$ of one cubic material can be scaled by the Zener ratio. Based on calculations, the scaling factor is adopted as $\eta_{\mathbf{X}} = \frac{\ln(A)}{\ln(A_{\text{ref}})}\eta_{\mathbf{X}}^{\text{ref}}$ with A_{ref} and $\eta_{\mathbf{X}}^{\text{ref}}$ denoting the Zener ratio and elasticity mismatch for the corresponding orientation pair of a reference cubic material. Here copper is used as the reference material for the following calculation. Utilizing the above approximations, Eq. (5.2.4) can be written as

$$\text{SCF} = \lambda^{\text{el}}\frac{\ln(A)}{\ln(A_{\text{ref}})}\eta_{\mathbf{X}}^{\text{ref}} + \lambda^{\text{pl}}\frac{\Delta M_{\text{T}}}{M_{\text{T}}} + 1. \tag{5.2.5}$$

As ε_{f} is inversely proportional to SCF, the correlations motivate a simple inverse approximation of ε_{f}, i.e. $\varepsilon_{\text{f}} \propto \text{SCF}^{-1}$. However, for very small tilt angles ($\theta_{\text{tilt}} < 5^{\circ}$), ε_{f} is very sensitive to SCF. This additional sensitivity at low tilt angles can be approximately captured by the following functional form:

$$\frac{\varepsilon_{\text{f}}}{\varepsilon_{\text{f}}^{\text{ref}}} \approx \alpha\left(\lambda^{\text{el}}\frac{\ln(A)}{\ln(A_{\text{ref}})}\eta_{\mathbf{X}}^{\text{ref}} + \lambda^{\text{pl}}\frac{\Delta M_{\text{T}}}{M_{\text{T}}} + 1\right)^{-1} + (1-\alpha)\left(1 - \tanh\frac{\frac{\ln(A)}{\ln(A_{\text{ref}})}\eta_{\mathbf{X}}^{\text{ref}} + \frac{\Delta M_{\text{T}}}{M_{\text{T}}}}{0.005}\right). \tag{5.2.6}$$

In the above equation, $\varepsilon_{\text{f}}^{\text{ref}}$ is a reference strain to incipient failure for a single crystal loaded along the <100>, i.e. $\varepsilon_{\text{f}}^{\text{ref}} = 0.45$.

Figure 5.8 is the contour plot for normalized strain $\frac{\varepsilon_{\text{f}}}{\varepsilon_{\text{ref}}}$ for materials of Zener ratio and GB tilt angle. The parameters λ^{el}, λ^{pl} and α are calibrated from SCF for isotropic elasticity and cubic elasticity in combination with crystal plasticity (blue and purple curves in Fig. 5.7), ε_{f} (square markers in Fig. 5.8) for $\theta_{\text{twst}} = 0^{\circ}$. Simulation results using $C_{11} = 169$ GPa, $C_{12} = 122$ GPa and $C_{44} = 32.64$ GPa, which induces a Zener ratio equivalent to that

of aluminum ($A = 1.22$), is also plotted (diamond marker) in Fig. 5.8. The quantitative agreement between the numerical predictions (square and diamond markers) and the contour plot shows the the effectiveness of the simple functional form in Eq. (5.2.6).

The contour map (Fig. 5.8) predicting the relative variation of ε_{f} with respect to tilt and Zener ratio can be a viable tool to guide GB engineering. A polycrystal with a high fraction of high angle GBs and/or a high Zener ratio will behave in a brittle manner and be more susceptible to intergranular failure. A material with a low Zener ratio and low tilt angle GBs will be more ductile and less susceptible to intergranular failure.

In addition to Zener ratio and tilt angle, the crystallography plays an important role in the likelihood of intergranular failure. It was noted earlier that ε_{f} has a strong inverse correlation with Tayor factor difference, $\frac{\Delta M_{\mathrm{T}}}{M_{\mathrm{T}}}$ (c.f. Fig. 5.6). By construction, the Tayor factor depends on the available slip or twin systems of the crystal. For example, FCC

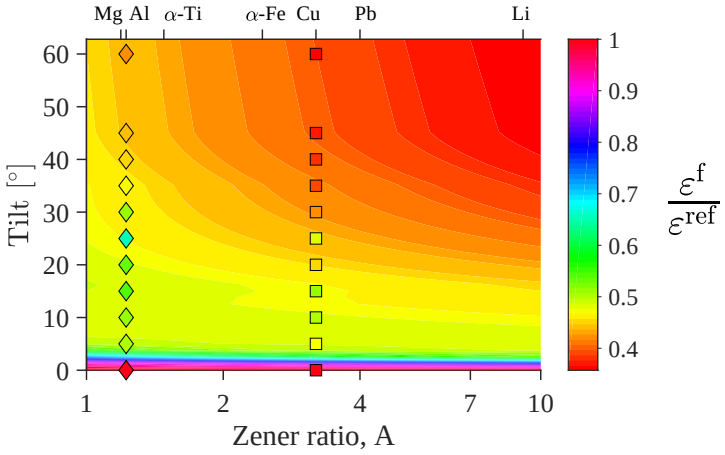

Fig. 5.8: Extrapolation of ε_{f} based on tilt, and Zener ratio, for the orientation set in Fig. 5.7 (square markers). Calibrated parameters for Eq. (5.2.6) are $\lambda^{\mathrm{el}} = 0.46$, $\lambda^{\mathrm{pl}} = 0.18$, $\alpha = 0.49$. Diamond markers are simulation results of an identical material except with a shear modulus of $C_{44} = 32.64$ GPa and a Zener ratio equivalent to aluminum ($A = 1.22$). Markers on the top of the contour box show Zener ratios of cubic materials calculated from elastic coefficients in (Every and McCurdy, 1992), and equivalent Zener ratios of magnesium (HCP) and α-Ti (HCP) from (Ranganathan and Ostoja-Starzewski, 2008).

has 12 primary slip systems, body-centered cubic (BCC) such as α-Fe can have up to 48 slip systems, and hexagon close-packed (HCP) such as magnesium has 36 (primary) slip and twin systems. Using the same set of 2,000 random orientations, the Taylor factor difference is calculated for BCC and HCP and their distribution is plotted on Fig. 5.9 for comparison.

Generally, as can be seen in Fig. 5.9, materials with more available slip systems correspond to a smaller maximum attainable mismatch in the Taylor factor across all possible crystallographic orientations. In the limiting case of an infinite number of slip systems, i.e. J_2 plasticity, the Taylor factor mismatch will vanish for all orientation pairs. A higher number of easily activated slip systems induces a lower SCF, which results in better ductility. As such, if high ductility is desired one should choose a material with a Zener ratio close to unity and many slip systems.

Some crystalline materials, particularly HCP, have slip or twin systems that are extremely difficult to activate under general loading conditions. For example, HCP magnesium has a low critical resolved shear stress (CRSS) in basal or extension twin systems, but high CRSS in pyramidal or compression twin systems (Zhang and Joshi, 2012). As a consequence, even with a total of all 36 slip and twin systems, magnesium is commonly considered a brittle material. Figure 5.9 shows an example of the Taylor factor mismatch for these restricted slip systems. When 36 slip and twin systems can be activated easily, the largest Taylor factor mismatch is less than 0.2. While with only basal slip and extension twin systems, $\sim 40\%$ of Taylor factor mismatches are larger than 0.2 with the largest values reaching 0.77. According to equation Eq. (5.2.6), doubling $\frac{\Delta M_{\mathrm{T}}}{M_{\mathrm{T}}}$ will roughly half ε_{f} for magnesium. As such, Fig. 5.9 sheds some light on the ductility of HCP materials. Generally, an HCP with similar CRSS for all slip and twin systems is expected to be significantly more ductile than an HCP with large contrasts between CRSS of various slip and twin systems, which will tend to be more susceptible to intergranular failure.

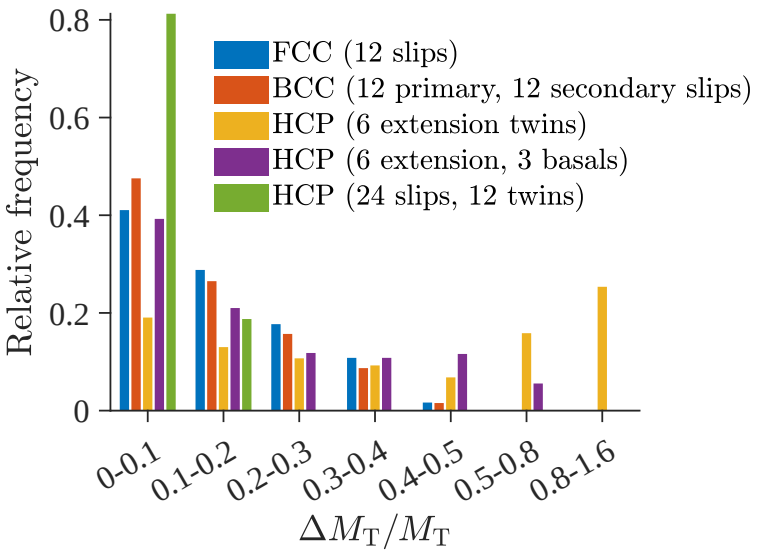

Fig. 5.9: Relative frequency of Taylor factor difference for 2,000 randomly oriented GBs. FCC: 12 slip systems $\langle 1\bar{1}0\rangle$ $\{111\}$. BCC: 12 primary slip systems $\langle \bar{1}11\rangle$ $\{110\}$ and 12 secondary slip systems $\langle \bar{1}11\rangle$ $\{211\}$; HCP: Extension twin systems (for Magnesium) (6): $\langle 10\bar{1}\bar{1}\rangle$ $\{10\bar{1}2\}$; Basal slip systems (3): $\langle 11\bar{2}0\rangle\{0001\}$; Prismatic slip system (3): $\langle 11\bar{2}0\rangle\{10\bar{1}0\}$; pyramidal slip system (6): $\langle 11\bar{2}0\rangle\{10\bar{1}1\}$ pyramidal <c+a> slip system (12): $\langle 11\bar{2}3\rangle\{10\bar{1}1\}$ Compression twin systems (for Magnesium) (6): $\langle 10\bar{1}\bar{2}\rangle\{10\bar{1}1\}$

6. CONCLUSIONS AND FUTURE DIRECTIONS

6.1 Concluding remarks

The focus of this dissertation has been model development and application of a computational framework for mesoscale modeling of dynamic failure of shocked single crystals and polycrystals. To the best of the author's knowledge, the resulting homogenized model is the first of its kind, and is particularly powerful in predicting the dynamic evolution of damage in ductile single crystal and polycrystal metals subject to high-rate loading.

In chapter 2, we have developed a dislocation-based viscoplasticity and dynamic ductile damage framework for single crystals. Within the framework the rate of crystallographic slip is determined through Orowan's expression in terms of an evolving dislocation density field and the effective mean velocity for the mobile population of dislocations. An expression for the velocity of dislocations accounts for the mechanism of phonon drag acting on dislocations, which naturally increases as dislocations approach the shear wave speed of the lattice in order to capture so-called relativistic effects. An averaging scheme was developed to approximate the evolution of the dislocation substructure in both the macroscale as well as its spatial distribution at the microscale. Beside the averaging scheme, we also incorporated the yield function for porous single crystal (Han et al., 2013) into the CRSS at macroscale to improve the accuracy of the porosity effect on macroscopic shear response on shear dominant loading regime. The kinetics of dynamic damage evolution are represented by closed-form approximations derived through a spherical shell analysis of solid matrix material surrounding an encapsulated void. By

The present chapter is based on publications by Nguyen et al. (2017, 2019).

separating the effect of macroscopic deviatoric and hydrostatic stress, crystal plasticity and dynamic void growth are solved using different yield conditions, in a consistent manner. Namely, crystal plasticity and dynamic void growth are coupled via the evolving dislocation structure and evolving porosity. Within the model for dynamic void growth, a closed-form approximation for the internal resistance to void growth was developed to represent dislocation forest interactions and high-rate dislocation dynamics.

The resulting homogenized single crystal ductile damage framework has been implemented into the commercially available finite element package Abaqus/explicit. chapter 3 provided comparison with direct numerical simulations of corresponding unit cells. We have established the relative accuracy of the approximate expressions in representing the dynamics of void growth, which are governed by both micro-inertia as well as dislocation kinetics and dislocation substructure evolution. The agreement between the homogenized theory and direct numerical simulations was shown to be quite remarkable given the sophistication of the underlying viscoplasticity framework.

In chapter 4, the crystal plasticity and damage parameters were calibrated for single crystal copper against KB/SHPB high strain-rate stress-strain measurements (Rittel et al., 2012) and acoustic spall strength measurements from plate impact test (Turley et al., 2018). Single element simulations of spallation for a range of compression pressure and strain rate indicate a favorable agreement with experimental data (Turley et al., 2018) and molecular dynamics simulation data (Luo et al., 2009a). In particular, we find that the spall strength increases with increasing compression pressure for the lower range of strain rates, but can decrease with increasing compression pressure at extreme strain rates or extreme pressures. Lastly, we provide simple scaling relations that capture the relevant physics and help elucidate the dominant governing mechanisms.

In chapter 5, we turned our attention to the spall failure of polycrystals. In particular, we explored the dominant GB characteristics and related factors that explain the pref-

erential growth and localization of damage on particular GBs within dynamically loaded polycrystalline copper (Wayne et al., 2010; Brown et al., 2015). We make use of the model presented in chapter 2, to study the effect of GB misorientation on damage localization. Our key findings on the spall failure of polycrystals are summarized as follows.

- The proposed numerical framework and subsequent analysis captures most of the trends on preferential localization of damage at GBs observed in experiments (Brown et al., 2015) for misorientation angle $\theta < 40^{\circ}$.

- By accounting for the prevalence of $\Sigma 3$ twin boundaries in polycrystalline copper within our framework, the conditional probabilities observed in experiments (Brown et al., 2015) for localization of damage with respect to misorientation angle across the entire domain of viable orientations is well captured by the model. That is, the observed correlations between grain boundaries that are preferentially more likely to exhibit damage can be solely explained by the mismatch in the mechanical response of the adjacent grains. As such, we conclude that mechanics is likely a key factor in the intergranular failure of relatively pure metals. This conclusion is in agreement with the observations of Lieberman et al. (2016) who considered the relationship between Taylor factor differences and porosity growth at GBs in full-field polycrystal calculations.

- Our analysis demonstrates that misorientation alone is not a sufficient GB characteristic to predict the likelihood of preferential localization of damage. Instead, there is a stronger correlation between the tilt angle of a GB and the conditions leading to damage localization.

- Further investigation of the dependence of preferential damage localization on mismatch in anisotropic elastic and plastic properties demonstrates that both a high

stiffness mismatch and high Taylor factor mismatch across a GB promote intergranular damage localization. The fact that $\eta_{\mathbf{X}}$ and $\frac{\Delta M_{\mathrm{T}}}{M_{\mathrm{T}}}$ are independent of twist angle and that ε_{f} does not depend on twist provides further corroboration and reasoning that GB damage localization is likely independent of twist angle.

- The statistical analysis of our simulation results suggests that mismatch in elastic and plastic properties can equally explain the observed variations in GB resistance to damage for copper. Further analysis and modeling of the hydrostatic stress concentration factor, SCF, suggests that the distinction between GBs within FCC and BCC materials with higher Zener ratio than copper will likely be driven predominantly be elastic mismatch. On the other hand, FCC and BCC materials with lower Zener ratio will be more driven by the mismatch in plastic anisotropy. HCP materials can behave similar to FCC or BCC if there are sufficient slip systems, but with limited deformation modes, HCP metals will be predominantly affected by the plasticity incompatibility.

Our work on polycrystals is meaningful not only to understand the underlying mechanisms governing the preference toward intergranular damage localization, but also provide a fundamental basis for GB engineering of dynamic strength.

6.2 Future directions

Model limitation and possible model improvement

The limitations of the model are listed as follow.

- The homogenized model was constructed based on the assumption of uniform void size and void spacing. This assumption makes it possible to simplify the representative volume element into a micromechanic equivalent volume element of a voided

sphere, which is used to build the damage evolution equation. In reality, void size and void spacing are randomly distributed inside the material (see Brown, 2015, for examples). A model development to include a statistical distribution of void families could be indirectly added by considering a statistical distribution of nucleation stresses (Wright and Ramesh, 2008).

- Void interaction and coalescence can strongly influence the material macroscopic behavior at later stage of void growth. In this model, void coalescence criteria is simply a constant porosity value (φ_{cr}). For single crystals, it has been shown that void coalescence is affected by stress triaxiality and Lode parameter (Srivastava and Needleman, 2013). A model development to incorporate those stress parameters into the critical porosity φ_{cr} could be useful to address their effect on void coalescence.

- Dislocation transportation and dislocation interaction with GB interfaces are relevant mechanisms in deforming polycrystals. They were postulated to affect the dynamic intergranular failure of polycrystals (Cerreta et al., 2012). However, the dislocation-based crystal plasticity model, upon which our homogenized model is built, ignored these mechanisms. A coupling between the crystal plasticity and a continuum dislocation transport such as the work of Luscher et al. (2016) is desired to improve the accuracy of the evolving dislocation density, and therefore the spall strength in shock loading.

- The crystal plasticity parameters were calibrated from KB/SHPB experiments. A more rigorous calibration can be performed using the early stage of velocity history in plate impact tests and simulation counterparts (see Lloyd et al., 2014b, for an example).

Despite the above limitations, the CPD-FE model proposed here might be utilized to

understand other aspects of spall strength and fracture morphology. The two aspects are briefly outlines below:

Anomalous orientation dependence of spall strength

As mentioned briefly in chapter 1, the orientation dependence of spall strength is not fully understood, with contradicting experimental data from Minich et al. (2004); Turley et al. (2018); Perez-Bergquist et al. (2011) and MD simulations result (Luo et al., 2009a). Spall strength measured from plate impact tests of Minich et al. (2004) has been used to show the dependence of spall strength on crystal orientation (see Fig. 6.1). In particular, the pullback velocity of $\langle 100 \rangle$ orientation is higher than that of $\langle 110 \rangle$ orientation on a range from 5 GPa to 50 GPa compression pressure. Figure 6.2(a) shows one example of that relationship at 9.63 GPa shock compression. A reversed correlation can be inferred from the velocity histories of Perez-Bergquist et al. (2011), in which pullback velocity of $\langle 110 \rangle$ orientation is higher than that of $\langle 100 \rangle$ orientation (see Fig. 6.2(b)). It is worth noting that the orientation of higher pullback velocity also had higher experimental-inferred tensile loading rates (by comparing the unloading slopes of the velocity histories in Fig. 6.2). It is known that the static yield strength of $\langle 110 \rangle$ orientation is larger than that of $\langle 100 \rangle$ orientation (see (Rawat et al., 2014) for an example). The reason for this is, $\langle 110 \rangle$ orientation has higher Taylor factor than $\langle 100 \rangle$ orientation ($M_T^{\langle 100 \rangle} = 2.45$ and $M_T^{\langle 110 \rangle} = 3.67$). That said, orientation dependence reported by Minich et al. (2004) and Turley et al. (2018) does not scale with the Taylor factor for those orientations. On the other hand, Luo et al. (2009a) reported no orientation dependence of spall strength on single crystal copper at extreme loading rates ($\sim 10^{10}\ \mathrm{s}^{-1}$) from MD simulations. The CPD-FE model proposed here could be used to elucidate the fundamental reasons for this anomalous orientation dependence through modeling plate impact tests of single crystals.

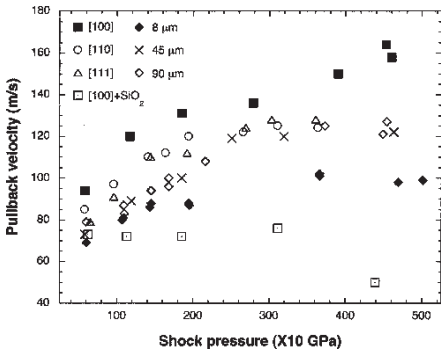

Fig. 6.1: Pullback velocity for copper single crystals of $\langle 100 \rangle$, $\langle 110 \rangle$, $\langle 111 \rangle$ orientations, and polycrystals of grain sizes 8 μm, 45 μm, 90 μm (reproduced from (Minich et al., 2004)).

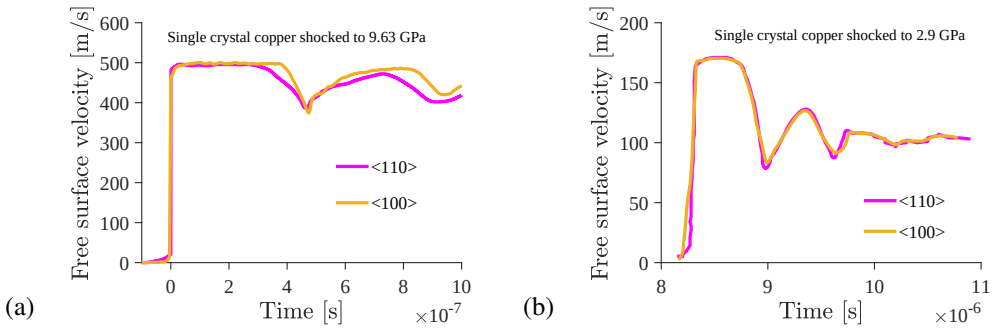

Fig. 6.2: Free surface velocity history from a) one target plate made of 2 grains with $\langle 100 \rangle$ and $\langle 110 \rangle$ orientations (reproduced from (Perez-Bergquist et al., 2011)), b) 2 plate impact tests on single crystals of $\langle 100 \rangle$ and $\langle 110 \rangle$ orientations (reproduced from (Turley et al., 2018)).

Grain size dependence of void size and void area fraction

Non-monotonic grain size dependence on final void sizes and void area fractions The void size and void area fraction was reported to be a function of grain size in (Escobedo et al., 2011). In particular, void area fraction and void size were both observed to increase with grain size, for grain size of 60 μm and up (see Fig. 6.3(a) and Fig. 6.3(b), respec-

tively). The trends reverse as grain size reduces from 60 μm to 30 μm. The reason for these trends is not fully understood. The CPD-FE model proposed here could be used to understand these correlations through modeling plate impact tests of polycrystalline target plates with explicit resolution of individual grains.

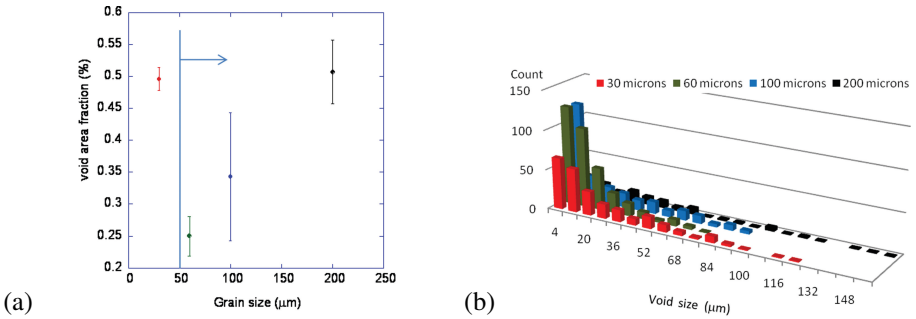

Fig. 6.3: a) Void area fraction as a function of grain size, b) void size distribution (reproduced from (Escobedo et al., 2011)).

REFERENCES

T. Antoun. *Spall fracture*. Springer Science & Business Media, 2003.

R. J. Asaro. Micromechanics of crystals and polycrystals. *Adv. Appl. Mech.*, 23:1–115, 1983.

R. A. Austin and D. L. McDowell. A dislocation-based constitutive model for viscoplastic deformation of fcc metals at very high strain rates. *Int. J. Plast.*, 27(1):1 – 24, 2011.

R. A. Austin and D. L. McDowell. Parameterization of a rate-dependent model of shock-induced plasticity for copper, nickel, and aluminum. *Int. J. Plast.*, 32- 33:134 – 154, 2012.

J. M. Ball. Discontinuous equilibrium solutions and cavitation in nonlinear elasticity. *Phil. Trans. R. Soc. A*, 306(1496):557–611, 1982.

N. Barton, J. Bernier, R. Becker, A. Arsenlis, R. Cavallo, J. Marian, M. Rhee, H.-S. Park, B. Remington, and R. Olson. A multiscale strength model for extreme loading conditions. *Journal of applied physics*, 109(7):073501, 2011.

A. A. Benzerga and J. Besson. Plastic potentials for anisotropic porous solids. *Eur. J. Mech. A. Solids*, 20(3):397–434, 2001.

A. A. Benzerga and J.-B. Leblond. Ductile fracture by void growth to coalescence. *Advances in Applied Mechanics*, 44:169–305, 2010.

J. Besson. Continuum models of ductile fracture: a review. *Int. J. Damage Mech.*, 2009.

R. Bishop, R. Hill, and N. Mott. The theory of indentation and hardness tests. *Proc. Phys. Soc.*, 57(3):147, 1945.

A. F. Bower. *Applied mechanics of solids*. CRC press, 2009.

D. Brandon. The structure of high-angle grain boundaries. *Acta metallurgica*, 14(11): 1479–1484, 1966.

A. Brown. *Three Dimensional Characterization of Microstructural Effects on Spall Damage in Shocked Polycrystalline Copper*. PhD dissertation, Arizona State University, 2015.

A. D. Brown, L. Wayne, Q. Pham, K. Krishnan, P. Peralta, S.-N. Luo, B. M. Patterson, S. Greenfield, D. Byler, K. J. McClellan, et al. Microstructural effects on damage nucleation in shock-loaded polycrystalline copper. *Metallurgical and Materials Transactions A*, 46(10):4539–4547, 2015.

J. Buchar, M. Elices, and R. Cortez. The influence of grain size on the spall fracture of copper. *Le Journal de Physique IV*, 1(C3):C3–623, 1991.

B. Budiansky, J. Hutchinson, and S. Slutsky. *Void growth and collapse in viscous solids*. Pergamon Press, London, 1982.

H. Bunge. Some applications of the taylor theory of polycrystal plasticity. *Crystal Research and Technology*, 5(1):145–175, 1970.

M. Carroll and A. Holt. Static and dynamic pore-collapse relations for ductile porous materials. *J. Appl. Phys.*, 43(4):1626–1636, 1972.

E. K. Cerreta, J. Escobedo, A. Perez-Bergquist, D. Koller, C. P. Trujillo, G. Gray Iii, C. Brandl, and T. Germann. Early stage dynamic damage and the role of grain boundary type. *Scripta Materialia*, 66(9):638–641, 2012.

X. Chen, J. Asay, S. Dwivedi, and D. Field. Spall behavior of aluminum with varying microstructures. *Journal of applied physics*, 99(2):023528, 2006.

C. Chu and A. Needleman. Void nucleation effects in biaxially stretched sheets. *J. Eng. Mater. Technol.*, 102(3):249–256, 1980.

J. Clayton. Dynamic plasticity and fracture in high density polycrystals: constitutive modeling and numerical simulation. *Journal of the Mechanics and Physics of Solids*, 53(2): 261–301, 2005.

R. Cortés. Dynamic growth of microvoids under combined hydrostatic and deviatoric

stresses. *Int. J. Solids Struct.*, 29(13):1637–1645, 1992a.

R. Cortés. The growth of microvoids under intense dynamic loading. *Int. J. Solids Struct.*, 29(11):1339–1350, 1992b.

J. Cuq-Lelandais, M. Boustie, L. Berthe, T. De Rességuier, P. Combis, J.-P. Colombier, M. Nivard, and A. Claverie. Spallation generated by femtosecond laser driven shocks in thin metallic targets. *J. Phys. D: Appl. Phys.*, 42(6):065402, 2009.

D. Curran, L. Seaman, and D. Shockey. Dynamic failure of solids. *Physics reports*, 147 (5-6):253–388, 1987.

C. Czarnota, S. Mercier, and A. Molinari. Modelling of nucleation and void growth in dynamic pressure loading, application to spall test on tantalum. *Int. J. Fract.*, 141(1-2): 177–194, 2006.

C. Czarnota, N. Jacques, S. Mercier, and A. Molinari. Modelling of dynamic ductile fracture and application to the simulation of plate impact tests on tantalum. *Journal of the Mechanics and Physics of Solids*, 56(4):1624–1650, 2008.

M. Dewald and W. Curtin. Multiscale modelling of dislocation/grain boundary interactions. ii. screw dislocations impinging on tilt boundaries in al. *Philosophical Magazine*, 87(30):4615–4641, 2007.

K. Enakoutsa and J.-B. Leblond. Numerical implementation and assessment of the glpd micromorphic model of ductile rupture. *European Journal of Mechanics-A/Solids*, 28 (3):445–460, 2009.

J. Escobedo, D. Dennis-Koller, E. Cerreta, B. Patterson, C. Bronkhorst, B. Hansen, D. Tonks, and R. Lebensohn. Effects of grain size and boundary structure on the dynamic tensile response of copper. *Journal of Applied Physics*, 110(3):033513, 2011.

J. Escobedo, E. Cerreta, and D. Dennis-Koller. Effect of crystalline structure on intergranular failure during shock loading. *Jom*, 66(1):156–164, 2014.

J. P. Escobedo, E. K. Cerreta, D. Dennis-Koller, C. P. Trujillo, and C. A. Bronkhorst.

Influence of boundary structure and near neighbor crystallographic orientation on the dynamic damage evolution during shock loading. *Philosophical Magazine*, 93(7):833–846, 2013.

J. Eshelby. Uniformly moving dislocations. *Proc. Phys. Soc. London, Sect. A*, 62(5):307, 1949.

A. Every and A. McCurdy. *Second and Higher Order Elastic Constants/ Elastische Konstanten zweiter und höherer Ordnung*. Landolt-Börnstein: Numerical Data and Functional Relationships in Science and Technology - New Series / Condensed Matter. Springer Berlin Heidelberg, 1992. ISBN 9783540544104.

S. Fensin, J. Escobedo-Diaz, C. Brandl, E. Cerreta, G. Gray Iii, T. Germann, and S. Valone. Effect of loading direction on grain boundary failure under shock loading. *Acta Materialia*, 64:113–122, 2014.

S. J. Fensin and E. N. Hahn. Predicting susceptibility of grain boundaries to failure in bcc materials. Technical report, Los Alamos National Lab.(LANL), Los Alamos, NM (United States), 2017.

J. M. Fick, K. Ramesh, and P. Swaminathan. Modeling of ductile fragmentation that includes void interactions. *J. Mech. Phys. Solids*, 85:54–73, 2015.

E. V. Fortin, A. D. Brown, L. Wayne, and P. D. Peralta. Microstructural analysis of spall damage nucleation and growth in multicrystalline titanium. In *ASME 2016 International Mechanical Engineering Congress and Exposition*, pages V009T12A044–V009T12A044. American Society of Mechanical Engineers, 2016.

W. Garrison and N. Moody. Ductile fracture. *J. Phys. Chem. Solids*, 48(11):1035–1074, 1987.

D. Grady. The spall strength of condensed matter. *Journal of the Mechanics and Physics of Solids*, 36(3):353–384, 1988.

G. Gray III, N. Bourne, and B. Henrie. On the influence of loading profile upon the tensile

failure of stainless steel. *Journal of applied physics*, 101(9):093507, 2007.

A. L. Gurson. Continuum theory of ductile rupture by void nucleation and growth: Part i-yield criteria and flow rules for porous ductile media. *J. Eng. Mater. Technol.*, 99(1): 2–15, 1977.

M. Haghi and L. Anand. Analysis of strain-hardening viscoplastic thick-walled sphere and cylinder under external pressure. *Int. J. Plast.*, 7(3):123–140, 1991.

X. Han, J. Besson, S. Forest, B. Tanguy, and S. Bugat. A yield function for single crystals containing voids. *Int. J. Solids Struct.*, 50(14):2115–2131, 2013.

D. Handscomb. On the random disorientation of two cubes. *Can. J. Math*, 10:85–88, 1958.

H. Hibbit, B. Karlsson, and E. Sorensen. Abaqus user manual, version 6.12. *Simulia, Providence, RI*, 2012.

R. Hill. *The mathematical theory of plasticity*, volume 11. Oxford university press, 1950.

Y. Huang, J. Hutchinson, and V. Tvergaard. Cavitation instabilities in elastic-plastic solids. *J. Mech. Phys. Solids*, 39(2):223–241, 1991.

Y. Huang, H. Gao, W. Nix, and J. Hutchinson. Mechanism-based strain gradient plasticity—ii. analysis. *J. Mech. Phys. Solids*, 48(1):99–128, 2000.

N. Jacques, C. Czarnota, S. Mercier, and A. Molinari. A micromechanical constitutive model for dynamic damage and fracture of ductile materials. *Int. J. Fract.*, 162(1-2): 159–175, 2010.

N. Jacques, S. Mercier, and A. Molinari. Effects of microscale inertia on dynamic ductile crack growth. *J. Mech. Phys. Solids*, 60(4):665 – 690, 2012a.

N. Jacques, S. Mercier, and A. Molinari. Multiscale modelling of voided ductile solids with micro-inertia and application to dynamic crack propagation. *Procedia IUTAM*, 3: 53–66, 2012b.

N. Jacques, S. Mercier, and A. Molinari. A constitutive model for porous solids taking into

account microscale inertia and progressive void nucleation. *Mech. Mater.*, 80:311–323, 2015.

Z.-H. Jin, P. Gumbsch, K. Albe, E. Ma, K. Lu, H. Gleiter, and H. Hahn. Interactions between non-screw lattice dislocations and coherent twin boundaries in face-centered cubic metals. *Acta Materialia*, 56(5):1126–1135, 2008.

G. R. Johnson and W. H. Cook. A constitutive model and data for metals subjected to large strains, high strain rates and high temperatures. In *Proc. 7th Int. Symp. on Ballistics*, volume 21, pages 541–547. The Hague, The Netherlands, 1983.

G. R. Johnson and W. H. Cook. Fracture characteristics of three metals subjected to various strains, strain rates, temperatures and pressures. *Engineering fracture mechanics*, 21(1): 31–48, 1985.

J. Johnson and F. Addessio. Tensile plasticity and ductile fracture. *Journal of applied physics*, 64(12):6699–6712, 1988.

J. N. Johnson. Dynamic fracture and spallation in ductile solids. *J. Appl. Phys.*, 52(4): 2812–2825, 1981.

G. Kanel. Spall fracture: methodological aspects, mechanisms and governing factors. *International journal of fracture*, 163(1-2):173–191, 2010.

S. Keralavarma and A. Benzerga. A constitutive model for plastically anisotropic solids with non-spherical voids. *J. Mech. Phys. Solids*, 58(6):874–901, 2010.

S. Keralavarma, S. Hoelscher, and A. Benzerga. Void growth and coalescence in anisotropic plastic solids. *Int. J. Solids Struct.*, 48(11):1696–1710, 2011.

S. M. Keralavarma and A. A. Benzerga. An approximate yield criterion for anisotropic porous media. *Comptes Rendus Mécanique*, 336(9):685–692, 2008.

J. Knowles and M. Jakub. Finite dynamic deformations of an incompressible elastic medium containing a spherical cavity. *Arch. Ration. Mech. Anal.*, 18(5):367–378, 1965.

U. Kocks. The relation between polycrystal deformation and single-crystal deformation.

Metall. Mater. Trans., 1(5):1121–1143, 1970.

K. Krishnan, A. Brown, L. Wayne, J. Vo, S. Opie, H. Lim, P. Peralta, S.-N. Luo, D. Byler, K. J. McClellan, et al. Three-dimensional characterization and modeling of microstructural weak links for spall damage in fcc metals. *Metallurgical and Materials Transactions A*, 46(10):4527–4538, 2015.

L. Kubin, B. Devincre, and T. Hoc. Modeling dislocation storage rates and mean free paths in face-centered cubic crystals. *Acta Mater.*, 56(20):6040 – 6049, 2008.

A. Y. Kuksin, V. Stegaĭlov, and A. Yanilkin. Atomistic simulation of plasticity and fracture of nanocrystalline copper under high-rate tension. *Physics of the Solid State*, 50(11): 2069–2075, 2008.

R. A. Lebensohn and C. Tomé. A self-consistent anisotropic approach for the simulation of plastic deformation and texture development of polycrystals: application to zirconium alloys. *Acta metallurgica et materialia*, 41(9):2611–2624, 1993.

R. A. Lebensohn, J. P. Escobedo, E. K. Cerreta, D. Dennis-Koller, C. A. Bronkhorst, and J. F. Bingert. Modeling void growth in polycrystalline materials. *Acta Materialia*, 61 (18):6918–6932, 2013.

P. Lejček. *Grain boundary segregation in metals*, volume 136. Springer Science & Business Media, 2010.

E. J. Lieberman, R. A. Lebensohn, D. B. Menasche, C. A. Bronkhorst, and A. D. Rollett. Microstructural effects on damage evolution in shocked copper polycrystals. *Acta Materialia*, 116:270–280, 2016.

S. Lin and T. Mura. Elastic fields of inclusions in anisotropic media (ii). *Physica Status Solidi (a)*, 15(1):281–285, 1973.

C. Ling, J. Besson, S. Forest, B. Tanguy, F. Latourte, and E. Bosso. An elastoviscoplastic model for porous single crystals at finite strains and its assessment based on unit cell simulations. *International Journal of Plasticity*, 84:58–87, 2016.

C. Ling, B. Tanguy, J. Besson, S. Forest, and F. Latourte. Void growth and coalescence in triaxial stress fields in irradiated fcc single crystals. *Journal of Nuclear Materials*, 492: 157–170, 2017.

C. Ling, S. Forest, J. Besson, B. Tanguy, and F. Latourte. A reduced micromorphic single crystal plasticity model at finite deformations. application to strain localization and void growth in ductile metals. *International Journal of Solids and Structures*, 134:43–69, 2018.

J. Lloyd, J. Clayton, R. Austin, and D. McDowell. Plane wave simulation of elastic-viscoplastic single crystals. *J. Mech. Phys. Solids*, 69:14–32, 2014a.

J. Lloyd, J. Clayton, R. Becker, and D. McDowell. Simulation of shock wave propagation in single crystal and polycrystalline aluminum. *Int. J. Plast.*, 60:118–144, 2014b.

S. L. Lohr. *Sampling: Design and Analysis*. Cengage Learning, 2009.

S.-N. Luo, Q. An, T. C. Germann, and L.-B. Han. Shock-induced spall in solid and liquid cu at extreme strain rates. *Journal of Applied Physics*, 106(1):013502, 2009a.

S.-N. Luo, T. C. Germann, and D. L. Tonks. Spall damage of copper under supported and decaying shock loading. *Journal of Applied Physics*, 106(12):123518, 2009b.

D. Luscher, J. Mayeur, H. Mourad, A. Hunter, and M. Kenamond. Coupling continuum dislocation transport with crystal plasticity for application to shock loading conditions. *Int. J. Plast.*, 76:111–129, 2016.

D. Luscher, F. Addessio, M. Cawkwell, and K. Ramos. A dislocation density-based continuum model of the anisotropic shock response of single crystal α-cyclotrimethylene trinitramine. *J. Mech. Phys. Solids*, 98:63–86, 2017.

D. J. Luscher, C. A. Bronkhorst, C. N. Alleman, and F. L. Addessio. A model for finite-deformation nonlinear thermomechanical response of single crystal copper under shock conditions. *J. Mech. Phys. Solids*, 61(9):1877 – 1894, 2013.

D. J. Luscher, M. A. Buechler, D. J. Walters, C. A. Bolme, and K. J. Ramos. On computing

the evolution of temperature for materials under dynamic loading. *International Journal of Plasticity*, 111:188–210, 2018.

A. Ma and F. Roters. A constitutive model for fcc single crystals based on dislocation densities and its application to uniaxial compression of aluminium single crystals. *Acta Mater.*, 52(12):3603–3612, 2004.

K. Mackenchery, R. R. Valisetty, R. R. Namburu, A. Stukowski, A. M. Rajendran, and A. M. Dongare. Dislocation evolution and peak spall strengths in single crystal and nanocrystalline cu. *Journal of Applied Physics*, 119(4):044301, 2016.

J. Mackenzie. Second paper on statistics associated with the random disorientation of cubes. *Biometrika*, 45(1-2):229–240, 1958.

A. Mbiakop, A. Constantinescu, and K. Danas. An analytical model for porous single crystals with ellipsoidal voids. *J. Mech. Phys. Solids*, 84:436–467, 2015.

F. A. McClintock. A criterion for ductile fracture by the growth of holes. *J. Appl. Mech.*, 35(2):363–371, 1968.

R. McQueen and S. Marsh. Equation of state for nineteen metallic elements from shock-wave measurements to two megabars. *Journal of Applied Physics*, 31(7):1253–1269, 1960.

M. A. Meyers. *Dynamic behavior of materials*. John wiley & sons, 1994.

M. A. Meyers and C. T. Aimone. Dynamic fracture (spalling) of metals. *Progress in Materials Science*, 28(1):1–96, 1983.

R. W. Minich, J. U. Cazamias, M. Kumar, and A. J. Schwartz. Effect of microstructural length scales on spall behavior of copper. *Metall. Mater. Trans. A*, 35(9):2663–2673, 2004.

A. Molinari and S. Mercier. Micromechanical modelling of porous materials under dynamic loading. *J. Mech. Phys. Solids*, 49(7):1497–1516, 2001.

A. Molinari and T. Wright. A physical model for nucleation and early growth of voids

in ductile materials under dynamic loading. *J. Mech. Phys. Solids*, 53(7):1476–1504, 2005.

A. Molinari, N. Jacques, S. Mercier, J.-B. Leblond, and A. A. Benzerga. A micromechanical model for the dynamic behavior of porous media in the void coalescence stage. *Int. J. Solids Struct.*, 71:1–18, 2015.

V. Monchiet, O. Cazacu, E. Charkaluk, and D. Kondo. Macroscopic yield criteria for plastic anisotropic materials containing spheroidal voids. *Int. J. Plast.*, 24(7):1158–1189, 2008.

J. A. Moore, S. F. Li, M. Rhee, and N. R. Barton. Modeling the effects of grain and porosity structure on copper spall response. *Journal of Dynamic Behavior of Materials*, pages 1–17, 2018.

T. Mori and K. Tanaka. Average stress in matrix and average elastic energy of materials with misfitting inclusions. *Acta Metall.*, 21(5):571–574, 1973.

E. Moshe, S. Eliezer, E. Dekel, A. Ludmirsky, Z. Henis, M. Werdiger, I. Goldberg, N. Eliaz, and D. Eliezer. An increase of the spall strength in aluminum, copper, and metglas at strain rates larger than 107 s- 1. *J. Appl. Phys.*, 83(8):4004–4011, 1998.

E. Moshe, S. Eliezer, Z. Henis, M. Werdiger, E. Dekel, Y. Horovitz, S. Maman, I. Goldberg, and D. Eliezer. Experimental measurements of the strength of metals approaching the theoretical limit predicted by the equation of state. *Appl. Phys. Lett.*, 76(12):1555–1557, 2000.

T. Mura. *Micromechanics of defects in solids*. Monographs and Textbooks on Mechanics of Solids and Fluids. Springer Netherlands, 2013. ISBN 9789401193061.

S. Nemat-Nasser and M. Hori. Void collapse and void growth in crystalline solids. *J. Appl. Phys.*, 62(7):2746–2757, 1987.

G. D. Nguyen, A. M. Korsunsky, and J. P.-H. Belnoue. A nonlocal coupled damage-plasticity model for the analysis of ductile failure. *Int. J. Plast.*, 64:56–75, 2015.

T. Nguyen, D. Luscher, and J. Wilkerson. A dislocation-based crystal plasticity framework for dynamic ductile failure of single crystals. *Journal of the Mechanics and Physics of Solids*, 108:1–29, 2017.

T. Nguyen, D. J. Luscher, and J. W. Wilkerson. The role of elastic and plastic anisotropy in intergranular spall failure. *Acta Materialia*, 2019. ISSN 1359-6454.

M. Ortiz and A. Molinari. Effect of strain hardening and rate sensitivity on the dynamic growth of a void in a plastic material. *J. Appl. Mech.*, 59(1):48–53, 1992.

D. Paquet and S. Ghosh. Microstructural effects on ductile fracture in heterogeneous materials. part ii: Applications to cast aluminum microstructures. *Eng. Fract. Mech.*, 78 (2):226–233, 2011.

J. Paux, L. Morin, R. Brenner, and D. Kondo. An approximate yield criterion for porous single crystals. *Eur. J. Mech. A-Solids*, 51:1–10, 2015.

J. Paux, R. Brenner, and D. Kondo. Plastic yield criterion and hardening of porous single crystals. *International Journal of Solids and Structures*, 132:80–95, 2018.

N. A. Pedrazas, D. L. Worthington, D. A. Dalton, P. A. Sherek, S. P. Steuck, H. J. Quevedo, A. C. Bernstein, E. M. Taleff, and T. Ditmire. Effects of microstructure and composition on spall fracture in aluminum. *Materials Science and Engineering: A*, 536:117–123, 2012.

P. Peralta, S. DiGiacomo, S. Hashemian, S.-N. Luo, D. Paisley, R. Dickerson, E. Loomis, D. Byler, K. McClellan, and H. D'Armas. Characterization of incipient spall damage in shocked copper multicrystals. *Int. J. Damage Mech.*, 18(4):393–413, 2009.

A. Perez-Bergquist, E. K. Cerreta, C. P. Trujillo, F. Cao, and G. Gray III. Orientation dependence of void formation and substructure deformation in a spalled copper bicrystal. *Scripta Materialia*, 65(12):1069–1072, 2011.

P. Perzyna. Internal state variable description of dynamic fracture of ductile solids. *Int. J. Solids Struct.*, 22(7):797–818, 1986.

A. Pineau and T. Pardoen. Failure mechanisms of metals. *Comprehensive structural integrity encyclopedia*, 2, 2007.

A. Pineau, A. A. Benzerga, and T. Pardoen. Failure of metals i: Brittle and ductile fracture. *Acta Mater.*, 107:424–483, 2016.

C. P. Przybyla, B. L. Adams, and M. P. Miles. Methodology for determining the variance of the taylor factor: application in fe-3% si. *Journal of Engineering Materials and Technology*, 129(1):82–93, 2007.

J. Qu and M. Cherkaoui. *Fundamentals of Micromechanics of Solids*. Wiley, 2006. ISBN 9780471464518.

S. I. Ranganathan and M. Ostoja-Starzewski. Universal elastic anisotropy index. *Physical Review Letters*, 101(5):055504, 2008.

S. Rawat, S. Chandra, V. Chavan, S. Sharma, M. Warrier, S. Chaturvedi, and R. Patel. Integrated experimental and computational studies of deformation of single crystal copper at high strain rates. *Journal of Applied Physics*, 116(21):213507, 2014.

S. Razorenov, G. Kanel, B. Herrmann, E. Zaretsky, and G. Ivanchihina. Influence of nano-size inclusions on spall fracture of copper single crystals. In *AIP Conference Proceedings*, volume 955, pages 581–584. AIP, 2007.

F. Reusch, B. Svendsen, and D. Klingbeil. Local and non-local gurson-based ductile damage and failure modelling at large deformation. *Eur. J. Mech. A-Solid*, 22(6):779–792, 2003.

J. R. Rice and D. M. Tracey. On the ductile enlargement of voids in triaxial stress fields. *J. Mech. Phys. Solids*, 17(3):201–217, 1969.

D. Rittel, A. Kidane, M. Alkhader, A. Venkert, P. Landau, and G. Ravichandran. On the dynamically stored energy of cold work in pure single crystal and polycrystalline copper. *Acta Materialia*, 60(9):3719–3728, 2012.

V. Romanchenko and G. Stepanov. Dependence of the critical stresses on the loading time

parameters during spall in copper, aluminum, and steel. *Journal of Applied Mechanics and Technical Physics*, 21(4):555–561, 1980.

J. Schiøtz and K. W. Jacobsen. A maximum in the strength of nanocrystalline copper. *Science*, 301(5638):1357–1359, 2003.

S. Schmauder and M. Meyer. Correlation between Dundurs' parameters and elastic constants. *Z. Metallkd*, 83(7):524–527, 1992.

L. Seaman, D. R. Curran, and D. A. Shockey. Computational models for ductile and brittle fracture. *J. Appl. Phys.*, 47(11):4814–4826, 1976.

S. Srinivasan, M. Baskes, and G. Wagner. Atomistic simulations of shock induced microstructural evolution and spallation in single crystal nickel. *Journal of applied physics*, 101(4):043504, 2007.

A. Srivastava and A. Needleman. Void growth versus void collapse in a creeping single crystal. *Journal of the Mechanics and Physics of Solids*, 61(5):1169–1184, 2013.

R. Stoller and S. Zinkle. On the relationship between uniaxial yield strength and resolved shear stress in polycrystalline materials. *J. Nucl. Mater.*, 283 - 287, Part 1:349 – 352, 2000.

A. Sutton and R. Balluffi. *Interfaces in crystalline materials*. Monographs on the physics and chemistry of materials. Clarendon Press, 1995. ISBN 9780198513858.

G. I. Taylor. Plastic strain in metals. *J. Inst. Metals*, 62:307–324, 1938.

W. Tong and G. Ravichandran. Dynamic pore collapse in viscoplastic materials. *J. Appl. Phys.*, 74(4):2425–2435, 1993.

W. Tong and G. Ravichandran. Inertial effects on void growth in porous viscoplastic materials. *J. Appl. Mech.*, 62(3):633–639, 1995.

W. Turley, S. Fensin, R. Hixson, D. Jones, B. La Lone, G. Stevens, S. Thomas, and L. Veeser. Spall response of single-crystal copper. *Journal of Applied Physics*, 123 (5):055102, 2018.

V. Tvergaard. Influence of voids on shear band instabilities under plane strain conditions. *Int. J. Fract.*, 17(4):389–407, 1981.

V. Tvergaard and A. Needleman. Analysis of the cup-cone fracture in a round tensile bar. *Acta Metall.*, 32(1):157–169, 1984.

V. Tvergaard and A. Needleman. Effects of nonlocal damage in porous plastic solids. *Int. J. Solids Struct.*, 32(8):1063–1077, 1995.

T. Vogler and J. D. Clayton. Heterogeneous deformation and spall of an extruded tungsten alloy: plate impact experiments and crystal plasticity modeling. *Journal of the Mechanics and Physics of Solids*, 56(2):297–335, 2008.

Y. Wang, M. Qi, H. He, and L. Wang. Spall failure of aluminum materials with different microstructures. *Mechanics of Materials*, 69(1):270–279, 2014.

Z.-P. Wang. Growth of voids in porous ductile materials at high strain rate. *J. Appl. Phys.*, 76(3):1535–1542, 1994.

Z.-P. Wang. Void-containing nonlinear materials subject to high-rate loading. *J. Appl. Phys.*, 81(11):7213–7227, 1997.

Z.-P. Wang and Q. Jiang. A yield criterion for porous ductile media at high strain rate. *J. Appl. Mech.*, 64(3):503–509, 1997.

L. Wayne, K. Krishnan, S. DiGiacomo, N. Kovvali, P. Peralta, S. Luo, S. Greenfield, D. Byler, D. Paisley, K. McClellan, A. Koskelo, and R. Dickerson. Statistics of weak grain boundaries for spall damage in polycrystalline copper. *Scr. Mater.*, 63(11):1065 – 1068, 2010.

J. Wen, Y. Huang, K. Hwang, C. Liu, and M. Li. The modified gurson model accounting for the void size effect. *Int. J. Plast.*, 21(2):381–395, 2005a.

J. Wen, K.-C. Hwang, and Y. Huang. Extension of the gurson model accounting for the void size effect. *Acta Mech. Sin.*, 21(2):142–150, 2005b.

J. Wilkerson. On the micromechanics of void dynamics at extreme rates. *Int. J. Plast.*,

2017.

J. Wilkerson and K. Ramesh. A dynamic void growth model governed by dislocation kinetics. *J. Mech. Phys. Solids*, 70:262 – 280, 2014.

J. Wilkerson and K. Ramesh. Unraveling the anomalous grain size dependence of cavitation. *Physical review letters*, 117(21):215503, 2016.

D. Wolf and S. Phillpot. Role of the densest lattice planes in the stability of crystalline interfaces: A computer simulation study. *Materials Science and Engineering: A*, 107: 3–14, 1989.

D. Wolf and S. Yip. *Materials interfaces: atomic-level structure and properties*. Springer Science & Business Media, 1992.

T. Wright and K. Ramesh. Dynamic void nucleation and growth in solids: A self-consistent statistical theory. *J. Mech. Phys. Solids*, 56(2):336 – 359, 2008.

Q. Wu and M. Zikry. Microstructural modeling of transgranular and intergranular fracture in crystalline materials with coincident site lattice grain-boundaries: σ3 and σ17b bicrystals. *Materials Science and Engineering: A*, 661:32–39, 2016.

X. Wu, K. Ramesh, and T. Wright. The coupled effects of plastic strain gradient and thermal softening on the dynamic growth of voids. *Int. J. Solids Struct.*, 40(24):6633–6651, 2003a.

X. Wu, K. Ramesh, and T. Wright. The dynamic growth of a single void in a viscoplastic material under transient hydrostatic loading. *J. Mech. Phys. Solids*, 51(1):1–26, 2003b.

X. Wu, K. Ramesh, and T. Wright. The effects of thermal softening and heat conduction on the dynamic growth of voids. *Int. J. Solids Struct.*, 40(17):4461–4478, 2003c.

Y. Yang, P. Zhi-qiang, C. Xing-zhi, G. Zhao-liang, T. Tie-gang, H. Hai-bo, and Z. Qing-ming. Spall behaviors of high purity copper under sweeping detonation. *Materials Science and Engineering: A*, 651:636–645, 2016.

J. Zhang and S. P. Joshi. Phenomenological crystal plasticity modeling and detailed mi-

cromechanical investigations of pure magnesium. *Journal of the Mechanics and Physics of Solids*, 60(5):945–972, 2012.

J. Zheng, Y. Bai, and Z. Wang. Influence of inertial and thermal effects on the dynamic growth of voids in porous ductile materials. *Le Journal de Physique IV*, 4(C8):C8–765, 1994.

A. Zurek, J. Johnson, and C. E. Frantz. Characterization of dynamic fracture in copper under uniaxial stress and uniaxial strain. *Le Journal de Physique Colloques*, 49(C3): C3–269, 1988.

APPENDIX

Implementation

The CP model (without damage) was implemented into user-defined subroutine VUMAT (Abaqus/Explicit subroutines to define material behavior) by Dr. Darby J. Luscher. The detail implementation was described in (Luscher et al., 2017). The backbone of the CP model implementation is the 4th order Runge-Kutta scheme to integrate the rate equations of crystal plasticity constitutive laws (subsection 2.2.1).

The VUMAT subroutine for CPD was build upon the VUMAT subroutine for CP by adding a step prior to the 4th order Runge-Kutta CP integration scheme. In the step, a backward Euler integration scheme was used to integrate porosity (φ) in the second order ODE (i.e. Eq. (2.2.22)) based on the trial stress. The porosity and equivalent plasticity due to void growth (Eq. (2.1.12)) are then passed into the evolving dislocation density on both microscale and macroscale in the subsequent 4th order Runge-Kutta scheme.

The uncoupled integration scheme is not ideal for solving the set of nonlinear and complex (CPD) constitutive equations. In order to limit the accumulated error from this uncoupled integration scheme, a sub-incrementation scheme is used over time steps of large change in solution dependent variables (such as dislocation density and porosity). In particular, time increment is cut into half whenever the estimated error from the Runge-Kutta method (obtained by comparing the 3rd order and 4th order Runge-Kutta) or from Backward Euler method is larger than the targeted tolerance.

Verification

The subsections provides verification of some key equations in the CPD model.

CP implementation: Cliffton' equation for dislocation velocity

In order to verify the implementation of Cliffton' equation for dislocation velocity (Eq. (2.2.4)), uniaxial strain loading in $\langle 100 \rangle$ direction in a single hexagonal volume element was conducted. Due to the loading direction, 8 slip systems can be equally activated (Lloyd et al., 2014a) in this BVP. The CRSS ($\tau_{cr}^{(\alpha)}$) is removed to further simplify the problem (by setting $\tau_0 = 0$ and $c_\perp = 0$). The evolution of dislocation velocity ($v_\perp$) with respect to RSS (τ) from the simulation result for one activated slip system are plotted in Fig. 6.4 and in a excellent agreement with the analytical solution of Eq. (2.2.4).

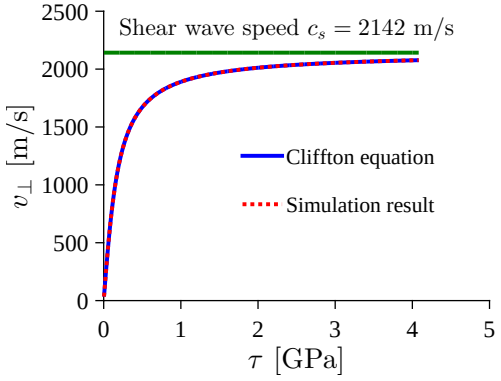

Fig. 6.4: Comparison of dislocation velocity evolution with respect to RSS from one element simulation and Cliffton's equation analytical solution

Porosity evolution implementation

This subsection provides verification for the backward Euler integration scheme to solve porosity in Eq. (2.2.22). For simplicity, we set internal resistance to be zero, i.e. $\mathcal{R} = 0$ (by setting $\tau_0 = 0$, $c_\perp = 0$, $M_T = 0$), the second order ODE for porosity becomes

$$\frac{1}{3}\rho_s \ell_v^2 \left(\frac{1 - \sqrt[3]{\varphi}}{\sqrt[3]{\varphi}(1-\varphi)} \ddot{\varphi} - \frac{1 - 12\varphi + 11\varphi^{4/3}}{6\varphi^{4/3}(1-\varphi)^2} \dot{\varphi}^2 \right) = \Sigma_m \tag{6.2.1}$$

In the following two subsubsections, a stress controlled loading is applied to the volume element rather than the displacement control as the previous subsection.

Special case 1: Constant loading rate

For the special case of constant external stress rate, i.e. $\frac{d\Sigma_m}{dt} = \text{const}$, the void growth rate $\dot{a}$ approaches asymptotic void velocity $\dot{a}^*$ as a/a_0 approach infinity (see (Wilkerson, 2017), equation 3.3),

$$\dot{a}^* = \sqrt{\frac{6}{11}\frac{\Sigma_m}{\rho_s}} \tag{6.2.2}$$

Figure 6.5 shows the comparison of void velocity from the asymptotic formulation (Eq. (6.2.2)) and from numerical simulation. For this simulation, the external stress rate is set to be $\frac{d\Sigma_m}{dt} = 10\frac{\text{MPa}}{\mu\text{s}}$; the time integration increment is $\Delta t = 10^{-3}$ μs; void spacing is ℓ_v = 1000μm; initial void size is a_0 = 1 μm (or $\varphi_0 = 10^{-9}$). As can be seen in Fig. 6.5, the void velocity from numerical simulation successfully approaches the analytical velocity as a/a_0 approaches infinity, as expected in this special loading scenario.

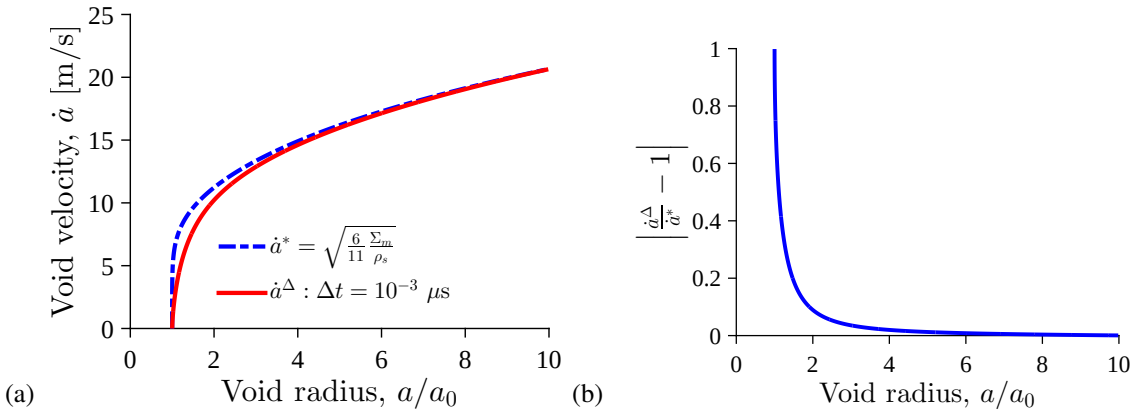

Fig. 6.5: (a) Void velocity evolution with respect to void radius, (b) Relative difference between void velocity and its asymptote with respect to void radius.

Special case 2: Solve for a given analytical expression φ^*

This subsection provides verification on solution convergence due to reducing time step size. Here, a given analytical evolution of porosity with respect to time is assumed,

$$\varphi^* = 0.001 + 10t^3. \tag{6.2.3}$$

Void spacing is set to be $\ell_v = 10$ μm. Putting the analytical function φ^* into Eq. (6.2.1), a analytical expression for mean stress can be express as below

$$\Sigma_m = \frac{1}{3}\rho_s \ell_v^2 \left\{ \begin{array}{c} 60t \frac{1-\left(10^{-3}+10t^3\right)^{1/3}}{\left(10^{-3}+10t^3\right)^{1/3}\left[1-\left(10^{-3}+10t^3\right)\right]} \\ -900t^4 \frac{\frac{11}{6}\left(10^{-3}+10t^3\right)^{4/3}-20t^3+\frac{247}{1500}}{\left(10^{-3}+10t^3\right)^{4/3}\left[1-\left(10^{-3}+10t^3\right)\right]^2} \end{array} \right\} \tag{6.2.4}$$

Using Eq. (6.2.4) as the external applied stress with respect to loading time, the porosity evolution from the backward Euler scheme can be obtained. The numerical solution for porosity (φ^{Δ}) is then plotted in comparison with the given analytical expression (φ^*) in Fig. 6.6. The results show that numerical solution for porosity (φ^{Δ}) converges to the given analytical expression (φ^*) with decreasing time step size.

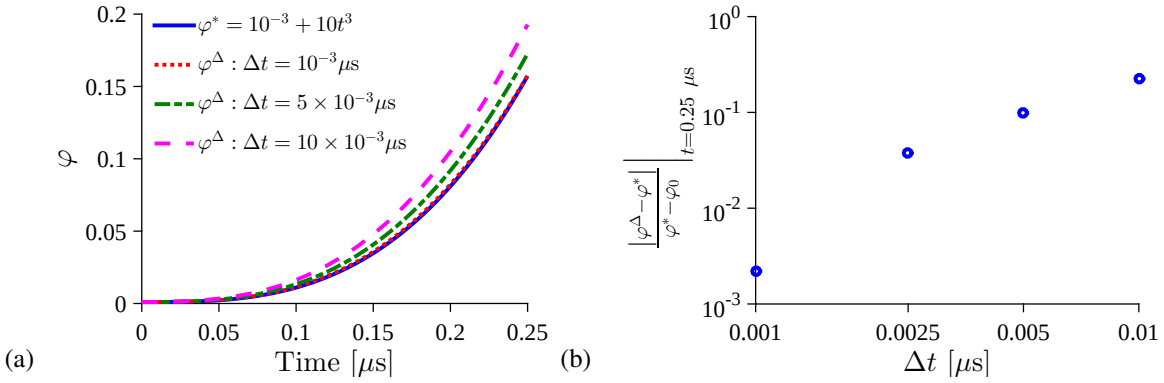

Fig. 6.6: (a) Comparison of the analytical solution, φ^*, and the numerical solution, φ^Δ for different time increment, (b) relative error of numerical solution at $t = 0.25$ μs with respect to time step.